UNIVERSITÀ DELLA CALABRIA

UNIVERSITA' DELLA CALABRIA

Dipartimento di Ingegneria Informatica. Modellistica, Elettronica e Sistemistica (DIMES)

Dottorato di Ricerca in

Ingegneria dei Sistemi ed Informatica

CICLO

XXVIII

Modellizzazione micromagnetica di dispositivi spintronici: dallo stato uniforme allo skyrmion

Settore Scientifico Disciplinare ING-IND/31

Coordinatore: Ch.mo Prof. Felice Crupi

Firma

Supervisore: Ch.mo Prof. Mario Carpentieri

Firma

Dottorando: Dott. Riccardo Tomasello

Firma

UNIVERSITÀ DELLA CALABRIA

UNIVERSITY OF CALABRIA

Department of Computer Science, Modeling, Electronics, and System Science (DIMES)

Degree of Doctor of Philosophy in

System and Computer Engineering

CYCLE

XXVIII

Micromagnetic modeling of spintronic devices: from uniform state to skyrmion

Scientific Sector ING-IND/31

Coordinator: Ch.mo Prof. Felice Crupi

Firma _____

Supervisor: Ch.mo Prof. Mario Carpentieri

Firma _____

Ph. D. student: Dott. Riccardo Tomasello

Firma _____

RIASSUNTO

La Spintronica è una branca della Fisica che ha attratto un notevole interesse negli ultimi 30 anni. Diversamente dall'Elettronica, che affida alla carica dell'elettrone la codifica binaria, la Spintronica prende in considerazione sia la carica sia il momento di spin degli elettroni. Tale connubio tra carica e spin consente agli spin di influenzare il trasporto degli elettroni, e, viceversa, alle cariche elettriche di modificare le proprietà magnetiche. In questo modo, si sono resi possibili la progettazione e fabbricazione di dispositivi caratterizzati da dimensioni nanometriche, basso consumo di energia, non-volatilità, alta velocità, grande scalabilità e compatibilità con l'odierna industria elettronica.

I dispositivi spintronici sono tipicamente composti da un tristato dove un materiale non magnetico è frapposto tra due ferromagneti. La magnetizzazione di uno di essi può essere manipolata, non soltanto tramite l'applicazione di campi esterni, bensì anche per mezzo di una corrente elettrica che fluisce perpendicolarmente al multistrato. Questo grado di libertà aggiuntivo nel controllo delle dinamiche della magnetizzazione ha dato vita a molteplici applicazioni tecnologiche dei dispositivi spintronici, come memorie magnetiche, le quali sono state già commercializzate, oscillatori alle frequenze delle microonde, che sono gli oscillatori più piccoli esistenti in natura, e rilevatori a microonde, la cui sensitività ha già superato quella dei diodi Schottky.

Una strategia per migliorare le prestazioni dei dispositivi spintronici concerne l'uso di configurazioni non uniformi della magnetizzazione, tra le quali gli skyrmion hanno mostrato caratteristiche promettenti. La principale peculiarità è la protezione topologica, che rende gli skyrmion molto stabili e difficili da essere distrutti.

Questa tesi descrive i risultati ottenuti mediante simulazioni micromagnetiche sulle memorie magnetiche, oscillatori e rivelatori alle frequenze delle microonde basati sia sullo stato uniforme della magnetizzazione, sia sullo skyrmion.

ABSTRACT

Spintronics is a branch of Physics which has attracted a lot interest over the past 30 years. Differently from Electronics, that entrusts the binary encode to the electron charge, Spintronics considers both charge and spin momentum of electrons. This bond between electron charge and spin allows to alter the electronic transport by spins, and, vice versa, to affect the magnetic properties by electron charges. In this way, it has been possible to design and make devices characterized by nanometer dimensions, low energy consumption, non-volatility, large speed, high scalability, and compatibility with nowadays' electronic industry.

Spintronic devices are typically composed of a trilayer where a non-magnetic spacer is sandwiched between two ferromagnets. The magnetization of one of them can be manipulated, not only by external applied fields, but also by an electrical current perpendicularly injected into the stack. This additional degree of freedom in controlling the magnetization dynamics has given rise to several technological applications of spintronic devices, as magnetic storages, which have been already commercialized, microwave oscillators, which are the smallest oscillators existing in nature and microwave detectors, whose sensitivity has already overcome the one of Schottky diodes.

A strategy to improve the performances of spintronic devices concerns the use of non-uniform configurations of the magnetization, among them skyrmions have shown promising features. The main characteristic is the topological protection which makes skyrmions very stable and hard to be wrecked.

This thesis shows the results achieved by means of micromagnetic simulations on magnetic storages, microwave oscillators and detectors based on both a uniform and a skyrmion state of the magnetization.

ACKNOWLEDGEMENTS

During my Master Degree, my colleagues and I, Angelo and Domenico, used to imagine working for a big company after graduating. However, my life did not go in the direction I expected. I attended a course on Magnetic Materials and Spintronics, taught by Prof. Giovanni Finocchio, who involved me in a deeper study of Spintronics and encouraged me to continue my studies. His first words to me were: "Riccardo, la cosa più importante è scrivere articoli!! (Riccardo, the most important thing is to write papers)". I owe a lot to Giovanni, from his guidance, indispensable support, useful work suggestions, valuable comments on different aspects of my research to his general advices for everyday life; because, as well as being an amazing professor, he is a great man and friend. His support his essential to my success. I can still feel my enthusiasm when he proposed me to spend almost two months at the University of Irvine, California, with Prof. Ilya Krivorotov and his group. I packed my stuff, and, with the few English words I knew at that time, I travelled all the way to California by myself, without an accommodation and not knowing anyone. It was a tough and crazy experience. I took the first serious contact with the world of Research and it helped me grow personally and professionally.

When I returned from the USA, I applied for the PhD position under the supervision of Prof. Mario Carpentieri. I have learned oodles of things from him: how to organize my work, tutor students, teach classes, write a paper, and much more. He is such an excellent person, supervisor and professor. I'm fully indebted to him for his understanding, guidance, encouragement, indispensable advice and information over the last three years and for pushing me farther than I thought I could go. The only thing I'm afraid of is not being up to his standards, since his most frequent sentence is: "Riccardo, sei sempre in vacanza!!! (Riccardo, you are always on vacation)".

Besides being grateful towards those two mentors, I'm glad to have met great educators such as Prof. Domenico Grimaldi, Prof. Luca Carnì,

Prof. Francesco Lamonaca, Prof. Sergio Greco, Prof. Felice Crupi and Prof. Marco Lanuzza towards whom I'm really thankful for their kindness, assistance and support.

I cannot avoid mentioning my first trip to Salamanca. I feel very privileged to have worked at the University of Salamanca under the supervision of kind and illustrious professors: Prof. Luis Torres, Prof. Eduardo Martinez and Prof. Luis Lopez-Diaz, and, more in general, I'm very happy and grateful to have been in Salamanca. I spent one of the most wonderful periods of my life there, both from a work achievement point of view and from a life-experience one. For this reason, I want to also thank all my Salamanca friends, especially my best friend David, Vincent, and Ignacio, as well as all the members of the group "Addicts to O'hara's".

I also want to acknowledge Prof. Ozhan Ozatay and his group (especially Vedat and Aisha) for the beautiful time spent at Bogazici University in the magic and chaotic Istanbul.

Another important step for my career and experience has been my attendance at the Magnetics Summer School in Minneapolis, Minnesota, which made me very proud of my research achievements since I was the only PhD student from Italy there.

Let's rewind to the beginning, because all this would have not been possible without meeting the charismatic Prof. Bruno Azzerboni and his fabulous group, above all my friends Vito and Anna, and the meticulous Giulio. It has been an honor collaborating with them and a pleasure as well, because, within this group, it is always possible to work with "a smile on your face". In Prof. Azzerboni words: "Tenete alto il nome del gruppo divertendovi!"(Keep high the name of the group, having fun).

I also express my deep sense of gratitude to my best friend Nunzio, who has always been by my side supporting me (i.e. He accompanied me for the admission exam for the PhD) and of course my amazing parents, for their co-operation, understanding and constant encouragement which were the sustaining factors to carry out this work successfully. Thank you, mom and dad, for your support, for giving me strength and your love, throughout

my studies in all the ways possible. I hope this thesis would be a worthy reward for what you have done for me.

Lastly, it is my privilege to conclude the acknowledgments mentioning my girlfriend, who is the most important gift Salamanca has given me. I am extremely thankful for her constant support and encouragement throughout my research period and for helping me improve my English. I hope to continue sharing my life with her for a long time.

TABLE OF CONTENTS

1. BASIC CONCEPTS 1

1.1 Micromagnetism 1

1.1.1 Exchange energy 3

1.1.2 Uniaxial Anisotropy energy 3

1.1.3 Magnetostatic energy 4

1.1.4 Zeeman energy 6

1.2 Equilibrium and dynamical equations 7

1.2.1 Oersted Field 8

1.2.2 Thermal Field 8

1.2.3 Dynamical equation 9

1.2.4 Spin-Transfer Torque 11

1.2.5 STT in OOP devices 12

1.2.6 STT in IP devices 14

1.2.7 Voltage controlled magnetocrystalline anisotropy (VCMA) 15

1.3 Spin-orbit interactions 16

1.3.1 Spin-Hall Effect 19

1.3.2 Rashba effect 21

1.3.3 Dzyaloshinskii-Moriya Interaction 22

1.3.4 Three terminal MTJ device 23

1.4 Magnetic skyrmions 24

1.4.1 Topology and skyrmion number 25

1.4.2 Observations of skyrmions 27

2. MAGNETIC MEMORIES: STT-MRAM AND RACETRACK 29

2.1 MTJ based STT-MRAM 29

2.1.1 Tunnel MagnetoResistance 30

2.1.2 Writing and reading process 32

2.1.3 Thermal stability and writing energy 34

2.1.4 State of the art 35

2.1.5 Comparison with other technologies 37

2.2 Results on STT-MRAMs 39

2.2.1 Switching Properties in Magnetic Tunnel Junctions With Interfacial Perpendicular Anisotropy: Micromagnetic Study 39

2.2.2 Micromagnetic Study of Electrical-Field-Assisted Magnetization Switching in MTJ Devices 47

2.3 Racetrack memory 55

2.4 Results on racetrack memories 57

2.4.1 A strategy for the design of skyrmion racetrack memories 57

3. SPIN-TORQUE OSCILLATORS AND DIODES 67

3.1 Introduction on oscillators 67

3.2 Spin-torque nano-oscillators 69

3.2.1 Classification of STNOs 70

3.2.2 State of the art 74

3.3 Results on STNOs 76

3.3.1 Dynamical properties of three terminal magnetic tunnel junctions: spintronics meets spin-orbitronics 76

3.3.2 Intrinsic synchronization of an array of spin-torque oscillators driven by the spin-Hall effect 83

3.4 Spin-torque diode 87

3.4.1 Spin-torque diode effect in MTJs 88

3.4.2 State of the art 90

3.5 Results on Spin Torque Diode 92

3.5.1 Influence of the Dzyaloshinskii-Moriya interaction on the spin-torque diode effect 92

4. SPIN-TORQUE OSCILLATOR AND DIODE BASED ON SKYRMION 97

4.1 Topological, non-topological and instanton droplets driven by STT in materials with perpendicular magnetic anisotropy and DMI 97

4.2 Skyrmion based microwave detectors and harvesting 107

5. JOURNAL ARTICLES 116

5.1 Published articles 116

5.2 Submitted articles 118

BIBLIOGRAPHY 119

LIST OF ABBREVIATIONS

AHE	Anomalous Hall Effect;
AMR	Anisotropic Magnetoresistance;
AP	Antiparallel;
AV	Anti-Vortex;
BC	Boundary conditions
BIA	Bulk Inversion Asymmetry;
CMOS	Complementary Metal-Oxide Semiconductor;
DMI	Dzyaloshinskii-Moriya Interaction;
DRAM	Dynamic Random Access Memory;
DW	Domain-Wall;
FM	Ferromagnetic;
FMR	Ferromagnetic Resonance;
FWHM	Full Width at Half Maximum;
GMR	Giant MagnetoResistance:
HM	Heavy Metal;
ID	Instanton Droplet;
i-DMI	Interfacial Dzyaloshinskii-Moriya Interaction;
IP	In-Plane;
IPA	Interfacial Perpendicular Anisotropy;
LLG	Landau-Lifshitz-Gilbert;
LLGS	Landau-Lifshitz-Gilbert-Slonczewski;
MRAM	Magnetic Random Access Memory;
MSMDMT	Micromagnetic Spectral Mode Decomposition Mapping Technique;
MTJ	Magnetic Tunnel Junction;
MWS	Micromagnetic Wavelet Scalogram;
NTD	Non Topological Droplet;
OOP	Out-Of-Plane;

P	Parallel;
SCD	Switching Current Density;
SHE	Spin-Hall Effect;
SIA	Structural Inversion Asymmetry;
SMD	Spatial Mode Distribution;
SOC	Spin-Orbit Coupling;
SOT	Spin-Orbit Torque;
SRAM	Static Random Access Memory;
SS	Static Skyrmion;
STD	Spin-Torque Diode;
STNO	Spin-Torque Nano-Oscillator;
STT	Spin-Transfer-Torque;
STT-MRAM	Spin-Transfer-Torque-Magnetic Random Access Memory;
TD	Topological Droplet;
TMR	Tunnel MagnetoResistance;
V	Vortex;
VCMA	Voltage Controlled Magnetocrystalline Anisotropy;
WA	Wavelet Analysis;

LIST OF SYMBOLS

dV	volume of magnetic material;
$\mathbf{r}$	vector position;
$\mathbf{M}$	magnetization vector;
M_S	saturation magnetization;
$\boldsymbol{\mu}$	spin angular momentum;
$\mathbf{m}$	normalized magnetization vector;
ε_{ex}	exchange energy density;
A	exchange constant;
m_x	x-component of the normalized magnetization;
m_y	y-component of the normalized magnetization;
m_z	z-component of the normalized magnetization;
ε_{an}	uniaxial anisotropy energy density;
k_1 or k_u	first order uniaxial anisotropy constant;
k_2	second order uniaxial anisotropy constant;
k_3	third order uniaxial anisotropy constant;
$\mathbf{u_k}$	unit vector of the magnetization easy axis;
$\mathbf{H_m}$	magnetostatic field;
$\mathbf{B}$	magnetic induction;
μ_0	vacuum permeability;
ρ_m	volume magnetic charge density;
U_m	scalar potential;
$\mathbf{n}$	normal unit vector;
$\sigma_m(\mathbf{r})$	surface magnetic charge density;
ε_m	magnetostatic energy density;
N_x	x-axis shape-dependent demagnetizing factor;
N_y	y-axis shape-dependent demagnetizing factor;

N_z	z-axis shape-dependent demagnetizing factor;
$\mathbf{H_{ext}}$	external magnetic field;
ε_{ext}	external magnetic field energy density;
ε_{tot}	total energy density of a ferromagnetic body;
$\mathbf{H_{eff}}$	effective field;
$\mathbf{h_{eff}}$	normalized effective field;
$\mathbf{H_{Oe}}$	Oersted field;
T	material temperature;
$\mathbf{H_{th}}$	stochastic thermal field;
K_B	Boltzmann constant;
ΔV	volume of the computational cell;
Δt	simulation time step;
$\boldsymbol{\xi}$	three-dimensional white Gaussian noise;
$\boldsymbol{\tau}$	torque;
$\mathbf{L}$	orbital angular momentum;
γ	gyromagnetic ratio;
g	Landé factor;
e	electron charge;
m_e	electron mass;
μ_B	Bohr magneton;
$\hbar$	Planck's constant;
α	damping parameter or Gilbert damping;
$\mathbf{j_{FE\text{-}oop}}$ or J	perpendicular current density;
J_{MTJ}	perpendicular current density in MTJ;
$\mathbf{m_p}$	normalized magnetization of the pinned layer;
$\mathbf{m_f}$	normalized magnetization of the free layer;
$\boldsymbol{\tau_{oop}}$	STT in OOP device;
t or t_{FE}	thickness of the ferromagnet;

$\varepsilon(\mathbf{m_f}, \mathbf{m_p})$	polarization function;
$\varepsilon_{SV}(\mathbf{m_f}, \mathbf{m_p})$	polarization function for spin-valve;
η	spin polarization factor for OOP device;
$\varepsilon_{MTJ}(\mathbf{m_f}, \mathbf{m_p})$	polarization function for MTJ;
$d\tau$	dimensionless time step;
$\mathbf{j_{FE\text{-}ip}}$ or j_{FE}	IP current density through ferromagnet;
$\boldsymbol{\tau}_{\mathbf{IP}}^{a}$	adiabatic torque for IP device;
P	spin polarization factor for IP device;
$\boldsymbol{\tau}_{\mathbf{IP}}^{na}$	non-adiabatic torque for IP device;
β	non-adiabatic parameter;
$\mathbf{H}_{\mathbf{k}\perp}$	perpendicular anisotropy field;
V_{app}	applied voltage;
H_{SO}	Spin-orbit Hamiltonian;
$V(\mathbf{r})$	electrical potential;
$\boldsymbol{\tau}_{\mathbf{SHE}}$	SHE torque;
θ_{SH}	spin-Hall angle;
j_{HM}	charge current density through a HM;
j_s	spin current;
$\mathbf{h_R}$	Rashba effective field;
$\boldsymbol{\tau}_{\mathbf{R}}$	Rashba torque;
α_R	Rashba parameter;
$\varepsilon_{BulkDMI}$	Bulk DMI energy density;
D	DMI parameter;
$\varepsilon_{InterDMI}$	Interfacial DMI energy density;
ξ	DMI characteristic length;
S	skyrmion number;

R_P	Parallel electrical resistance of OOP device;
R_{AP}	AP electrical resistance of OOP device;
J_C	switching current density;
J_C^{ip}	switching current density for IP MTJ;
H_k	anisotropy field;
J_C^{oop}	switching current density for OOP MTJ;
I	electrical current;
Δ	thermal stability factor;
k_{eff}	effective anisotropy constant;
V	magnetic volume of ferromagnet;
$\mathbf{H_{Keff}}$	effective anisotropy field;
E_w	write energy;
t_p	current pulse width;
S	cross section of the free layer;
l	length or diameter of a ferromagnet (or free layer cross section);
$\mathbf{h_{IPA}}$	IPA effective field contribution;
dt	time step;
$<m>$	average normalized magnetization;
$\mathbf{G}$	gyrocoupling vector;
v_x	x-component of the velocity of DW or skyrmion;
v_y	y-component of the velocity of DW or skyrmion;
$\ddot{\mathcal{D}}$	dissipative tensor;
$\ddot{\mathcal{R}}$	IP rotation matrix;
D_g	roughness size;
Δy_2	y-position of a skyrmion in a racetrack memory;
w	ferromagnet width;
Δx_1	travelling x-distance of a skyrmion in a racetrack memory;
η_p	power efficiency;

P_{out} or p_{out}	output power;
P_{in}	input power;
Q	quality factor;
f_0	FMR frequency;
R	electric resistance of an OOP device;
R_m	average resistance value;
ΔR or ΔR_S	amplitude of the oscillating resistance;
ω	angular frequency;
ϕ	intrinsic phase shift;
V_{out} or v_{out}	output voltage;
R_L	resistance of an inductive load;
$M_{\max}$	amplitude of the magnetization oscillation;
J_{th}	Threshold current density for persistent magnetization oscillations;
j_{MTJrf}	perpendicular microwave current density in MTJ;
J_{MAX}	perpendicular microwave current density amplitude in MTJ;
f_{rf}	perpendicular microwave current density frequency in MTJ;
Δ_{L}	locking range;
ω_{S}	synchronization angular frequency;
V_M	amplitude of the applied voltage;
R_0	resistance load;
G_{i}	conductance of *i*-MTJ;
$G_{m,\mathrm{i}}$	average conductance value of *i*-MTJ;
ΔG_{i}	amplitude of the conductance of *i*-MTJ;
t_{HM}	thickness of HM;
i_{MTJrf}	perpendicular microwave current in MTJ;
φ_I	intrinsic phase shift of i_{MTJrf} ;

φ_R	intrinsic phase shift of R;
V_{dc}	dc output voltage;
Φ_S	phase difference;
ε	diode sensitivity;
d_{c}	contact diameter;
D_{c}	critical i-DMI parameter;
r_{min}	minimum radius of the skyrmion;
r_{max}	maximum radius of the skyrmion;
r_c	contact radius;
d_{SK}	skyrmion diameter;
$d_{SK\text{-}min}$	minimum diameter of the skyrmion;
$d_{SK\text{-}max}$	maximum diameter of the skyrmion;
H_{VCMA}	VCMA effective field contribution;
ΔH_{VCMA}	Amplitude of the effective field contribution.

LIST OF FIGURES

Fig. 1.1: fundamental assumption of Micromagnetics, by which the magnetic momenta $\boldsymbol{\mu}_i$ of a volume element dV can be represented by a magnetization vector $\mathbf{M}$ 3

Fig. 1.2: (a) persistent precession of the magnetization $\mathbf{M}$ around the effective field $\mathbf{H}_{eff}$ when only the conservative torque acts. (b) Damped precession of the magnetization when the damping torque is considered... 10

Fig. 1.3: schematic representation of the creation of the spin-polarized current. Part of the entering spins in the ferromagnet1 are polarized in the same direction of $\mathbf{M}_1$, generating the spin-polarized current, which will transfer a spin-torque onto the magnetization $\mathbf{M}_2$ of the adjacent ferromagnet2. Part of the entering spins is reflected with a polarization opposite to $\mathbf{M}_1$. 11

Fig. 1.4: (a) schematic illustration of the spin-transfer torque exerted on the free layer magnetization in an OOP device. (b) representation of all the torques acting on the magnetization. 14

Fig. 1.5: schematic representation of two domains (UP and DOWN) separated by a domain wall. A non-polarized electron flowing through this magnetization configuration will change the direction of its spin adiabatically, namely it will follow the local magnetization orientation..... 15

Fig. 1.6: variation of the effective perpendicular anisotropy field when a voltage is applied in CoFeB-MgO MTJs [29]. 16

Fig. 1.7: schematic picture of (a) the skew scattering mechanism and (b) the side-jump mechanism. The letters U and D refer to the sign of the spin, respectively spin-UP and spin-DOWN. The yellow circle represents an impurity..... 18

Fig. 1.8: (a) example of crystalline lattice characterized by the inversion symmetry property. (b) Example of crystalline lattice lacking the inversion symmetry. 19

Fig. 1.9: schematic picture of the FM/HM bilayer, where the SHE arises, inducing opposite spin accumulations near the upper and lower surface of the HM. 19

Fig. 1.10: the Rashba effect arises in FM/HM bilayers, when the electrical current flows through the ferromagnet. 21

Fig. 1.11: (a) bulk DMI vector originating in a non-centrosymmetric crystal because of the interaction of the ferromagnetic atoms with an impurity with large SOC. (b) Interfacial DMI vector in a FM/HM bilayer. 22

Fig. 1.12: schematic representation of a three terminal device, where an MTJ is coupled through its free layer to a HM underlayer..... 24

Fig. 1.13: magnetization configurations with skyrmion number *S* equal to (a) zero, (b) one, and (c) two [54]..... 26

Fig. 1.14: magnetization distribution of a (a) Bloch skyrmion and (b) Néel skyrmion [47]..... 27

Fig. 2.1: schematic illustration of the TMR phenomenon in MTJs, where in (a) the magnetization state is parallel, allowing many spin-UP electrons to tunnel from the pinned layer to the free layer, in (b) the magnetization state is AP and just few spin-UP electrons can tunnel, leading to a high resistance of the MTJ. In the bottom panels, the density of states at Fermi level are represented, corresponding to the two ferromagnets in the two magnetization configurations..... 31

Fig. 2.2: schematic representation of a MTJ connected in series with a selection transistor. 33

Fig. 2.3: schematic illustration of (a) an IP MTJ and (b) an OOP one. 34

Fig. 2.4: schematic representation of the studied MTJ. 40

Fig. 2.5: IP SCD depending on the perpendicular anisotropy. The three curves with symbols refer to a saturation magnetization equal to $8x10^5$ A/m, $10x10^5$ A/m and $12x10^5$A/m. The green line without symbols represents the minimum values of IPA over which, for a fixed M_S, the free layer is OOP. 41

Fig. 2.6: representation of the spin magnetization domains of the MTJ elliptical section, describing the IP switching phenomenon, when the spins are oriented along (a) -*x* and (c) *x* and (b) during the switching..... 42

Fig. 2.7: IP SCD as function of the perpendicular anisotropy, without the Oersted field. The two curves refer to a saturation magnetization equal to $10x10^5$ A/m and $12x10^5$A/m..... 43

Fig. 2.8: IP SCD depending on the perpendicular anisotropy, without the Oersted field and for a reversal time of 10 ns The three curves refer to a saturation magnetization equal to $8x10^5$ A/m, $10x10^5$ A/m and $12x10^5$A/m. 43

Fig. 2.9: OOP SCD as function of the perpendicular anisotropy, for a switching time of (a) 10 ns and (b) 5 ns. The curves refer to a saturation magnetization equal to $8x10^5$ A/m, $10x10^5$ A/m and $12x10^5$ A/m..... 44

Fig. 2.10: IP SCD as function of the perpendicular anisotropy, without the Oersted field and for a reversal time of 20 ns at a temperature T=350 K. The three curves refer to a saturation magnetization equal to $8x10^5$ A/m, $10x10^5$ A/m and $12x10^5$A/m..... 45

Fig. 2.11: switching averaged energy as function of the IPA for (a) the IP switching, (b) OOP switching in 10 ns and (c) OOP switching in 5 ns. 46

Fig. 2.12: Sketch of the studied MTJ device. 49

Fig. 2.13: (a) applied current pulses. (b) Time domain plot of the three normalized components of the magnetization ($<m_x>$, $<m_y>$ and $<m_z>$, respectively represented in blue, red and black) during a whole reversal process (P→AP and AP→P) as a function of the current pulses in (a)..... 50

Fig. 2.14: time domain plot for the three normalized components of the magnetization $<m_x>$, $<m_y>$ and $<m_z>$, respectively represented in blue, red and black. (a) Pulse time of 3 ns. (b) Pulse time of 2.6 ns. 51

Fig. 2.15: spatial magnetization configurations before the current pulse is switched off. The arrows refer to the *y*-component of the magnetization (blue positive and red negative), whereas the background colors refer to the *z*-component (red positive direction and blue negative direction). The letter "V" indicates vortexes, while "AV" refers to antivortexes. (a) Pulse time of 3 ns. (b) Pulse time of 2.8 ns. (c) Pulse time of 2.6 ns. (d) Pulse time of 3.4 ns. (e) Spatial magnetization configuration after the current pulse is removed for a pulse time (e) t=3 ns and (f) t=2.6 ns. 53

Fig. 2.16: time domain plot for the *z*-component of the magnetization for different time pulses at T=300 K. (a) P→AP switching process. (b) AP→P switching process. 54

Fig. 2.17: evolution of DW racetrack memory. (a) and (b) represent a single ferromagnetic wire with IP and OOP domains, respectively. (c) bilayer where the DW motion is induced by the SHE. (d) motion of DWs due to the SHE in a synthetic antiferromagnet. 56

Fig. 2.18: (a) Néel skyrmion motion driven by the STT. (b) Néel skyrmion motion driven by the SHE. (c) Bloch skyrmion motion driven by the STT. (d) Bloch skyrmion motion driven by the SHE. The four insets show the spatial distribution of the Néel and Bloch skyrmion, where the background colors refer to the *z*-component of the magnetization (blue negative, red positive), while the arrows are related to the IP components of the magnetization. The current flows along the *x*-direction. The skyrmion moves along the *x*-direction in the scenarios A, C, and D and along the *y*-direction in the scenario B. 58

Fig. 2.19: (a) A comparison among the skyrmion velocities obtained for each scenario (A, B, C, and D). The current j_{FE} is related to the scenarios A

and C while j_{HM} to the scenarios B and D. (b) Sketch of the motion mechanism of the Néel skyrmion driven by the SHE along the *y*-direction. (c) Sketch of the motion mechanism of the Bloch skyrmion driven by the SHE along the *x*-direction. (d) Skyrmion velocities as a function of j_{HM} obtained for the scenario B: (i) thermal fluctuations (T=350 K) and perfect strip (red curve) and (ii) thermal fluctuations (T=350 K) and rough strip (blue curve). The arrows for (b) and (c) refer to the IP components of the magnetization, the spin-polarization of j_{HM} is also displayed..... 61

Fig. 2.20: (a) phase diagram (*i*-DMI parameter vs. external field) of the skyrmion stability. The colored part highlights the region where the skyrmion is stable and the red curve points out the values of D and H_{ext} for which the skyrmion diameter is 46 nm. (b) Skyrmion velocity as a function of the current calculated by micromagnetic (black curve) and analytical computations (green line). (c) Time domain evolution of the skyrmion diameter during the transient breathing mode at three different values of the j_{HM}, 30 MA/cm^2 (black curve), 40 MA/cm^2 (blue curve) and 50 A/cm^2 (red curve). (d) A comparison of skyrmion velocity as a function of the current for an ideal strip (T=0K) and a rough strip and room temperature..... 63

Fig. 2.21: (a) sketch of the skyrmion motion due to the SHE in a sample confined along the *y*-direction. (b) Skyrmion velocity (*x*-direction) as a function of the current: (i) no thermal fluctuations and perfect strip (red curve) and (ii) thermal fluctuations (T=350 K) and rough strip (black curve). (c) Skyrmion velocity as a function of the current when the strip width w is 100 nm (red curve), 150 nm (black curve) and 200 nm (blue curve). The colors for (a) refer to the *z*-component of the magnetization (blue negative, red positive). 65

Fig. 3.1: (a) schematic illustration of an STNO. (b) example of time domain oscillation of the STNO electrical resistance, when precessions of the free layer magnetization are excited. 70

Fig. 3.2: (a) and (b) geometry classification of STNOs, (a) nanopillars and (b) nano-contact. (c), (d) and (e) magnetization configuration classification of STNOs, (c) in-plane, (d) perpendicular and (e) in-plane-perpendicular. 71

Fig. 3.3: example of MTJ-based nanopillar STNO spectra showing a narrow linewidth at room temperature [23]. 74

Fig. 3.4: schematic representation of the three terminal MTJ device..... 78

Fig. 3.5: (a) oscillation frequency of the magnetization as a function of the j_{HM} for H_{ext}=40 mT (top curve) and H_{ext}=30 mT (bottom curve) when the J_{MTJ} is zero. (b) Temporal evolution of the three normalized components of the magnetization $<m_x>$ (dashed curve), $<m_y>$ (solid curve), $<m_z>$ (dotted curve) during 1 ns of the magnetization oscillations, for j_{HM} =-2.13x10^8 A/cm^2, H_{ext}=30 mT. (c) Snapshots of the magnetization during an oscillation period in the time instants reported in Fig. 3.5(b). The color scale refers to the *y*-component of the magnetization (red positive, blue negative). The arrows indicate the magnetization direction. 79

Fig. 3.6: (a) oscillation frequency for fixed H_{ext}=30 mT and j_{HM} =-2.13 x 10^8 A/cm^2 as function of the bias J_{MTJ}. (b) Fourier spectra for different values of the J_{MTJ}. (c) Arnold tongues showing the locking regions as function of J_{MAX} for T=0 K (lower curve) and T=300 K (upper curve) at j_{HM}=-2.13 x 10^8 A/cm^2. 80

Fig. 3.7: (a) schematic representation of the proposed highly scalable synchronization scheme. (b) Locking ranges as a function of the cross-section dimensions for J_{MAX}=2.0 x 10^6 A/cm^2 and j_{HM} =-2.13 x 10^8 A/cm^2.83

Fig. 3.8: schematic representation of the FM/HM bi-layered device. (Inset) Detailed sketch of the bylayer structure showing the thicknesses of the layers, the direction of the current density j_{HM} and the applied external magnetic field H_{ext}. 84

Fig. 3.9: Fourier spectra as a function of j_{HM}. (a) H_{ext}=80 mT. (b) H_{ext}=90 mT. 85

Fig. 3.10: Fourier spectra as a function of H_{ext}. (a) j_{HM}=-0.90x10^8 A/cm^2, (b) j_{HM}=-1.00x10^8 A/cm^2. 86

Fig. 3.11: MWS for H_{ext}=90 mT, where the power increases from white to black. (a) j_{HM}=-0.90x10^8 A/cm^2, (b) j_{HM}=-1.00x10^8 A/cm^2. Insets: SMDs related to the *x* component of the magnetization (the power increases from white to red). 87

Fig. 3.12: schematic representation of an STD working in the (a) IP regime and (b) in the OOP regime. 90

Fig. 3.13: comparison of STD sensitivities with the one of the Schottky diode [190]. 91

Fig. 3.14: FMR responses for j_{HM}=0 A/cm^2. a) J_{MAX}=0.5x10^6 A/cm^2 without *i*-DMI (top curve) and with *i*-DMI (bottom curve); b) J_{MAX}=0.1x10^6 A/cm^2 with no *i*-DMI (upper curve) and with *i*-DMI (lower curve). The insets represent the SMDs for the *y*- and *z*- components of the magnetization. 94

Fig. 3.15: FMR responses for a sub-critical j_{HM}=-1.50x10^7 A/cm^2 and a J_{MAX}=0.5x10^6 A/cm^2 without *i*-DMI (top curve) and with *i*-DMI (bottom curve). The insets represent the SMDs for the *y*- and *z*- components of the magnetization. 94

Fig. 3.16: FMR responses for j_{HM}=-1.40x10^8 A/cm^2. a) J_{MAX}=0.5x10^6 A/cm^2 without *i*-DMI (top curve) and with *i*-DMI (bottom curve); b) J_{MAX}=0.1x10^6 A/cm^2 with no *i*-DMI (upper curve) and with *i*-DMI (lower curve). The insets represent the SMDs for the *y*- and *z*- components of the magnetization. 95

Fig. 4.1: spin valve with a point contact geometry, where the Co free layer is coupled to the Pt underlayer. For the sake of clarity, an enlarged view of the nanocontact (fixed layer) and the diameter d_c of the nanocontact are illustrated, together with the dimensions $l \times l$ of the square cross section. . 99

Fig. 4.2: (a) stability phase diagram of the magnetization ground-state as a function of the modulus of the current density and of *D* at zero external

magnetic field. Letters A, B, C and D are linked to Fig. 4.4. The meaning of the symbols in the phase diagram are as follows. FM: ferromagnetic; SS: static skyrmion; TD: topological droplet; NTD: non-topological droplet, ID: instanton droplet. (b) Spatial distribution of the topological density (a color scale is represented, red +1, blue -1) for the three dynamical states NTD, TD, and ID at *i*-DMI values of 0.00, 2.50, and 1.25 mJ/m^2, respectively. 100

Fig. 4.3: (a) frequency-current density hysteresis loop at D=2.0 mJ/m^2: the black (red) arrows indicate the path where the initial state is FM (SS). (b) Output power as a function of current density for D=2.0 mJ/m^2. The solid line refers to the analytical computation from Eq. (4.1), while the dotted line is determined by micromagnetic calculations. The black (red) arrows indicate the path where the initial state is FM (SS). (c) Two dimensional spatial profile of the TD for D=2.5 mJ/m^2..... 103

Fig. 4.4: frequency spectra as a function of the *i*-DMI, when J=8.5x10^7 A/cm^2. Capital letters A, B, C, and D are linked to the phase diagram of Fig. 4.2. 104

Fig. 4.5: oscillation frequency as a function of D for J=8.5×10^7 A/cm^2. The different states are indicated. The inset shows the energy related to ID transitions as a function of D for J=8.5×10^7 A/cm^2..... 105

Fig. 4.6: frequency spectra as a function of the contact diameter d_c, when J=8.5x10^7 A/cm^2 and zero *i*-DMI, together with the spatial distribution of the topological density (red +1, blue -1) which corresponds to the frequency peak in the NTD dynamical state..... 106

Fig. 4.7: sketch of the device under investigation. The extended CoFeB acts as free layer while the top nano-contact made by CoFeB is the current polarizer (d_c is the contact diameter, l=100 nm). The Pt layer is necessary to introduce the *i*-DMI. 108

Fig. 4.8: (a) profile of the OOP component of the magnetization corresponding to the section AA', as indicated in the inset. d_{sx} represents the

skyrmion diameter. Inset: example of a snapshot of a Néel skyrmion stabilized by the *i*-DMI, where the arrows indicate the IP component of the magnetization while the colors are linked to the OOP component (blue negative, red positive). (b) and (c) Skyrmion diameter as computed by means of micromagnetic simulations (the radius is computed as the distance from the geometrical center of the skyrmion, where m_Z=-1 to the region where m_Z=0). Skyrmion diameter (b) as a function of D for k_u=0.8 and 0.9 MJ/m^3 and (c) as a function of k_u for D=3.0 and 3.5 mJ/m^2..... 109

Fig. 4.9: (a) STD response as a function of D for $k_{u.}$=0.8 MJ/m^3. (b) STD response as a function of $k_{u.}$ for D=3.0 mJ/m^2. (c) FMR frequency as a function of D for two different values of k_u as indicated in the panel. (d) FMR frequency as a function of D ($k_{u.}$=0.8 MJ/m^3) for three different values of the cross section diameter l=75, 100, and 150 nm with the indication of the critical DMI parameter D_{crit}. 111

Fig. 4.10:(a) sensitivity as a function of the contact diameter for different amplitudes of the microwave current as indicated in the main panel. (b) Detection voltage and microwave power as a function of the contact diameter for J_{MAX} =1 MA/cm^2. (c) Sensitivity as a function of the contact diameter for different microwave powers as indicated in the main panel. In both (a) and (c) an optimal contact diameter corresponding to a maximum in the sensitivity can be observed. (d) Detection voltage as a function of the contact diameter for different microwave powers. All the data reported in this figure are obtained for k_u=0.8 MJ/m^3 and D=3.0 mJ/m^2. 113

Fig. 4.11: (a) amplitude of the *z*-component of the magnetization driven by ΔH_{VCMA} at J_{MAX} =0 MA/cm^2; (b) sensitivity as a function of the ΔH_{VCMA}, considering the optimal contact diameter of Fig. 4(a) (d_C=40 nm), computed for J_{MAX} =1 and 2 MA/cm^2. (c) Phase shift Φ_S as a function of ΔH_{VCMA} for the same microwave currents amplitudes of (b). 114

LIST OF TABLES

Table 2.1: comparison of storage technologies [99]…….38

To my parents

1. BASIC CONCEPTS

In this chapter, several aspects concerning Micromagnetics, Spintronics, Spin-Orbitronics will be reviewed, in order to provide the basic background necessary to read the results of this thesis. First of all, a brief introduction of the micromagnetic formalism (paragraph 1.1) and the torques acting onto the magnetization vector of a ferromagnetic material (paragraph 1.2) will be presented. Paragraph 1.3 will deal with the key concepts of Spin-Orbitronics and, the last paragraph 1.4 will introduce the magnetic texture of the skyrmion.

1.1 Micromagnetism

Micromagnetism is a continuum field theory [1, 2, 3] which aims at the study of static and dynamical properties of ferromagnetic particles within a mesoscopic level. In other words, the characteristic scale of investigation is larger than the atomic one (10^{-10} – 10^{-9} m), but small enough to describe the internal structure of magnetic domains and domain walls (DWs).

The history of Micromagnetics starts in 1935 with a paper by Landau and Lifshitz [4, 5] on the structure of a wall between two antiparallel (AP) domains, and continues with Brown [6, 7] and many others up to nowadays. For many years, Micromagnetics was only used to

determine nucleation processes of domains, domain structures properties [8] and magnetization dynamics in simple and ideal systems. However, since the middle of 1980s, with the development of large-scale computations, Micromagnetics acquired more and more importance for the possibility to investigate realistic problems which were more amenable to be compared with experimental data [9, 10].

One of the fundamental assumptions of the micromagnetic theory is that the magnetization of a volume of material *dV*, denoted by the vector position **r**, can be represented as a vector **M**, which is a continuous function of the position **r** and has a modulus M_S constant in time (M_S is the saturation magnetization of the material). In particular, the size of the volume *dV* has to be chosen big enough to contain a large number *n* of magnetic momenta $\boldsymbol{\mu}_i$, but small enough to allow the magnetization vector to smoothly change between each volume element (Fig. 1.1). In this way, the magnetization can be locally expressed by:

$$\mathbf{M}(\mathbf{r},t) = \frac{\sum_{i=1}^{n} \boldsymbol{\mu}_i}{dV} \tag{1.1}$$

We can also refer to the normalized magnetization vector as: $\mathbf{m}(\mathbf{r},t) = \mathbf{M}(\mathbf{r},t)/M_S$ (in this thesis both notations $\mathbf{m}(\mathbf{r},t)$, $\mathbf{M}(\mathbf{r},t)$ or **m** and **M** will be used to indicate the magnetization). In order to obtain the equilibrium configurations of the magnetization **M**, it is necessary to introduce the fundamental energetic contributions, known as standard micromagnetic energies.

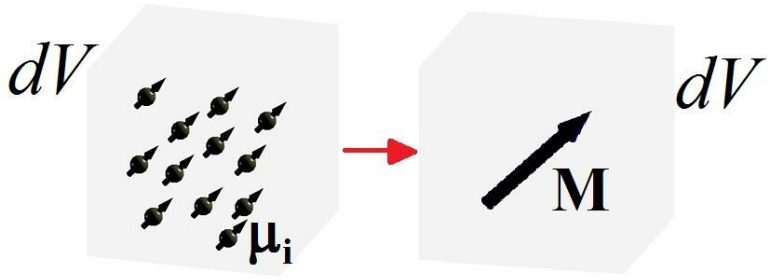

Fig. 1.1: fundamental assumption of Micromagnetics, by which the magnetic momenta $\boldsymbol{\mu}_i$ of a volume element dV can be represented by a magnetization vector $\mathbf{M}$.

1.1.1 Exchange energy

The exchange is a short-range interaction which tries to align neighboring magnetic momenta along the same direction [1, 7]. It is the basis of ferromagnetism and it has quantum-mechanical origins linked to the overlapping wave functions among electrons and to the Pauli exclusion principle. The volume energy density ε_{ex} related to the exchange is:

$$\varepsilon_{ex} = A\left[\left(\nabla m_x\right)^2 + \left(\nabla m_y\right)^2 + \left(\nabla m_z\right)^2\right] \tag{1.2}$$

being m_x, m_y, and m_z the three normalized components of the magnetization along the three spatial coordinates x, y, and z, respectively, and A is the exchange constant in J/m.

1.1.2 Uniaxial Anisotropy energy

It is well-known that in a crystalline lattice the magnetization vector tends to lie along preferential directions, which are called easy axes. On the other hand, the directions where the magnetization difficulty aligns are called hard axes. Therefore, the magnetocrystalline anisotropy energy [1, 7] can be defined as the energy surplus necessary to align the magnetization in a direction different from the easy one. The volume energy density ε_{an} related to the uniaxial anisotropy is:

$$\varepsilon_{an} = k_1 \sin^2\theta + k_2 \sin^4\theta + k_3 \sin^6\theta + \ldots \tag{1.3}$$

where k_1, k_2 and k_3 are uniaxial anisotropy constants expressed in J/m^3 and θ is the angle between the magnetization direction and the easy axis. Usually, only the first term is considered, leading to:

$$\varepsilon_{an} = k_1\left[1-\left(\mathbf{m}\cdot\mathbf{u_k}\right)^2\right] \tag{1.4}$$

being $\mathbf{u_k}$ the unit vector of the easy axis. If k_1 is positive, a minimum is obtained when the magnetization is parallel (P) or AP to the easy axis. If k_1 is negative, the plane perpendicular to the hard axis (defined in the direction $\mathbf{u_k}$) is an easy plane for the magnetization. In this thesis, also the symbol k_u is used to indicate the first order perpendicular anisotropy constant.

1.1.3 Magnetostatic energy

The magnetostatic energy is linked to the interactions among the magnetic dipoles inside the material [1]. The magnetostatic field $\mathbf{H_m}$ arising from those interactions is opposite to the internal magnetization **M**. For this reason, it is also known as *demagnetizing field*. If only **M** and $\mathbf{H_m}$ are taken into account, the magnetic induction **B** is equal to:

$$\mathbf{B}\left(\mathbf{r}\right) = \mu_0\left(\mathbf{M}(\mathbf{r}) + \mathbf{H_m}(\mathbf{r})\right) \tag{1.5}$$

where μ_0 is the vacuum permeability. In order to obtain the expression of $\mathbf{H_m}$, the Maxwell equations have to be considered [11]. Those equations, in absence of electrical fields, electrical currents, and considering only $\mathbf{H_m}$, are reduced to the following ones:

$$\begin{aligned} \nabla\cdot\mathbf{B}\left(\mathbf{r}\right) &= 0 \\ \nabla\times\mathbf{H_m}\left(\mathbf{r}\right) &= 0 \end{aligned} \tag{1.6}$$

and, using Eq. (1.5):

$$\begin{aligned} \nabla\cdot\mu_0\left(\mathbf{M}(\mathbf{r}) + \mathbf{H_m}(\mathbf{r})\right) &= 0 \\ \nabla\times\mathbf{H_m}\left(\mathbf{r}\right) &= 0 \end{aligned} \tag{1.7}$$

Since the curl of $\mathbf{H_m}$ is 0, it is possible to derive the magnetostatic field from a scalar potential U_m:

$$\mathbf{H_m}(\mathbf{r}) = -\nabla U_m(\mathbf{r}) \tag{1.8}$$

and, by including Eq. (1.8) into the first Eq. (1.7):

$$\nabla^2 U_m(\mathbf{r}) = -\nabla \cdot \mathbf{M}(\mathbf{r}) \tag{1.9}$$

where the quantity $-\nabla \cdot \mathbf{M}(\mathbf{r}) = \rho_m(\mathbf{r})$ plays a role of a volume magnetic charge density. Now, the boundary conditions, which determine the continuity of the normal component of **B** and of the tangential component $\mathbf{H_m}$ at the body surface, have to be considered:

$$\begin{cases} \mathbf{n} \cdot \left(\mathbf{B}(\mathbf{r})_{\mathbf{ext}} - \mathbf{B}(\mathbf{r})_{\mathbf{int}} \right) = 0 \\ \mathbf{n} \times \left(\mathbf{H}(\mathbf{r})_{\mathbf{d,ext}} - \mathbf{H}(\mathbf{r})_{\mathbf{d,int}} \right) = 0 \end{cases} \tag{1.10}$$

where **n** is a unit vector pointing outward from the surface.

In terms of the scalar potential, the corresponding conditions are:

$$\begin{cases} U_m(\mathbf{r})_{ext} = U_m(\mathbf{r})_{int} \\ \left. \frac{\partial U_m(\mathbf{r})}{\partial n} \right|_{ext} - \left. \frac{\partial U_m(\mathbf{r})}{\partial n} \right|_{int} = -\mathbf{M}(\mathbf{r}) \cdot \mathbf{n} \end{cases} \tag{1.11}$$

where the quantity $\mathbf{M}(\mathbf{r}) \cdot \mathbf{n} = \sigma_m(\mathbf{r})$ plays a role of a surface magnetic charge density. It is possible to notice that the surface of a magnetized body is influencing the overall response of a phenomenon having its origins at the atomic level. Finally, the expression for $\mathbf{H_m}$ can be written:

$$\mathbf{H_m}(\mathbf{r}) = \frac{1}{4\pi} \left[\int_{V'} \frac{(\mathbf{r} - \mathbf{r'}) \rho_m}{|\mathbf{r} - \mathbf{r'}|^3} dV' + \int_{S'} \frac{(\mathbf{r} - \mathbf{r'}) \sigma_m}{|\mathbf{r} - \mathbf{r'}|^3} dS' \right] \tag{1.12}$$

where *V'* and *S'* are the volume and surface of the body, respectively, and $|\mathbf{r} - \mathbf{r'}|$ is the distance between the points where the field is calculated (**r**) and where all other fields create magnetic momenta (**r'**). With the knowledge of $\mathbf{H_m}$, the magnetostatic energy density ε_m is calculated as:

$$\varepsilon_m = -\frac{1}{2} \mu_0 \mathbf{M} \cdot \mathbf{H_m} \tag{1.13}$$

The magnetostatic energy density is positive definite, hence volume charges and surface charges cannot compensate each other. This leads to Brown's pole avoidance principle, which states that a magnetic structure

tends to avoid magnetic charges. The tendency of the system to avoid surface charges often results in an alignment of magnetization with the surface. This effect is often referred to *shape anisotropy*, even though it is a pure magnetostatic effect, which is not related to crystalline anisotropy.

The magnetostatic energy competes with the uniaxial perpendicular anisotropy energy in fixing the easy axis of the magnetization. The magnetostatic energy depends on the geometrical properties of the ferromagnet as:

$$\mathbf{H_m} = -M_S \left(N_x m_x \hat{x} + N_y m_y \hat{y} + N_z m_z \hat{z} \right) \tag{1.14}$$

where N_x, N_y, N_z are the shape-dependent demagnetizing factors along the *x*, *y*, *z* directions, respectively. The demagnetizing factors sum to 1 and are smallest for directions along the longest dimensions of the magnetic element, meaning that the magnetization tries to be aligned along the longest dimension of the element. For a sphere, the demagnetizing factors are $N_x=N_y=N_z=1/3$ and there is no preferential direction that minimizes the magnetostatic energy. For an infinitely long cylinder, the demagnetizing factors perpendicular to the axis of the cylinder are 1/2, whereas 0 along the axis, hence the magnetization prefers to lie along the axis of the cylinder. However, if the uniaxial perpendicular anisotropy field overcomes the *z*-component of the magnetostatic field, the magnetization will align along the out-of-plane (OOP) direction. The competition between magnetostatic and uniaxial anisotropy field is fundamental for the control of the magnetization easy axis in spintronic devices.

1.1.4 Zeeman energy

The Zeeman energy is related to the application of an external magnetic field $\mathbf{H_{ext}}$. Its energy density ε_{ext} can be expressed as [1, 7]:

$$\varepsilon_{ext} = -\mu_0 \mathbf{M} \cdot \mathbf{H_{ext}} \tag{1.15}$$

1.2 Equilibrium and dynamical equations

It is necessary to understand the effect of each of the previous energetic contribution on the equilibrium configuration of the magnetization. In fact, every contribution favors different energetic minima and the final equilibrium state is given by the balance among them. Therefore, collecting together the energetic densities, the following expression for the free energy ε_{tot} of a generic ferromagnetic body is obtained:

$$\begin{aligned}\varepsilon_{tot} &= \varepsilon_{ex} + \varepsilon_{an} + \varepsilon_{m} + \varepsilon_{ext} = A\left[\left(\nabla m_x\right)^2 + \left(\nabla m_y\right)^2 + \left(\nabla m_z\right)^2\right] + \\ &+ k_1\left(1 - \left(\mathbf{m}\cdot\mathbf{u_k}\right)^2\right) - \frac{1}{2}\mu_0\mathbf{M}\cdot\mathbf{H_m} - \mu_0\mathbf{M}\cdot\mathbf{H_{ext}}\end{aligned} \tag{1.16}$$

By means of variational calculus, it is possible to define a particular field, called *effective field* [7], as the functional derivative of the total energy density:

$$\mathbf{H_{eff}} = -\frac{1}{\mu_0 M_S}\frac{\delta\varepsilon_{tot}}{\delta\mathbf{m}} \tag{1.17}$$

where the functional derivative is expressed by:

$$\frac{\delta}{\delta\mathbf{m}} = \frac{\partial}{\partial\mathbf{m}} - \nabla\cdot\frac{\partial}{\partial\left(\nabla\mathbf{m}\right)} \tag{1.18}$$

Hence, the total effective field is given by:

$$\mathbf{H_{eff}} = -\frac{2A}{\mu_0 M_S}\left(\nabla^2\mathbf{m}\right) - \frac{2k_1}{\mu_0 M_S}\left(\mathbf{m}\cdot\mathbf{u_k}\right)\mathbf{u_k} + \mathbf{H_m} + \mathbf{H_{ext}} \tag{1.19}$$

(we can also refer to the normalized effective field $\mathbf{h_{eff}}\left(\mathbf{r},t\right) = \mathbf{H_{eff}}\left(\mathbf{r},t\right)/M_S$).

As well as the four terms of the effective field related to the standard micromagnetic contributions, it is possible to consider other two additional terms to the effective field, linked to the Oersted field and the thermal field.

1.2.1 Oersted Field

It is well known that a flow of electric charges generates a magnetic field, known as Oersted field $\mathbf{H_{Oe}}$, which can calculated via the Maxwell equations:

$$\mathbf{H_{Oe}}(\mathbf{r}) = \frac{1}{4\pi}\left[\int_{V'} \mathbf{j}(\mathbf{r}') \times \frac{(\mathbf{r}-\mathbf{r}')}{|\mathbf{r}-\mathbf{r}'|^3} dV'\right] \tag{1.20}$$

where $\mathbf{j}(\mathbf{r}')$ is the current density which gives rise to $\mathbf{H_{Oe}}$. Indeed, the Oersted field acts as an external field, therefore the energy density ε_{Oe} has the same form as the Zeeman one:

$$\varepsilon_{Oe} = -\mu_0 \mathbf{M} \cdot \mathbf{H_{Oe}} \tag{1.21}$$

1.2.2 Thermal Field

In computational micromagnetics and other classical spin models, the interaction with the lattice is taken into account phenomenologically by means of a damping term in the dynamic equation and, in some cases, also by a random field representing thermal fluctuations. The amplitude of this random field is proportional to $\sqrt{T}$, where T is the lattice temperature. The effect of thermal fluctuations is included in the micromagnetic model following the Langevin formalism [12]. The thermal effect is considered as an additional stochastic term $\mathbf{H_{th}}$ to the deterministic effective field in each computational cell [13, 14]:

$$\mathbf{H_{th}} = \left(\xi / M_S\right)\sqrt{2\left(\alpha K_B T / \mu_0 \gamma_0 \Delta V M_s \Delta t\right)} \tag{1.22}$$

where K_B is the Boltzmann constant, ΔV is the volume of the computational cubic cell, Δt is the simulation time step, and ξ is a three-dimensional white Gaussian noise with zero mean and unit variance, and it is uncorrelated for each computational cell.

All the ingredients to study the magnetization dynamics have been described, and, thus, the Landau-Lifshitz-Gilbert equation can be introduced.

1.2.3 Dynamical equation

A homogeneous magnetic field $\mathbf{H_{eff}}$ acting on a magnetic momentum $\boldsymbol{\mu}$ exerts a torque $\boldsymbol{\tau}$ which, for definition, is equal to the time derivative of the angular momentum $\mathbf{L}$:

$$\boldsymbol{\tau} = \mu_0 \boldsymbol{\mu} \times \mathbf{H_{eff}} = \frac{d\mathbf{L}}{dt} \tag{1.23}$$

The relation between the angular momentum and the magnetic momentum is given by:

$$\frac{\boldsymbol{\mu}}{\mathbf{L}} = \gamma \tag{1.24}$$

where γ is the gyromagnetic ratio, expressed by:

$$\gamma = -\frac{ge}{2m_e} = -\frac{g\mu_B}{\hbar} \tag{1.25}$$

being g the Landé factor [15, 16], e and m_e the charge and the mass of the electron, respectively, μ_B the Bohr magneton and $\hbar$ the Planck's constant. The Landé factor is equal to 2 when the magnetic momentum originates purely from the electron spin. By using Eq. (1.24), Eq. (1.23) turns into:

$$\boldsymbol{\tau} = \mu_0 \gamma \boldsymbol{\mu} \times \mathbf{H_{eff}} = \frac{d\boldsymbol{\mu}}{dt} \tag{1.26}$$

and, in the micromagnetic framework, it becomes:

$$\frac{d\mathbf{M}}{dt} = -\gamma_0 \mathbf{M} \times \mathbf{H_{eff}} \tag{1.27}$$

where $\gamma_0 = -\mu_0 \gamma$. Eq. (1.27) indicates that the magnetization vector rotates persistently around the direction of the effective field (see Fig. 1.2(a)).

In a real material, dissipative processes result in a damping of the precession (for instance due to scattering processes, interactions with the internal structure of crystals, etc.) and, therefore, the magnetization will tend to align along the effective field. To take into account the damping, Eq. (1.27) has been firstly extended in the explicit form by Landau and Lifshitz [4], by adding a phenomenological damping torque:

$$\frac{d\mathbf{M}}{dt} = -\gamma' \mathbf{M} \times \mathbf{H}_{\text{eff}} - \frac{\gamma' \alpha}{M_S} \mathbf{M} \times \left(\mathbf{M} \times \mathbf{H}_{\text{eff}} \right) \tag{1.28}$$

being α the damping parameter.

Later, Gilbert proposed an implicit expression for the phenomenological damping [17, 18], presenting the so called *Landau-Lifshitz-Gilbert (LLG) equation*:

$$\frac{d\mathbf{M}}{dt} = -\gamma_0 \mathbf{M} \times \mathbf{H}_{\text{eff}} + \frac{\alpha}{M_S} \left(\mathbf{M} \times \frac{d\mathbf{M}}{dt} \right) \tag{1.29}$$

According to both Eq. (1.28) and (1.29), the magnetization will be eventually aligned with the effective field (see Fig. 1.2(b)). However, from the implicit form reported in Eq. (1.29), it is possible to obtain an equation formally equal to Eq. (1.28):

$$\frac{d\mathbf{M}}{dt} = -\frac{\gamma_0}{\left(1+\alpha^2\right)} \mathbf{M} \times \mathbf{H}_{\text{eff}} - \frac{\gamma_0 \alpha}{\left(1+\alpha^2\right) M_S} \mathbf{M} \times \left(\mathbf{M} \times \mathbf{H}_{\text{eff}} \right) \tag{1.30}$$

The last equation is more suitable for numerical analysis, because of the explicit expression of the time derivative of the magnetization.

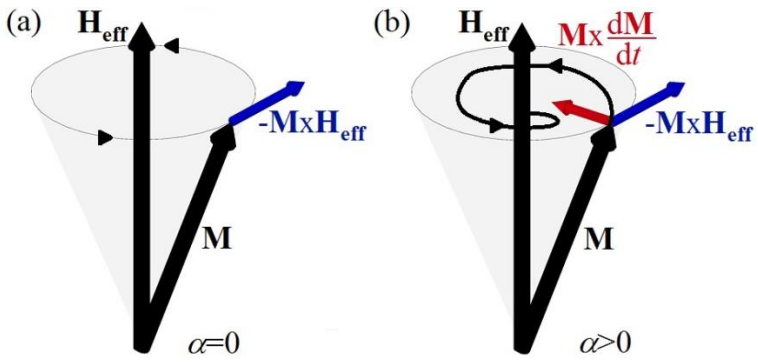

Fig. 1.2: (a) persistent precession of the magnetization **M** around the effective field $\mathbf{H}_{\text{eff}}$ when only the conservative torque acts. (b) Damped precession of the magnetization when the damping torque is considered.

Finally, such equation needs to be completed with a term related to the spin-transfer torque.

1.2.4 Spin-Transfer Torque

In 1996, Slonczewski [19] and Berger [20] independently predicted that a current flowing perpendicularly to the plane in a metallic multilayer could change the magnetization direction in one of the layers. In fact, when a current flows through a ferromagnet, all the electrons spins angular momenta become polarized along the same direction of the magnetization inside the ferromagnet: a spin-polarized current is generated. This spin-polarized current can exert a *spin-transfer torque* (STT) on the magnetization of an adjacent ferromagnet, if it is not parallel to the first one (see Fig. 1.3). The mechanism responsible for the transfer of the spin-angular momentum is the exchange interaction "felt" by the electrons in the ferromagnet, which exerts a torque on the electron spins and, in turn, induces a reaction torque on the magnetization [21]. The possibility to manipulate the magnetization of a ferromagnet by means of a current, and not only of external magnetic fields, has opened new routes for promising applications of spin-transfer torque based devices, such as STT-Magnetic Random Access Memories (STT-MRAMs), spin-torque nano-oscillators (STNOs), nano-magnetic logic devices, etc. [22, 23, 24].

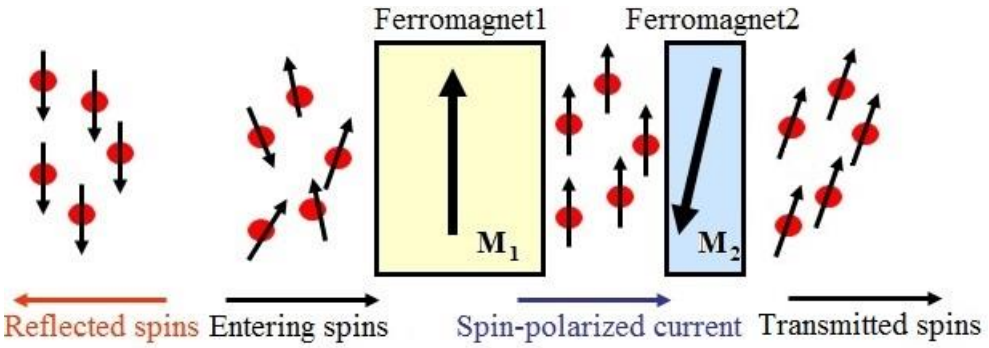

Fig. 1.3: schematic representation of the creation of the spin-polarized current. Part of the entering spins in the ferromagnet1 are polarized in the same direction of $\mathbf{M_1}$, generating the spin-polarized current, which will transfer a spin-torque onto the magnetization $\mathbf{M_2}$ of the adjacent ferromagnet2. Part of the entering spins is reflected with a polarization opposite to $\mathbf{M_1}$.

Indeed, two types of STT can be considered: one acts when the current flows perpendicularly to the plane of a multilayer [19], and another one is exerted when the current flow is in-plane (IP) [20]. Basically, these torques arise in two different devices: the former in OOP devices, the latter in IP ones.

1.2.5 STT in OOP devices

Typical OOP devices are multilayered structures, made by two ferromagnets separated by a non-magnetic material. Usually, one of the two ferromagnet is thicker, in order to keep fixed its magnetization, and it is called *pinned* or *fixed or reference layer* or *polarizer* as well. The other ferromagnet is thinner to allow changes of its magnetization and it is called *free layer* [21]. The chemical nature of the spacer leads to distinguish two types of devices: if the spacer is an electrical conductor, the multilayer is called *spin-valve*; on the other hand, the presence of an electrical insulator spacer characterizes a *magnetic tunnel junction* (MTJ). When the electrical current density $\mathbf{j}_{\mathbf{FE\text{-}oop}}$ flows perpendicularly to the device plane, it is polarized by the magnetization $\mathbf{m}_{\mathbf{p}}$ of the pinned layer and, subsequently it will manipulate the magnetization $\mathbf{m}_{\mathbf{f}}$ of the free layer, via the STT $\boldsymbol{\tau}_{\mathbf{oop}}$ (see Fig. 1.4(a)), which can be modeled as an additional contribution to the LLG equation, as derived by Slonczewski [19]:

$$\boldsymbol{\tau}_{\mathbf{OOP}} = \frac{g\mu_B \mathbf{j}_{\mathbf{FE\text{-}oop}}}{\gamma_0 e M_S^2 t}\varepsilon(\mathbf{m}_{\mathbf{f}}, \mathbf{m}_{\mathbf{p}})\left[\mathbf{m}_{\mathbf{f}} \times \left(\mathbf{m}_{\mathbf{f}} \times \mathbf{m}_{\mathbf{p}}\right)\right] \qquad (1.31)$$

being t the thickness of the free layer and $\varepsilon(\mathbf{m}_{\mathbf{f}}, \mathbf{m}_{\mathbf{p}})$ the polarization function, whose expression depends on the relative orientation between the pinned and free layer magnetization, the category of the device (i.e. spin valves, MTJs), thicknesses and ferromagnetic materials under investigation. In particular, for spin-valves the following $\varepsilon(\mathbf{m}_{\mathbf{f}}, \mathbf{m}_{\mathbf{p}})$ expression is usually used [19]:

$$\varepsilon_{SV}(\mathbf{m_f},\mathbf{m_p}) = \left(-4 + (1+\eta)^3 \frac{\left[3+(\mathbf{m_f}\cdot\mathbf{m_p})\right]}{4\eta^{3/2}} \right)^{-1} \tag{1.32}$$

where η is the spin polarization factor related to the magnetic material. In the case of MTJs, the expression becomes [25]:

$$\varepsilon_{MTJ}(\mathbf{m_f},\mathbf{m_p}) = \frac{0.5\eta}{\left[1+\eta^2(\mathbf{m_f}\cdot\mathbf{m_p})\right]} \tag{1.33}$$

It is important to notice now that the Slonczewski torque acts as an anti-damping torque (or also "negative" damping) [26]. In fact, by comparing the damping torque in Eq. (1.28) and (1.30) with the STT expression in Eq. (1.31), it is possible to observe that they have a similar vector structure. Therefore, for a proper direction of the electrical current (more in detail, for positive current, which conventionally means electrons flowing from the free layer to the pinned layer), the two torques are opposite, implying that, while the damping torque tries to align $\mathbf{m_f}$ with $\mathbf{m_p}$, the STT tries to avoid such alignment, pushing $\mathbf{m_f}$ away from $\mathbf{m_p}$ (see Fig. 1.4(b)). The balance between these two torques is necessary to generate persistent oscillations of the magnetization in dissipative media [23, 26].

The dimensionless *Landau-Lifshitz-Gilbert-Slonczewski (LLGS) equation* for a spin valve finally reads:

$$\begin{aligned} \frac{d\mathbf{m_f}}{d\tau} &= -(\mathbf{m_f}\times\mathbf{h_{eff}}) + \alpha\left(\mathbf{m_f}\times\frac{d\mathbf{m_f}}{d\tau}\right) + \\ &+ \frac{g\mu_B \mathbf{j_{FE\text{-}oop}}}{\gamma_0 e M_S^2 t}\varepsilon_{SV}(\mathbf{m_f},\mathbf{m_p})\left[\mathbf{m_f}\times(\mathbf{m_f}\times\mathbf{m_p})\right] \end{aligned} \tag{1.34}$$

where the dimensionless time step $d\tau = \gamma_0 M_S dt$ has been introduced. Similarly, the LLGS for an MTJ is obtained:

$$\left(1+\alpha^2\right)\frac{d\mathbf{m_f}}{d\tau} = -\left(\mathbf{m_f}\times\mathbf{h_{eff}}\right) - \alpha\left[\mathbf{m_f}\times\left(\mathbf{m_f}\times\mathbf{h_{eff}}\right)\right] - \\ -\frac{g\mu_B\mathbf{j_{FE\text{-}oop}}}{\gamma_0 e M_S^2 t}\varepsilon_{MTJ}(\mathbf{m_f},\mathbf{m_p})\left[\mathbf{m_f}\times\left(\mathbf{m_f}\times\mathbf{m_p}\right) - q(V)\left(\mathbf{m_f}\times\mathbf{m_p}\right)\right] \quad (1.35)$$

where, the main difference with Eq. (1.34) is the presence of an additional component of the STT term, namely the "field-like torque" or "out-of-plane" torque $q(V)\left(\mathbf{m_f}\times\mathbf{m_p}\right)$, which depends on the voltage applied to the MTJ leads [27].

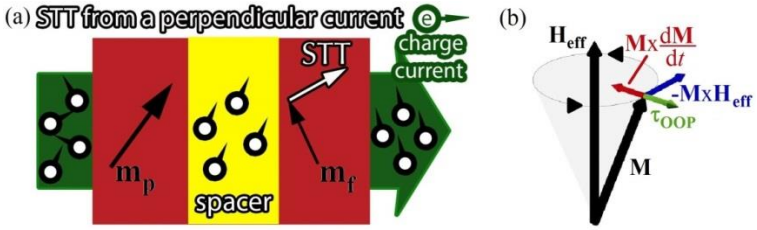

Fig. 1.4: (a) schematic illustration of the spin-transfer torque exerted on the free layer magnetization in an OOP device. (b) representation of all the torques acting on the magnetization.

1.2.6 STT in IP devices

An IP device can be envisaged as a ferromagnetic strip with the length much larger than its width, containing magnetic regions with different internal magnetization (domains) separated by DWs. A current density $\mathbf{j_{FE\text{-}ip}}$, flowing through the strip, is naturally polarized and can induce a translational motion of DWs. More specifically, when an electron flows in a ferromagnetic wire containing a single DW (see Fig. 1.5), the direction of its spin will adiabatically change, meaning that the electron spin will be almost parallel to the local magnetization. Such change in the spin direction gives rise to a STT which shifts the DW along the strip length. The expression of the *adiabatic* STT $\boldsymbol{\tau}_{\mathbf{IP}}^{a}$ was formulated by Berger [20] and reads:

$$\boldsymbol{\tau}_{\mathbf{IP}}^{a} = \frac{\mu_B P}{\gamma_0 e M_S^2}\left(\mathbf{j}_{\mathbf{FE\text{-}ip}} \cdot \nabla\right)\mathbf{m} \tag{1.36}$$

being P the spin polarization factor, which represents the amount of spins polarized by the local magnetization.

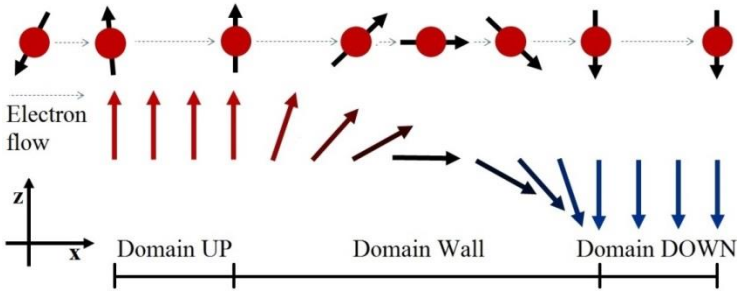

Fig. 1.5: schematic representation of two domains (UP and DOWN) separated by a domain wall. A non-polarized electron flowing through this magnetization configuration will change the direction of its spin adiabatically, namely it will follow the local magnetization orientation.

Later, a second STT was phenomenologically added in order to explain unexpected early stage experimental results. It was called *non-adiabatic* STT and its expression is:

$$\boldsymbol{\tau}_{\mathbf{IP}}^{na} = -\frac{\mu_B P}{\gamma_0 e M_S^2}\beta\left(\mathbf{j}_{\mathbf{FE\text{-}ip}} \cdot \nabla\right)\mathbf{m} \tag{1.37}$$

where β is the non-adiabatic parameter. A complete description and physical origin of the two mentioned torques can be found in [28].

By considering the adiabatic and non-adiabatic STT, the dimensionless LLG equation for IP devices is:

$$\begin{aligned}\frac{d\mathbf{m}}{d\tau} &= -\left(\mathbf{m}\times\mathbf{h}_{\mathbf{eff}}\right) + \alpha\left(\mathbf{m}\times\frac{d\mathbf{m}}{d\tau}\right) + \\ &+ \frac{\mu_B P}{\gamma_0 e M_S^2}\left(\mathbf{j}_{\mathbf{FE\text{-}ip}} \cdot \nabla\right)\mathbf{m} - \frac{\mu_B P}{\gamma_0 e M_S^2}\beta\left(\mathbf{j}_{\mathbf{FE\text{-}ip}} \cdot \nabla\right)\mathbf{m}\end{aligned} \tag{1.38}$$

1.2.7 Voltage controlled magnetocrystalline anisotropy (VCMA)

The application of an electric field can induce variations of the magnetic anisotropy of a ferromagnet, and, hence of its magnetization [29, 30]. The ferromagnet has to be ultrathin for at least two reasons: (i) its

perpendicular anisotropy has to derive from interfacial effects (see subparagraph 2.1.4) [31]; (ii) the electric field can only penetrate few monolayers of the ferromagnet. For these reasons, the VCMA has not been observed in MTJs with relatively thick free layers (>3 nm). One possible origin of this phenomenon is that the electric field influences the electron filling of the ferromagnetic layer, which, consequently, affects the perpendicular anisotropy [32].

In MTJs composed of an iron rich CoFeB and a MgO spacer, the variation of the perpendicular anisotropy field $\Delta H_{k\perp}$ with the applied voltage V_{app} has been measured and reported in Fig. 1.6, where $\Delta H_{k\perp} = H_{k\perp}(V_{app}) - H_{k\perp}(0)$, being $H_k(V_{app})$ and $H_k(0)$ the perpendicular anisotropy field values with and without the applied voltage, respectively. The relation is linear with a slope of 0.6 kOe/V [29]. Therefore, micromagnetically, the VCMA is implemented as a linear change of the perpendicular anisotropy effective field with respect to the applied voltage.

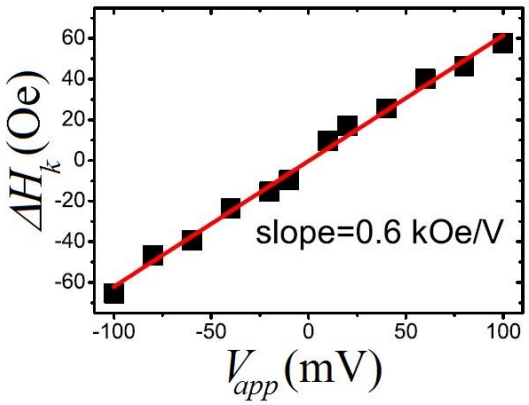

Fig. 1.6: variation of the effective perpendicular anisotropy field when a voltage is applied in CoFeB-MgO MTJs [29].

1.3 Spin-orbit interactions

In the previous paragraphs, it has been seen how both external magnetic field and the STT, as well as the VCMA, can modify the magnetic state of a ferromagnetic material.

Very recently, an additional way to control the magnetization of a ferromagnet has been demonstrated [33, 34, 35, 36, 37], owed to the coupling between the spin angular momentum of an electron and the orbital one in non-magnetic materials (it can be also observed in ferromagnetic material). Such demonstration has opened a novel direction in Spintronics, namely the so-called *Spin-Orbitronics*.

To easily understand the fundament of the spin-orbit coupling (SOC), it is possible to write an approximated expression of its Hamiltonian H_{SO}:

$$H_{SO} \approx \lambda \mathbf{L} \cdot \boldsymbol{\mu} \tag{1.39}$$

where λ is a parameter that depends on the electrical potential V "seen" by the electron. In particular, in the case of central potential approximation, λ is proportional to the atomic number of the non-magnetic material [38]. For this reason, heavy metals (HMs) (Platinum, Tantalum, Iridium, Palladium, Tungsten, etc.) are usually characterized by a large SOC.

The SOC has different forms and origins. In bulk systems, it is possible to distinguish an extrinsic SOC, linked to interactions with impurities, and an intrinsic SOC, related to the band structures of the material [39]. More in detail, the extrinsic SOC can occur in two physical mechanisms: the *skew scattering* and the *side jump*, which both regard the spin-dependent scattering of electrons when they interact with an impurity. In the former case, electrons with spin-UP will be scattered on one side of the impurity with a certain angle, electrons with spin-DOWN will be scattered on the other side (see Fig. 1.7(a)). The latter corresponds to a lateral displacement of electrons towards an impurity (see Fig. 1.7(b)). In both mechanisms, the effect is asymmetrical with respect to the spin state, meaning that spin-UP and spin-DOWN currents are different [38].

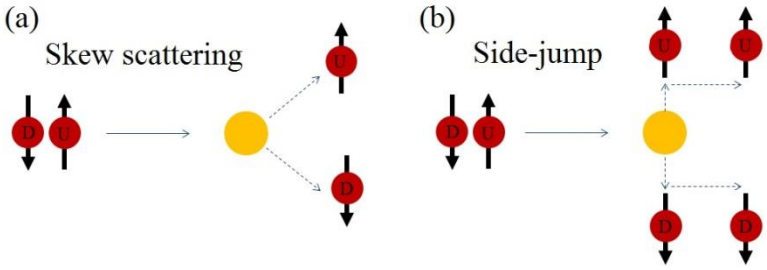

Fig. 1.7: schematic picture of (a) the skew scattering mechanism and (b) the side-jump mechanism. The letters U and D refer to the sign of the spin, respectively spin-UP and spin-DOWN. The yellow circle represents an impurity.

The intrinsic SOC is related to the spin-splitting of the electronic bands occurring in systems lacking the inversion symmetry. This refers to the property of a material to maintain the same characteristics when the position of each particle in the elementary cell is changed from **r** to –**r**. For instance, the body-centered cubic cell represented in Fig. 1.8(a) is characterized by the inversion symmetry. But, it is enough to shift the central atom towards one of the faces of the cube to lose the inversion symmetry property (see Fig. 1.8(b)). The intrinsic SOC is linked to the lack of inversion symmetry of the electrical potential, namely $V(\mathbf{r}) \neq V(-\mathbf{r})$, so that the spin-orbit Hamiltonian H_{SO} is not invariant under the spatial inversion. This so-called *bulk inversion asymmetry* (BIA) of the elementary lattice cell is typical of non-centrosymmetric crystals. However, another kind of inversion symmetry can be identified: the *structural inversion asymmetry* (SIA), which arises in crystals subject to surface strains as well as in heterostructures where a ferromagnetic layer is placed between two asymmetric interfaces [38, 39].

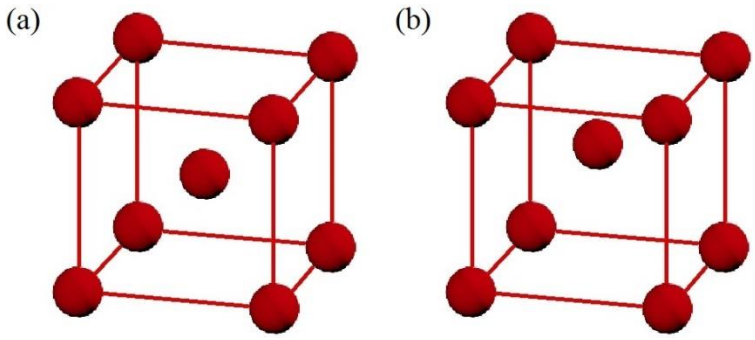

Fig. 1.8: (a) example of crystalline lattice characterized by the inversion symmetry property. (b) Example of crystalline lattice lacking the inversion symmetry.

Both extrinsic and intrinsic SOC are responsible for the generation of spin-orbit related phenomena, such as the anisotropic magnetoresistance (AMR), the spin-Hall effect (SHE), the anomalous Hall effect (AHE), the Rashba effect, and the Dzyaloshinskii-Moriya Interaction (DMI). In the following subparagraphs, the micromagnetic model of the SHE, Rashba effect and DMI will be described.

1.3.1 Spin-Hall Effect

The SHE [33, 40, 41, 42] originates from both extrinsic and intrinsic SOC in by-layered structures where an ultra-thin ferromagnetic material (FM) is deposited on a HM and the electrical current density $\mathbf{j}_{HM}$ flows through the HM (see Fig. 1.9). The spin-dependent electrons

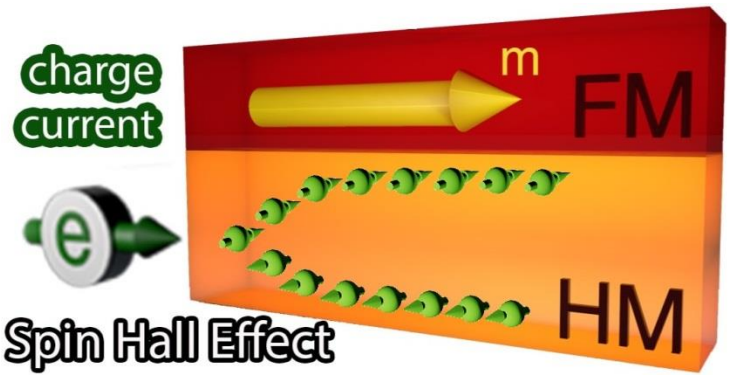

Fig. 1.9: schematic picture of the FM/HM bilayer, where the SHE arises, inducing opposite spin accumulations near the upper and lower surface of the HM.

scattering create a spin accumulation of opposite sign near the upper and lower side of the HM, characterized by a spin-polarization perpendicular to the direction of the electrical current (i.e. if the charge current is along the *x*-axis, the spin-polarization is along the *y*-axis). The spin-accumulation localized at the FM/HM interface allows the spins to diffuse towards the FM. In other words, a vertical spin-current is generated and, consequently, absorbed by the FM, exerting a torque $\boldsymbol{\tau}_{\mathbf{SHE}}$ on its magnetization, which is expressed as:

$$\boldsymbol{\tau}_{\mathbf{SHE}} = -\frac{g\mu_B\theta_{SH}}{2\gamma_0 eM_S^2 t}\mathbf{m}\times\mathbf{m}\left(\hat{z}\times\mathbf{j}_{\mathbf{HM}}\right) \tag{1.40}$$

being θ_{SH} the spin-Hall angle, which represents the amount of charge current j_{HM} converted into spin-current j_s: $j_s = \theta_{SH}\, j_{HM}$. $\hat{z}$ is the unit vector in the OOP direction (the direction of the electrical current is supposed along the *x*-axis). It is possible to notice that the structure of this torque is similar to the Slonczewski torque of Eq. (1.31) [34, 36, 37], with the difference that, instead of considering the direction of the spin-polarization given by the magnetization $\mathbf{m_p}$, here the cross product $\left(\hat{z}\times\mathbf{j}_{\mathbf{HM}}\right)$ indicates the direction of the spin-polarization. Therefore, the SHE torque acts as an anti-damping term [26]. Since the framework where the SHE torque can be observed is an extension of IP devices, it is possible to add $\boldsymbol{\tau}_{\mathbf{SHE}}$ to Eq. (1.38):

$$\begin{aligned}\frac{d\mathbf{m}}{d\tau} = &-\left(\mathbf{m}\times\mathbf{h}_{\mathbf{eff}}\right)+\alpha\left(\mathbf{m}\times\frac{d\mathbf{m}}{d\tau}\right)+\frac{\mu_B P}{\gamma_0 eM_S^2}\left(\mathbf{j}_{\mathbf{FE\text{-}ip}}\cdot\nabla\right)\mathbf{m}- \\ &-\frac{\mu_B P}{\gamma_0 eM_S^2}\beta\left(\mathbf{j}_{\mathbf{FE\text{-}ip}}\cdot\nabla\right)\mathbf{m}-\frac{g\mu_B\theta_{SH}}{2\gamma_0 eM_S^2 t}\mathbf{m}\times\mathbf{m}\left(\hat{z}\times\mathbf{j}_{\mathbf{HM}}\right)\end{aligned} \tag{1.41}$$

In this way, if the electrical current flows completely via the ferromagnet, $\mathbf{j}_{\mathbf{HM}}$ =0 A/cm^2 and only the STT is taken into account. On the contrary, if the electrical current is entirely passed through the HM, $\mathbf{j}_{\mathbf{FE\text{-}ip}}$ =0 A/cm^2 and only the SHE torque acts.

1.3.2 Rashba effect

In the bilayer analyzed in the previous subparagraph, an electric field can build up due to the SIA at the FM/HM interface. If an electrical current density $\mathbf{j}_{\mathbf{FE\text{-}ip}}$ flows through the ferromagnet, the electrons passing near the interface "perceive" that electric field as a magnetic field (Lorentz transformation) [Supplementary Information 34, 43]. This effect is micromagnetically modeled by considering two terms: an effective magnetic field $\mathbf{h}_{\mathbf{R}}$ in the direction transverse to both the electric field and the current density and an anti-damping torque $\boldsymbol{\tau}_{\mathbf{R}}$ [44]:

$$\mathbf{h}_{\mathbf{R}} = \frac{\mu_B \alpha_R P}{\gamma_0 e M_S^2} \mathbf{m} \times \left[\hat{z} \times \mathbf{j}_{\mathbf{FE\text{-}ip}} \right], \tag{1.42}$$

$$\boldsymbol{\tau}_{\mathbf{R}} = \frac{\mu_B \alpha_R P}{\gamma_0 e M_S^2} \beta \mathbf{m} \times \mathbf{m} \times \left(\hat{z} \times \mathbf{j}_{\mathbf{FE\text{-}ip}} \right), \tag{1.43}$$

being α_R the Rashba parameter.

Hence, when an electrical current flows via a FM coupled to a HM (see Fig. 1.10), gives rise to both the STT and the Rashba effect, leading to the following LLG equation:

$$\begin{aligned} \frac{d\mathbf{m}}{d\tau} = &-\left(\mathbf{m} \times \mathbf{h}_{\mathbf{eff}}\right) - \left(\mathbf{m} \times \mathbf{h}_{\mathbf{R}}\right) + \alpha \left(\mathbf{m} \times \frac{d\mathbf{m}}{d\tau} \right) + \frac{\mu_B P}{\gamma_0 e M_S^2} \left(\mathbf{j}_{\mathbf{FE\text{-}ip}} \cdot \nabla \right) \mathbf{m} - \\ &- \frac{\mu_B P}{\gamma_0 e M_S^2} \beta \left(\mathbf{j}_{\mathbf{FE\text{-}ip}} \cdot \nabla \right) \mathbf{m} - \frac{\mu_B \alpha_R P}{\gamma_0 e M_S^2} \beta \mathbf{m} \times \mathbf{m} \times \left(\hat{z} \times \mathbf{j}_{\mathbf{FE\text{-}ip}} \right) \end{aligned} \tag{1.44}$$

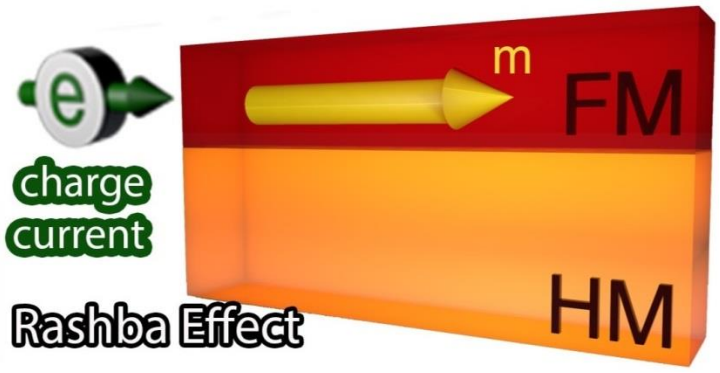

Fig. 1.10: the Rashba effect arises in FM/HM bilayers, when the electrical current flows through the ferromagnet.

1.3.3 Dzyaloshinskii-Moriya Interaction

The DMI is a chiral energetic term, which acts as an antisymmetric exchange contribution [45, 46]. In fact, while the exchange tries to align adjacent spins in parallel, maintaining a uniform magnetization state, the DMI prefers to align them orthogonally, fostering the formation of rotational magnetization textures. The DMI originates from both BIA, in single crystals, and SIA, in multilayered structure at the FM/HM interface. In the first case, a *bulk DMI* arises, whereas, in the second one, an *interfacial DMI* (*i*-DMI) takes place (see Fig. 1.11) [47]. The energy density expressions for the two types of DMI are [48]:

$$\begin{aligned} \varepsilon_{BulkDMI} &= D\mathbf{m}\cdot\nabla\times\mathbf{m} \\ \varepsilon_{InterDMI} &= D\left[m_z\nabla\cdot\mathbf{m}-\left(\mathbf{m}\cdot\nabla\right)m_z\right] \end{aligned} \tag{1.45}$$

being D the parameter taking into account the intensity of the DMI. Indeed, for the expression of $\varepsilon_{InterDMI}$, the ultra-thin film hypothesis has been considered $\left(\frac{\partial\mathbf{m}}{\partial z}=0\right)$.

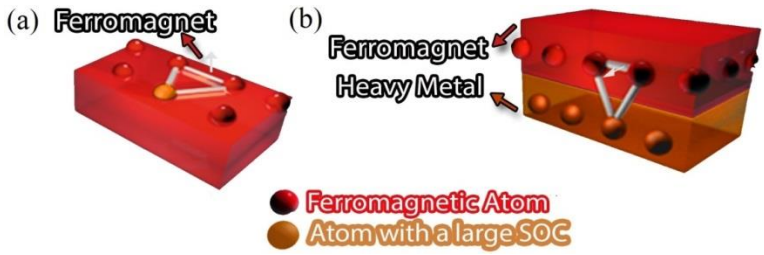

Fig. 1.11: (a) bulk DMI vector originating in a non-centrosymmetric crystal because of the interaction of the ferromagnetic atoms with an impurity with large SOC. (b) Interfacial DMI vector in a FM/HM bilayer.

In the micromagnetic framework, the DMI is considered as an additional term to the effective field, directly derived from the energy densities:

$$\begin{aligned}\mathbf{h}_{BulkDMI} &= -\frac{1}{\mu_0 M_S}\frac{\delta\varepsilon_{BulkDMI}}{\partial\mathbf{m}} = -\frac{2D}{\mu_0 M_s}\nabla\times\mathbf{m} \\ \mathbf{h}_{InterDMI} &= -\frac{1}{\mu_0 M_S}\frac{\delta\varepsilon_{InterDMI}}{\partial\mathbf{m}} = -\frac{2D}{\mu_0 M_S}\left[\left(\nabla\cdot\mathbf{m}\right)\hat{z} - \nabla m_z\right]\end{aligned} \tag{1.46}$$

Besides, the DMI affects the boundary conditions (BC) of the ferromagnet in the following way [48]:

$$\begin{aligned}&\text{Bulk DMI BC: } \frac{d\mathbf{m}}{dn} = \frac{\mathbf{m}\times\mathbf{n}}{\xi} \\ &\text{Interfacial DMI BC: } \frac{d\mathbf{m}}{dn} = \frac{1}{\xi}\left(\hat{z}\times\mathbf{n}\right)\times\mathbf{m}\end{aligned} \tag{1.47}$$

where $\xi = \frac{2A}{D}$ is a characteristic length in presence of the DMI.

As it will be explained in the next paragraph, the DMI is one of the key ingredients to stabilize magnetic skyrmions.

1.3.4 Three terminal MTJ device

In 2012, Liu *et al.* [49] introduced a new spintronic device where an MTJ is deposited on an extended HM underlayer (see Fig. 1.12). In this framework, the magnetization of the MTJ free layer can be manipulated by the STT from a perpendicular current flowing through the MTJ and by the spin-orbit torque (SOT) from the SHE [50], due to an IP electric current injected into the HM, as well as by other spin-orbit phenomena, such as the DMI. In other words, the so called “three terminal device” combines Spintronics and Spin-Orbitronics.

If the three terminal device is used as storage, the writing current is injected via the first terminal into the HM. In this way, high currents can flow without damaging the insulator barrier of the MTJ. On the other hand, the small reading current can directly be injected via the second terminal into the MTJ.

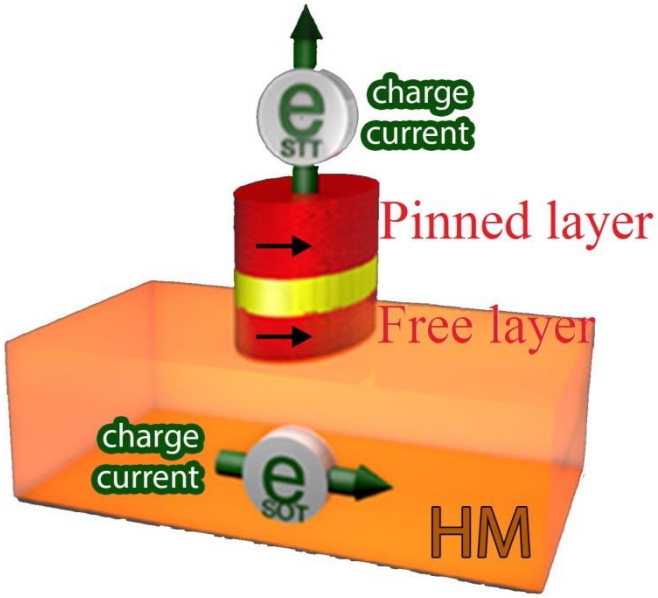

Fig. 1.12: schematic representation of a three terminal device, where an MTJ is coupled through its free layer to a HM underlayer.

The dynamics of the free layer magnetization can be studied by means of the following equation, which is an extension of Eq. (1.35):

$$\begin{aligned}(1+\alpha^2)\frac{d\mathbf{m_f}}{d\tau} &= -\left(\mathbf{m_f}\times\mathbf{h_{eff}}\right)-\alpha\left[\mathbf{m_f}\times\left(\mathbf{m_f}\times\mathbf{h_{eff}}\right)\right] \\ &-\frac{g\mu_B\theta_{SH}}{2\gamma_0 eM_S^2 t}\left[\mathbf{m_f}\times\mathbf{m_f}\left(\hat{z}\times\mathbf{j_{HM}}\right)\right]+\frac{g\mu_B\theta_{SH}}{2\gamma_0 eM_S^2 t}\mathbf{m_f}\times\left(\hat{z}\times\mathbf{j_{HM}}\right) \\ &-\frac{g\mu_B\mathbf{j_{FE\text{-}oop}}}{\gamma_0 eM_S^2 t}\varepsilon_{MTJ}(\mathbf{m_f},\mathbf{m_p})\left[\mathbf{m_f}\times\left(\mathbf{m_f}\times\mathbf{m_p}\right)-q(V)\left(\mathbf{m_f}\times\mathbf{m_p}\right)\right]\end{aligned} \tag{1.48}$$

1.4 Magnetic skyrmions

Skyrmions are a non-uniform configuration of the magnetization which are attracting a growing interest from both fundamental and technological point of view. Together with DWs, vortexes, bubbles, a skyrmion can be considered a magnetic soliton and, in certain scenarios, can behave like a rigid object. The term skyrmion derives from the field of Particle Physics and was coined by the physicist Tony Skyrme [51] to identify topologically stable field configuration related to mesons. Recently,

that term has been borrowed in Spintronics to indicate topologically protected particle-like magnetization patterns.

1.4.1 Topology and skyrmion number

The adjective "topologically protected" comes from a classification of magnetic solitons according to a parameter called *skyrmion number S*, defined as [52, 53, 54]:

$$S = \frac{1}{4\pi} \int \mathbf{m} \cdot \left(\partial_x \mathbf{m} \times \partial_y \mathbf{m} \right) dxdy \tag{1.49}$$

In general, an integer skyrmion number implies a topological protection of the soliton, meaning that it cannot be continuously deformed into the uniform ferromagnetic state without causing a singularity [54]. In other words, configurations with different skyrmion numbers cannot be continuously converted into each other because of the presence of a Bloch point or line. The understanding of the meaning of the skyrmion number can be related to the total variation of the magnetization angle when moving counterclockwise around a circle, divided by 2π [54]. For example, let's consider the spin configurations in Fig. 1.13. In the first case (Fig. 1.13(a) left panel), all the spins point in the same direction, hence there is no variation of the magnetization angle and the skyrmion number is zero. The same result is obtained for the configuration of Fig. 1.13(a) right panel. In fact, if we start to move from the circled spin, after a quarter of turn, the magnetization angle covers $\pi/2$ in a counterclockwise sense. In the next quarter of turn, the magnetization covers again an angle of $\pi/2$, but in the clockwise sense, resulting in a zero angle variation with the respect to the starting spin. The same occurs for the other subsequent half turn. Therefore, at end, there is no change in the magnetization angle and the skyrmion number is again zero. In the case of Fig. 1.13(b), a 2π continuous rotation of the magnetization angle is observed in a complete turn, leading to a skyrmion number equal to 1. In the last case of Fig. 1.13(c), the

magnetization covers continuously an angle of 4π in a turn, being characterized by a skyrmion number equal to 2.

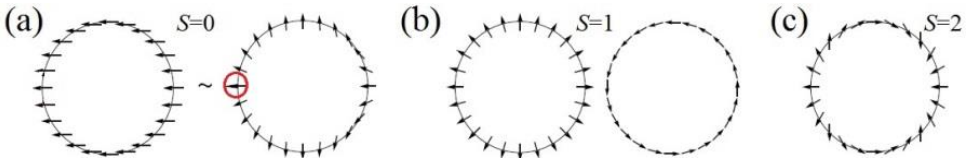

Fig. 1.13: magnetization configurations with skyrmion number *S* equal to (a) zero, (b) one, and (c) two [54].

In this concern, DWs have a zero skyrmion number [55], vortexes have $S = \pm 1/2$ (the sign depends on the polarity of the vortex) [56], and bubbles can be characterized by different *S*. Bubbles with $S = \pm 1$ are called either *Bubble skyrmions*, if stabilized by a competition between exchange and magnetostatic field and without DMI, or *Skyrmions* in presence of DMI. An example of topological soliton with $S = 2$ is the quadripole [57].

Magnetic skyrmions consist of two perpendicular and opposite magnetization domains separated by a circular IP DW. In order to nucleate a skyrmion, two main features are necessary: the use of ferromagnetic materials with the magnetization pointing in the OOP direction (use of large external field or perpendicular materials), and the presence of the DMI. In particular, since two types of DMI exist (as explained in the subparagraph 1.3.3), two types of skyrmions can be stabilized. In the case of bulk DMI, *Bloch skyrmions* are stabilized, which have a vortex like configuration of the domain wall spins (see Fig. 1.14(a)); when the *i*-DMI originates, *Néel skyrmions* are obtained, characterized by a radial distribution of the domain wall spins (see Fig. 1.14(b)) [47]. The chirality of both skyrmions depends on the sign of the DMI parameter. It is worthy to underline that skyrmions have a double protection linked to, firstly, the free energy minimization and, secondly, to the topology, which confers to them a strong stability.

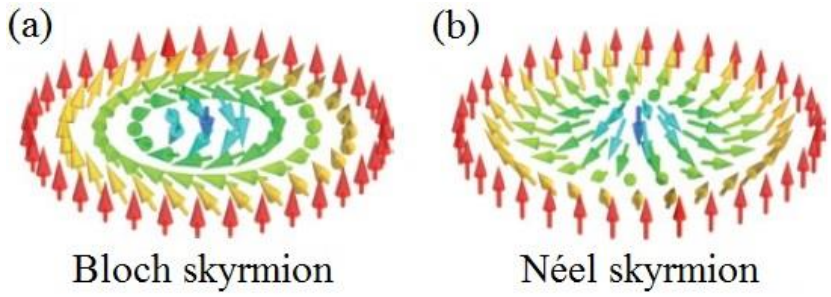

Fig. 1.14: magnetization distribution of a (a) Bloch skyrmion and (b) Néel skyrmion [47].

1.4.2 Observations of skyrmions

Skyrmions have been observed in the form of skyrmions lattice, isolated skyrmions (skyrmions not organized in a lattice) and single skyrmion. After the prediction of the existence of skyrmions in 2006 by Rossler *et al.* [58], the first indirect experimental observation of skyrmions concerned a skyrmions phase in the field-temperature phase diagram of a MnSi compound, characterized by a bulk DMI [59]. In 2010, the first real observation of Bloch skyrmions lattice and isolated skyrmions was achieved by means of Lorentz Transmission Electron Microscopy in FeCoSi alloy [60]. A year later, a Néel skyrmions lattice was observed via Spin-Polarized-Scanning Transmission Microscopy in a monolayer of iron grown on a iridium underlayer and at zero external field [61]. However, all these studies were carried out near the temperature of 0 K. In 2012, Huang *et al.* [62] proved that in a thin FeGe compound, a Bloch skyrmions lattice could be obtained close to room temperature and at zero external field. Afterwards, several numerical studies were performed in order to better understand static and dynamical behaviors of skyrmions. Iwasaki *et al.* [63] predicted the motion of skyrmions lattice by the injection of an IP electrical current, gathering the so called universal current-velocity relation. Later, the same group demonstrated the motion of a single skyrmion in a confined MnSi strip, proposing a way to nucleate single skyrmions by means of a notch made in the ferromagnetic layer [64]. At the same time, Fert *et al.* proposed a technological use of skyrmions in racetrack memories, as

alternative to DWs [47]. A milestone is the work by Sampaio *et al.* [65], where, via micromagnetic simulations, they proved that a single skyrmion can be nucleated by a perpendicular polarized current and it can be moved by either the STT or the SHE. The latter mechanism drives the Néel skyrmion in the same direction of the current and it is energetically more efficient than the STT, as the same skyrmion velocities can be achieved by applying lower currents (see subparagraph 2.4.1).

Further numerical predictions have involved skyrmions as basis for logic gates [66] and transistors [67] and as source of microwave signals in point-contact nano-oscillators, linked to either a mode of the skyrmion core called “breathing mode” [68, 69, 70] (see paragraph 4.1) or to the rotation of the skyrmion around the nano-contact [71].

Recently, the hardest challenge regarding the stabilization of single skyrmions at room temperature seems to have been overcome, both in circular nano-dots [72] and in multilayered nanowire [73], encouraging the research on skyrmions for new device concepts.

2. MAGNETIC MEMORIES: STT-MRAM AND RACETRACK

The second chapter concerns the study of spintronic devices such as magnetic memories. Paragraph 2.1 deals with the use of MTJs as STT-MRAM and it focuses on the achievements on tunnel magnetoresistance, reduction of the critical current to write the information bit, and thermal stability, giving also a brief description of the *state of the art* of STT-MRAMs. Paragraph 2.2 shows the results obtained about STT-MRAMs. In the paragraph 2.3, a brief review on racetrack memories is presented, followed by the outcomes achieved on skyrmion racetrack memories, discussed in paragraph 2.4.

2.1 MTJ based STT-MRAM

STT-MRAM is a magnetic non-volatile solid state memory which is a promising candidate to be used as "universal memory" (supporting both operations and storage in computing architecture) in the next generation products [22]. The fundamental component of STT-MRAMs is the MTJ (see subparagraph 1.2.5), having, nowadays, lateral dimensions of about 20 nm [74]. The functionality of a STT-MRAM is made possible thanks to two

basic phenomena: the already discussed STT (see subparagraph 1.2.4), involved in the writing process of information bits, and the Tunnel MagnetoResistance (TMR) [75], necessary for the reading process. The information bit is stored in the MTJ free layer. More in details, it can have two magnetization states: one is parallel to the pinned layer magnetization, and the other one is antiparallel. Because of the TMR, these two magnetic states correspond to two electric resistance states of the device, low and high respectively. Therefore, it is possible to associate two information bits "0" and "1" to the two magnetic states of the MTJ [22]. In order to write the bits, it is necessary to switch the free layer magnetization, via the STT mechanism, from the P to the AP configuration and vice versa.

The switching dynamics are micromagnetically studied by solving the LLGS equation in Eq. (1.35).

In the following subparagraphs, the key points of STT-MRAMs will be discussed, in terms of TMR, writing and reading processes, and thermal stability.

2.1.1 Tunnel MagnetoResistance

The TMR is exhibited by MTJs because of the presence of the insulator spacer placed between the two ferromagnets and concerns the spin-dependent tunneling through the insulator barrier. The phenomenon can be understood by considering the example shown in Fig. 2.1. The electrons with a certain spin orientation can tunnel from the pinned layer to the free layer (assuming that spin is conserved during tunneling) only if there are empty states available in the free layer, corresponding to such spin orientation. In particular, the majority electrons spins orientation is related to the magnetization direction of each ferromagnets. In Fig. 2.1(a), the magnetization state is parallel along the positive OOP direction. Therefore, the majority electrons are characterized by spin-UP and can fill the majority states in the free layer, while minority electrons with spin-DOWN will fill the minority states. This will result in a low electric resistance R_P of the

junction. In the case of AP magnetization state (see Fig. 2.1(b)), the majority and minority states in the two ferromagnets are reversed, namely the pinned layer has majority electrons with spin-UP, whereas the free layer has majority electrons with spin-DOWN. Hence, the majority spins from the pinned layer fill minority states in the free layer and vice versa, resulting in a low current flow and, therefore, in a high electric resistance R_{AP} of the device. It is possible to define the *TMR ratio* as:

$$TMR = \frac{R_{AP} - R_P}{R_P} \tag{2.1}$$

The TMR effect has been first observed in 1975 by Julliere, who detected a TMR ratio of 14% at 4.2 K [75].

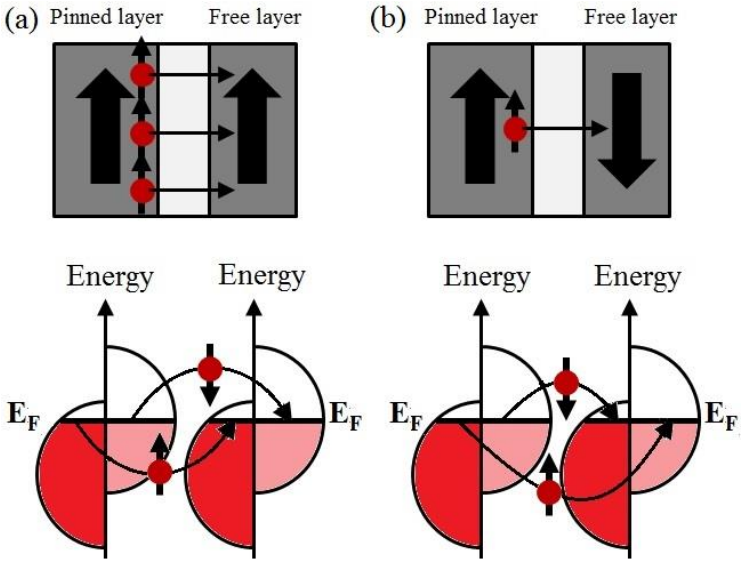

Fig. 2.1: schematic illustration of the TMR phenomenon in MTJs, where in (a) the magnetization state is parallel, allowing many spin-UP electrons to tunnel from the pinned layer to the free layer, in (b) the magnetization state is AP and just few spin-UP electrons can tunnel, leading to a high resistance of the MTJ. In the bottom panels, the density of states at Fermi level are represented, corresponding to the two ferromagnets in the two magnetization configurations.

In 1995 Miyazaki *et al.* [76] and Moodera *et al.* [77] made MTJs with amorphous AlO barriers, obtaining TMR of 18% at room temperature, which has been increased later to about 70% by optimizing the ferromagnetic materials and the conditions for fabricating oxides [78]. In

2004, TMR ratios of about 200% were obtained at room temperature with a crystalline MgO barrier [79]. Nowadays, MgO based MTJs can exhibit a TMR larger than 500% [80]. High TMR values are suitable for memory applications because they improve the detection of the two magnetization states.

2.1.2 Writing and reading process

STT-MRAMs differ significantly from standard MRAMs, which use a magnetic field with a toggle procedure to switch the free layer magnetization [81, 82]. The main disadvantages of field switched MRAM are the more complex cell architecture as well as high writing current (order of mA) to generate the magnetic fields and poor scalability beyond 65 nm [83]. STT writing technology overcomes these drawbacks with lower switching current (order of μA), simpler cell architecture, thus, reducing the manufacturing cost, and more importantly, very high scalability to future technology nodes [83, 84, 85]. A major challenge for the STT writing mode is the reduction of the dc critical current density J_C (writing current) which switches the free layer magnetization from the P and to the AP state and vice versa, while maintaining high thermal stability necessary for long-term data endurance [31]. Minimal critical current densities are required for at least three main reasons. Firstly, for reducing the energy consumption of the memory cell. Secondly, smaller voltages across the MTJ decrease the probability of tunneling barrier degradation and breakdown, ensuring write endurance of the device. Thirdly, for dropping the size of the selection transistor connected in series with the MTJ (see Fig. 2.2) to achieve the highest possible memory density.

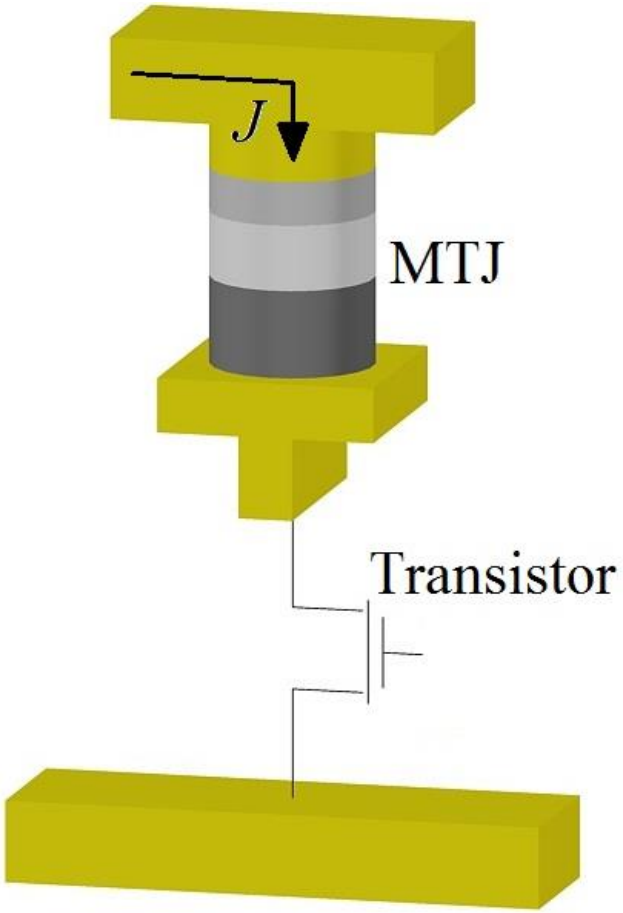

Fig. 2.2: schematic representation of a MTJ connected in series with a selection transistor.

Two types of STT-MRAMs exist according to the magnetization orientation of the pinned and free layer: IP memories and OOP ones (see Fig. 2.3). For the IP cell, considering the hypothesis of uniform switching approximation and at zero temperature, the analytical expression for the critical current density J_C^{ip} is given by [85, 86]:

$$J_C^{ip} = \frac{2\alpha e}{\varepsilon_{MTJ}\hbar} M_S t\left(H_{ext} + H_k + 2\pi M_S - H_{k\perp}/2\right) \qquad (2.2)$$

where $2\pi M_S$ is related to the demagnetizing field. For the OOP cell, the analytical formula of the critical current J_C^{oop} reads [85, 86]:

$$J_C^{oop} = \frac{2\alpha e}{\varepsilon_{MTJ}\hbar} M_S t\left(H_{ext} + H_{k\perp} - 2\pi M_S\right) \quad (2.3)$$

being $2\pi M_S$ the demagnetizing field parallel to $H_{k\perp}$, and H_{ext} the perpendicular external field. When the injected current $J>J_C$, the magnetization of the free layer is reversed. Indeed, the critical current density $J_C^{P\to AP}$, inducing the P to the AP state switching, is different from the corresponding $J_C^{AP\to P}$, since the spin polarization function ε_{MTJ} depends on the relative orientation of the pinned and free layer magnetizations [87, 88]. In order to be competitive with the nowadays' used CMOS technology, the STT-MRAMs should exhibit a critical switching current density (SCD) of the order of 10^5 - 10^6 A/cm^2 [31].

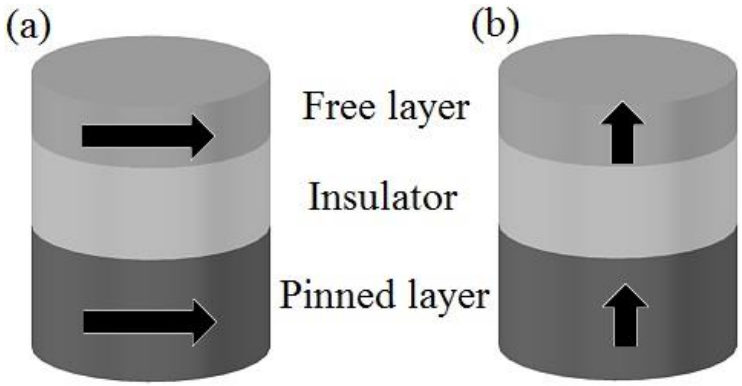

Fig. 2.3: schematic illustration of (a) an IP MTJ and (b) an OOP one.

The reading process occurs via the same transistor, but using a current I smaller than the critical one. Depending on the electric resistance state (R_P or R_{AP}), the resulting output voltage $R_P(R_{AP})\cdot I$ will be low (high), detecting the information bit "0" ("1").

2.1.3 Thermal stability and writing energy

The thermal stability is directly correlated to the non-volatility property of STT-MRAMs, and, consequently to the endurance (or retention time) of the information bit. In other words, it is possible to define a thermal stability factor Δ that indicates the magnetic bit stability against false switching events due to thermal activation. For instance, a thermal stability

factor of 40 means a retention time of about 10 years [89]. In particular, the stability factor for uniform magnetization is expressed by [31, 86, 89]:

$$\Delta = \frac{k_{eff} V}{k_B T} = \frac{M_S H_{Keff} V}{2 k_B T} \tag{2.4}$$

where k_{eff} is the effective anisotropy constant in J/m^3, V is the magnetic volume of the free layer, and H_{Keff} is the effective anisotropy field, which takes into account both the anisotropy and the demagnetizing field. It is important to notice that, if the volume of the free layer is decreased, the effective anisotropy field needs to be increased to keep the same thermal stability factor, for example, by changing the shape of the free layer cross section (aspect ratio, namely length to width ratio) or its thickness. Indeed, it is also possible to vary M_S, by changing the material of the free layer. Moreover, for IP devices the thermal stability factor in mainly related to the shape anisotropy, whereas, for OOP devices, it depends on the perpendicular effective anisotropy field. This leads to an advantage of perpendicular memories on IP ones, as described in the next subparagraph.

The energy E_w necessary to write the bit depends on the current pulse width t_p as [89]:

$$E_w = J_C^2 S^2 R t_p \tag{2.5}$$

being S and R the area of the cross section and the resistance of the MTJ, respectively. Therefore, the write energy can be essentially reduced, by decreasing the resistance (which is limited for practical reasons), and, again, by reducing the critical SCD.

2.1.4 State of the art

STT-MRAMs combine materials development from the hard disk drive industry, with the *know-how* of memory design and manufacturing from the field switched MRAM. The first switching demonstration via the STT mechanism has been reported in IP spin-valves in 1998 [90]. Since then, many efforts have been done from both theoretical and experimental

side, leading, in 2004, to the first STT induced switching in AlO based IP MTJs [91]. In 2005, the switching has been successfully demonstrated in MgO based MTJs with TMR>150% and small SCD [87], and later, in 2006, the first reversal in perpendicular spin-valves has been proved [92]. In 2010, the key milestone work by Ikeda *et al.* [31] has opened the design of OOP MgO based MTJs with perpendicular anisotropy [29, 93]. Specifically, it has been demonstrated that in these kinds of devices, the perpendicular anisotropy is dominated by the interfacial effects between the MgO barrier and the iron-rich CoFeB free layer, due to the electrostatic interaction between the *2d* iron orbital of the ferromagnet and the *2p* oxygen one of the spacer [31]. Perpendicular MTJs based STT-MRAMs have shown reduction of the critical current density (considering an equal thermal stability of IP memories), larger thermal stability thanks to the high anisotropy field, and manufacturability in smaller technology nodes down 30 nm. This last advantage over IP devices is owed to the thermal energy barrier dependence on only the effective perpendicular anisotropy, which avoids the use of elongated cross sections of MTJs (as, instead, happens for IP devices), enabling the fabrication of circular memories [89]. Furthermore, the possibility to manipulate the perpendicular anisotropy by means of the VCMA (see subparagraph 1.2.7), has led, in 2012, to electric field assisted STT-MRAMs characterized by a unipolar switching of the magnetization [29].

Lately, after the promising results about magnetization switching driven by the SHE [34, 37, 94], the research has been also devoted to the design of MRAM based on such spin-orbital interaction [95].

Finally, it is useful to mention some commercialization achievement. In 2005, Sony announced a first 4 kb SpinRAM memory, based on CoFeB-MgO MTJ with high TMR of 160% [96]. In the same year, Renesas, the joint branch from Hitachi and Mitsubishi from Japan, started the production of STT-MRAM chips in a 65 nm process in cooperation with the american company Grandis. In 2007, a Hitachi and Tohuku University joint

collaboration announced a 2 Mbit STT-MRAM [97], and in 2008, IBM provided a preview of 64Mbit memory. In 2009, Samsung and Hynix started to work on 30 nm STT-MRAM. In 2012, Toshiba developed a prototype STT-MRAM that, according to Toshiba, achieves the world's lowest power consumption ever reported [74]. In 2013, Buffalo Memory launched the first product on the market: a solid state drive SATA III (the S6C series) that uses Everspin's STT-MRAM [98] as cache memory.

2.1.5 Comparison with other technologies

In the memory hierarchy, the information is temporally stored in static random access memories (SRAMs) as cache memory, and in dynamic random access memories (DRAMs) as the principal working memory, and then, permanently stored in Flash or hard drives, used as non-volatile memories for long-term retention. In particular, SRAM is the fastest of the three (operating in the GHz range), needs little dynamic power (about 100 fJ per switch), has unlimited endurance, and can be incorporated directly on the logic chip. However, SRAM is volatile, has a very low density (resulting in a higher cost per bit) and the standby power consumption increases too much as the transistor dimensions are scaled down. DRAM has a higher density compared with SRAM, but it is also volatile and needs a periodic refresh, which results in power consumption for maintaining the memory state. The NOR flash memories have the highest density among the three, and are non-volatile. However, they have very slow write speed and very limited endurance. They also use high power for writing data and high internal voltages are needed for their operation. These factors provide strong motivation to develop a technology that utilizes new physical principles and is scalable to smaller technology nodes. A number of such technologies have been explored in the past, but only few of them were proven to match these high demands, and STT-MRAMs are among those few. They might have the density of DRAM, the speed of SRAM and the non-volatility of flash, as well as unlimited endurance and low power consumption. While it

is challenging to meet all these requirements at the same time (DRAM technology node is below 30 nm, flash density is up to 3 bits per cell, write operation for SRAM takes less than 1 ns), STT-MRAMs have a large potential market because it can combine the capability of existing memory technologies with new functionality (for example, the density of DRAM combined with the non-volatility of flash) and provide greater scalability to future technology nodes [89]. A comparison of the main characteristics of the storage technologies is reported in Table 2.1.

Feature	**SRAM**	**DRAM**	**FLASH**	**MRAM**	**STT-MRAM**
Non-volatile	No	No	Yes	Yes	Yes
Cell size (F^2)	50-120	6-8	4-8	16-40	6-20
Node (nm)	300	20	30	65-200	30-130
Density	Low	High	High	High	High
Read Speed	1 ns	10 ns	25 μs	2-20 ns	1-10 ns
Write speed	1 ns	10 ns	200 μs	2-20 ns	1-10 ns
Dynamic Power	Low	Medium	Very high	High	Medium
Leakage Power	High	Medium	None	None	None
Scalability	Yes	Yes	Yes	Yes	Yes
Data retention	ms	ms	10 years	10 years	10 years
Write endurance (cycles)	10^{16}	10^{16}	10^{5}	10^{15}	10^{15}
Cost ($/GB)	500-1000	1-10	0.1-1	100-1000	100-1000

Table 2.1: comparison of storage technologies [99].

2.2 Results on STT-MRAMs

In the next two subparagraphs, the results achieved on STT-MRAMs based on a uniform state of the free layer magnetization will be described.

2.2.1 Switching Properties in Magnetic Tunnel Junctions With Interfacial Perpendicular Anisotropy: Micromagnetic Study

As mentioned in the subparagraph 2.1.4, in structures with a CoFeB free layer and an MgO spacer, it is possible to exploit the IPA to achieve suitable switching and dynamical properties. This interaction is micromagnetically modeled as a perpendicular anisotropy field contribution $\mathbf{h_{IPA}}$ (see subparagraph 1.1.2).

Experimental data in Fig. 1 of [100] show M_S and IPA for a $Co_{20}Fe_{60}B_{20}$ free layer as function of its thickness, highlighting an inverse proportionality of the IPA. In the same paper, IPA is quantified by means of the product of k_u and the free layer thickness.

Here [101], we numerically study the dependence of the SCD on the IPA and on the M_S, either with an IP or with an OOP magnetization, simulating a fast switching (20 ns) and an ultra-fast switching (10 and 5 ns). Moreover, we analyze the effect of the thermal contribution at room temperature, showing the critical current density, which allows to reach a reliable magnetization reversal, as a function of the IPA and of M_S. We further provide a complete scheme of the power dissipation. With respect to the experimental works, where the IPA contribution is changed through the free layer thickness or composition, our numerical analysis permits to determine directly the IPA value for the design of MRAMs.

We reproduce the same experimental framework of [100]. The object under investigation is an MTJ nanopillar with an elliptical cross section of 170x60 nm^2, as displayed in Fig. 2.4. The sample structure stack includesPtMn(15)/$Co_{70}Fe_{30}$(2.3)/Ru(0.85)/$Co_{40}Fe_{40}B_{20}$(2.4)/MgO(0.8)/$Co_{20}Fe_{60}B_{20}$(1.4) (thicknesses in nm). No external magnetic field is applied. We

introduce a Cartesian coordinate system with the *x*-axis oriented along the larger dimension of the ellipse and the *z*-axis along the layers thickness. We consider the critical current to switch the magnetization from the AP state to the P configuration and that the switching phenomenon is achieved when the normalized *x*-component of the magnetization reaches ± 0.8.

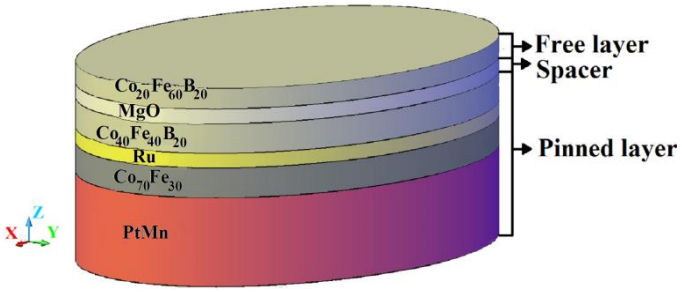

Fig. 2.4: schematic representation of the studied MTJ.

We perform micromagnetic simulations based on the numerical solution of the LLGS equation in Eq. (1.35). We set α=0.02. In order to consider an IP magnetization, we refer to the curves reported in [100] and we extract the free layer thickness t=1.4 nm, where the bulk anisotropy is null, and the corresponding M_S=8x10^5 A/m. After setting that value of t, we study the IP switching properties (within a switching time close to 20 ns and to 10 ns) by changing the free layer composition (M_S and IPA). In practice, those parameters can be varied by changing the percentage of Co, Fe, and B. Particularly, it has been experimentally observed that the coercivity field (proportional to the term $H_{k\perp} - 2\pi M_S$) changes with the free layer chemical composition [102] and, therefore, M_S and IPA can be tuned in this way as well. Similarly, we analyze the OOP ultra-fast switching with a switching time equal to 5 ns and 10 ns.

We also include the thermal effect at T=350 K (see subparagraph 1.2.2) for the specific case of IP fast magnetization reversal (<20ns).

Fig. 2.5 shows the SCD as a function of the IPA and parameterized with three different values of M_S: 8x10^5 A/m, 10x10^5 A/m, and 12x10^{5}A/m, as obtained by means of our numerical simulations.

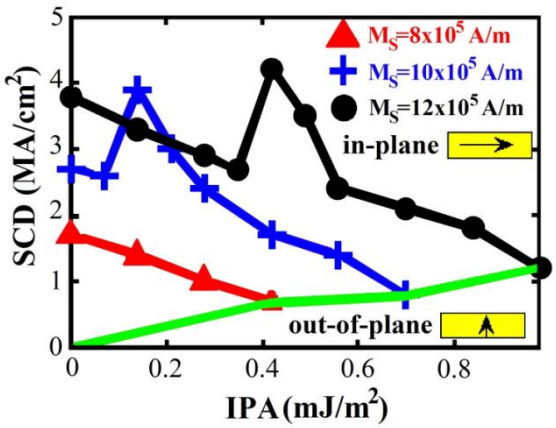

Fig. 2.5: IP SCD depending on the perpendicular anisotropy. The three curves with symbols refer to a saturation magnetization equal to 8x10^5 A/m, 10x10^5 A/m and 12x10^{5}A/m. The green line without symbols represents the minimum values of IPA over which, for a fixed M_S, the free layer is OOP.

We can identify two regions in the phase diagram, divided by the solid line without symbols (green online): (i) the IP free layer region, where the magnetization is collinear to the polarizer; (ii) the OOP region, where the free layer magnetization is perpendicular to the polarizer. The green line, in fact, has been determined from static simulations: for a fixed value of M_S, the point in the line represents the minimum IPA value which gives rise to the transition of the easy axis from IP to OOP. This behavior is due to a competition between the IPA field and the $\mathbf{h_m}$, as explained in the subparagraph 1.1.3. Until the $\mathbf{h_{IPA}}$ contribution is smaller than the $\mathbf{h_m}$ *z*-component, the magnetization keeps IP.

We observe that the IP SCD exhibits a non-monotonic trend as a function of IPA for M_S=10x10^5 and 12x10^5 A/m. In fact, it is evident a first decrease, followed by a sudden increase until the maximum points (peaks in the curves) are reached, for IPA equal to 1.4x10^{-4} and to 4.2x10^{-4} J/m^2, respectively. Then, a monotonically decrease appears again, up to the IPA values where the free layer magnetization turns OOP, equal to 7x10^{-4} and 9.8x10^{-4} J/m^2, respectively. The SCD drops with the increase of the IPA because the IP magnetization becomes energetically less stable, making the magnetization reversal to be easier.

In addition, when increasing the M_S and keeping constant the IPA, the SCD increases as well. This is qualitatively consistent with Eq. (2.2) and Eq. (1.35). In particular, in the latter equation, the $g|\mu_B|\mathbf{j}_{\mathbf{FE\text{-}oop}}/\gamma_0 e M_S^2 t$ factor, that precedes the negative damping term, has to be maintained constant in order to balance the free layer natural damping; thus, to an M_S increase, an SCD rise has to correspond.

In order to explain the peaks in the curves, we have to refer to the spin domains excited in the device: when the IPA field is low, in the elliptical section, three magnetization domains are nucleated, which have a symmetric oscillation at the boundary, called edge mode (see Fig. 2.6).

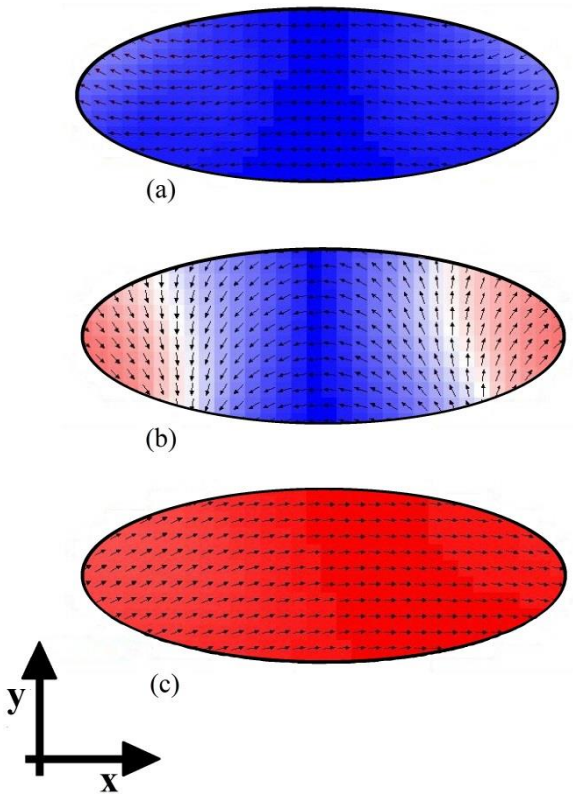

Fig. 2.6: representation of the spin magnetization domains of the MTJ elliptical section, describing the IP switching phenomenon, when the spins are oriented along (a) -*x* and (c) *x* and (b) during the switching.

For the IPA values linked to the jumps in the curves (indicated above), the metastability of the domains is larger, due to a trade-off between

the Oersted field and the STT [103, 104], leading to a longer switching for a fixed current. In fact, studying the switching without the Oersted field, the peaks disappear, as we see in Fig. 2.7. Moreover, we can underline that the observed decreasing linear relationship between the SCD and IPA in Fig. 2.7 qualitatively agrees with the analytical prediction of Eq. (2.2).

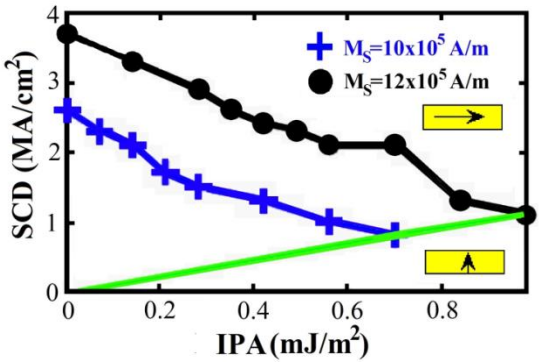

Fig. 2.7: IP SCD as function of the perpendicular anisotropy, without the Oersted field. The two curves refer to a saturation magnetization equal to 10x10^5 A/m and 12x10^{5}A/m.

A similar study is carried out for a switching time of 10 ns. As we see in Fig. 2.8, a shorter switching time needs a higher SCD, about twice larger, whereas the SCD behavior as function of IPA and of M_S is the same explained for a reversal time of 20 ns.

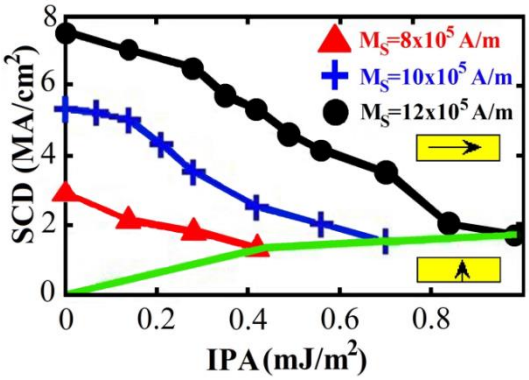

Fig. 2.8: IP SCD depending on the perpendicular anisotropy, without the Oersted field and for a reversal time of 10 ns The three curves refer to a saturation magnetization equal to 8x10^5 A/m, 10x10^5 A/m and 12x10^{5}A/m.

For IPA values larger than 10x10^{-4} J/m^2, the free layer magnetization is OOP. In order to numerically simulate an OOP structure, we orient the polarizer direction along the *z*-axis. Those results are illustrated in Fig. 2.9.

Comparing the two graphs, we note a decrease of the SCD for longer switching times. Focusing only on Fig. 2.9(a) (the same evaluations can be extended to Fig. 2.9(b)), we show that the SCD increases linearly for higher IPA (as analytically confirmed by (2.3)), because of the larger stability of the magnetization *z*-component.

The SCD, for a fixed value of the IPA, increases with the reduction of the M_S. This is in agreement with the bulk anisotropy definition $K_b = K_U / t_{\mathrm{CoFeB}} - 2\pi M_S$ [31, 100] where t_{CoFeB} is the free layer thickness. According to this relationship, higher M_S values lead to a greater OOP anisotropy contribution, favoring the energetic stability of the magnetization.

In addition, contrarily to the IP case, the OOP results show a monotonic trend without peaks. This can be ascribed to the fact that the Oersted field has a null perpendicular component, so that it does not influence the OOP SCD.

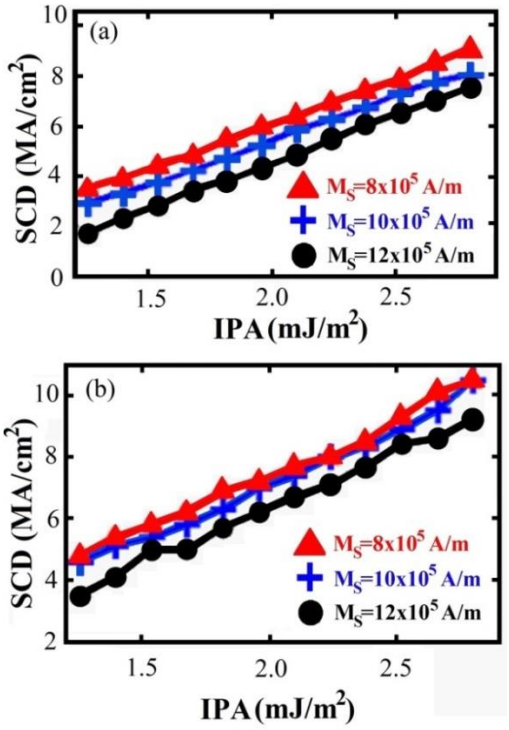

Fig. 2.9: OOP SCD as function of the perpendicular anisotropy, for a switching time of (a) 10 ns and (b) 5 ns. The curves refer to a saturation magnetization equal to $8\text{x}10^5$ A/m, $10\text{x}10^5$ A/m and $12\text{x}10^5$ A/m.

Fig. 2.10 represents the SCD behavior as a function of IPA and of M_S when the thermal contribution at room temperature T=350 K is considered and when the free layer magnetization is IP, neglecting the Oersted field. The SCD plotted values are those ones that allow to obtain the switching phenomenon with a probability of 99.99 %, within a reversal time of 20 ns. As can be noted, the influences of IPA and of M_S on the SCD are the same of the previous cases. Comparing those results with the results obtained for T=0 K (Fig. 2.5 and Fig. 2.7), we point out that the thermal contribution leads to a greater SCD reduction, up to $0.3\text{x}10^6$ A/cm^2 for IPA=$4.2\text{x}10^{-4}$ J/m^2 and M_S=$8\text{x}10^5$ A/m. These are very important results in terms of applications, as the SCD values are compatible with the *state of the art* semiconductor technology, and open interesting perspectives to make STT-MRAMs competitive.

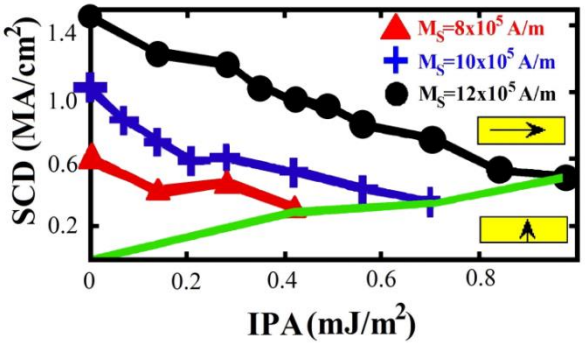

Fig. 2.10: IP SCD as function of the perpendicular anisotropy, without the Oersted field and for a reversal time of 20 ns at a temperature T=350 K. The three curves refer to a saturation magnetization equal to $8\text{x}10^5$ A/m, $10\text{x}10^5$ A/m and $12\text{x}10^5$A/m.

A complete analysis of the device switching mean energy is shown in Fig. 2.11. The energy is computed by the following expression [105]:

$$E_w = \sum \left(dt \cdot \left(J_C \cdot S \right)^2 \cdot R_p + \Delta R \left(\frac{1-\cos\theta}{2} \right) \right) \qquad (2.6)$$

where dt is the time step, J_C is the SCD, θ is the angle between the magnetization of the free layer and the polarizer, and ΔR=R_P-R_{AP} (these values are extracted from the experimental data [100]). About the IP switching (Fig. 2.11(a)), by increasing the IPA, a reduction of the averaged

energy is observed, but, at the same time, a worse thermal stability is achieved as well. Thus, in order to consider a device with good performance, it is necessary to find the right trade-off between the switching energy and the thermal stability limit value. As expected, studying the OOP switching averaged energy (Fig. 2.11(b) and (c)), the lowest dissipated power is reached for the lowest IPA values and for a switching time of 10 ns.

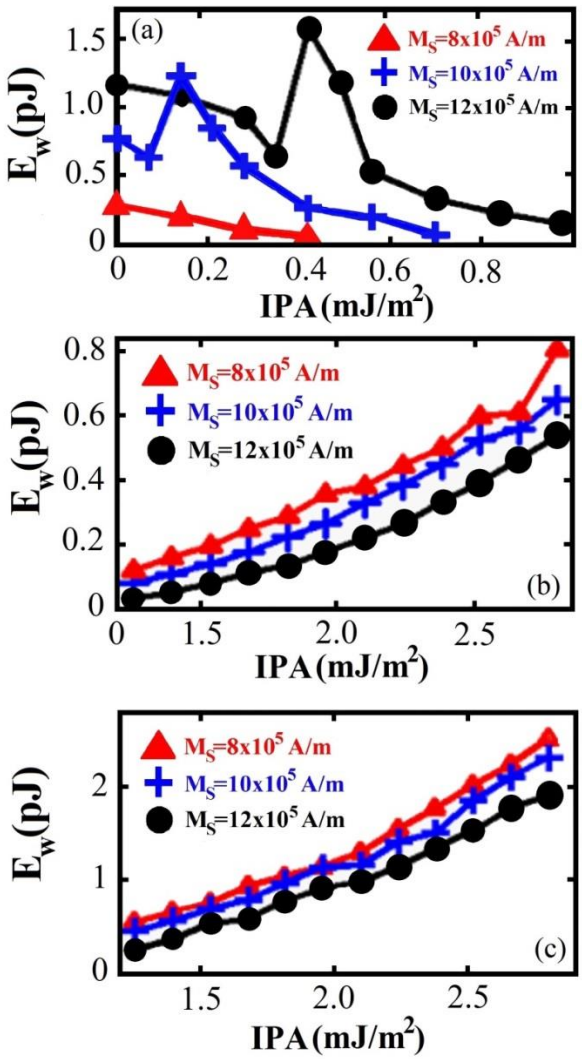

Fig. 2.11: switching averaged energy as function of the IPA for (a) the IP switching, (b) OOP switching in 10 ns and (c) OOP switching in 5 ns.

In summary, we numerically studied the IP and OOP SCD depending on the IPA and on M_S. We showed that the presence of the IPA yields an IP SCD decrease up to values close to 10^6 A/cm^2, for all

considered M_S values and for a writing time of 20 ns. The switching averaged energy diminishes too, with a consequent smaller thermal stability. The effect of the thermal contribution at room temperature was the reduction of the SCD with respect to the SCD values at 0 K. On the contrary, about the OOP switching, the lowest SCD values are reached for low IPA contributions and high M_S ones, either for a writing time of 5 ns or 10 ns. In addition, for shorter writing time, a larger SCD is necessary and this means also a higher switching averaged energy. Finally, these achievements can be useful in the preliminary design stage of STT-MRAMs, as they provide interesting information on the switching currents and the corresponding energy consumption.

2.2.2 Micromagnetic Study of Electrical-Field-Assisted Magnetization Switching in MTJ Devices

Reduction of the critical current and high-thermal stability have been obtained with different strategies, on top of those the use of IPA (see subparagraph 2.2.1). However, the reversal current density is still too high, hence, besides the only STT, other switching mechanisms have to be investigated. Many experimental [106, 107], and macrospin [108] studies have addressed the magnetization reversal assisted by the VCMA (see subparagraph 1.2.7) and, among them, a milestone experiment was performed in [29]. These studies have demonstrated that switching processes can be controlled by a trade-off between H_{ext} and a unipolar voltage pulse, achieving the magnetization switching for current densities of the order of 10^4 A/cm^2 in the presence of a small H_{ext} (+z-direction). For the initial P state (both magnetization along -z-direction), a low voltage pulse is applied to decrease the perpendicular anisotropy in order that the current flowing through the stack switches the state from the P to AP. The P→AP switching is assisted by the external field. For AP→P switching the scenario is different. A high-voltage pulse reduces drastically the perpendicular anisotropy, leading to an IP free layer magnetization. In this case, the STT

related to the large current density flowing through the MTJ stack switches the magnetization.

Here [109], we perform a numerical study by means of micromagnetic simulations to deeply understand that experiment [29]. Our results predict the achievement of electrical-assisted- magnetization reversal in the nanosecond scale at $J_{MTJ}=10^5$ A/cm^2, making such switching mechanism more suitable for high-speed storage applications. The switching occurs via the nucleation of complex magnetization patterns, including vortex and antivortex and, therefore, it is strongly spatially non-uniform, making impossible its understanding in the framework of macrospin approximation.

We study an MTJ stack composed of CoFeB(1.3 nm)/MgO(1.2 nm)/CoFeB(1.6 nm). The thinner and the thicker layers act as pinned and free layer, respectively. A sketch of the structure is shown in Fig. 2.12. We introduce a Cartesian coordinate system with the *z*-axis oriented along the OOP direction and the *x*- and *y*-axis positioned into the film plane. The device has a circular cross section with a diameter $l=200$ nm, $M_S=9\times10^5$ A/m, and $A=2\times10^{-11}$ J/m. Since the free layer is very thin and it is coupled to an MgO insulator, we can consider a $k_u=5.3\times10^5$ J/m^3 [31], which is large enough to stabilize an OOP magnetization easy axis. The magnetization of the pinned layer points down (negative *z*-direction) and $H_{ext}=5.5$ mT is applied along the positive *z*-direction. Initially, the free and pinned layer magnetizations are collinear. The voltage dependence of the anisotropy constant is linear, as shown in [29]. The anisotropy constant is reduced to $k_u=4.8\times10^5$ J/m^3 for the current pulse to switch P→AP, while its value is 4.4×10^5 J/m^3 for the current pulse to switch AP→P.

The micromagnetic simulations are based on the numerical solution of the LLGS equation in Eq. (1.35).

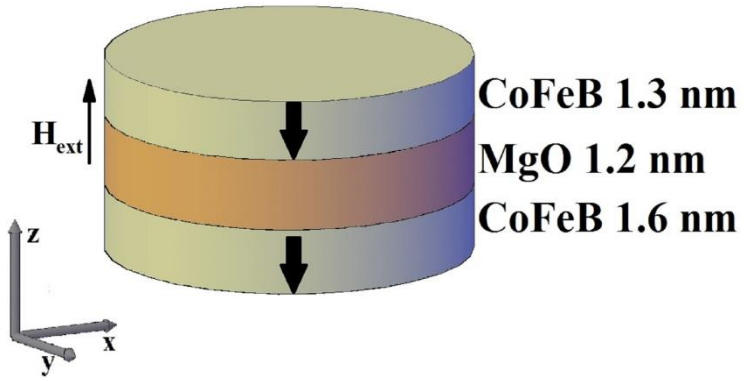

Fig. 2.12: Sketch of the studied MTJ device.

We set α=0.015, a typical value for this material [31]. The thermal field is included as explain in the subparagraph 1.2.2.

Fig. 2.13(a) shows the current pulses (as a consequence of the voltage pulses) as a function of time *t*. We consider that the switching phenomenon is achieved when the normalized *z*-component of the magnetization reaches ± 0.8. The voltage pulses give rise to an anisotropy constant reduction and a current flow through the MTJ. The first pulse, long 15 ns, gives rise to a negative current density of about 6×10^5 A/cm^2. During this time range, the *z*-component of the magnetization starts to reverse (Fig. 2.13(b)), remaining in an oscillatory state. At *t*=18 ns, when the first current pulse is switched OFF, k_u is turned back to the initial value, and due to the external field H_{ext} (pointing upward), the P→AP switching is fully attained. This is a stable state and the $<mz>$ keeps firmly the AP state. At *t*=38 ns, the second higher pulse is applied (J=-7×10^5 A/cm^2) for a time of 3 ns. Consequently, since k_u reduces more and the negative current favors the P state, the AP state becomes unstable, accordingly $<m_z>$ starts to switch back. When the current pulse is switched OFF (*t*=41 ns), the anisotropy field returns to the initial value and helps the full magnetization reversal. At *t*=47 ns, the AP→P switching is achieved. The current densities to achieve both switching processes in less than 50 ns are about one order of magnitude smaller than the one used in STT-MRAM [100].

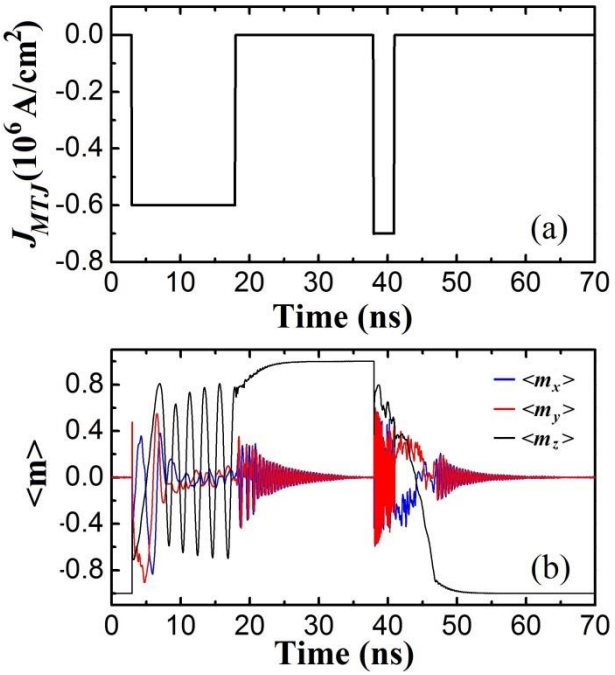

Fig. 2.13: (a) applied current pulses. (b) Time domain plot of the three normalized components of the magnetization (<m_x>, <m_y> and <m_z>, respectively represented in blue, red and black) during a whole reversal process (P→AP and AP→P) as a function of the current pulses in (a).

The P→AP is approximately insensitive to the pulse time duration. With this in mind, we systematically study the AP→P switching as a function of the duration of the current pulse. In detail, we sweep the pulse duration from 2.6 to 7 ns, with a time step of 0.2 ns, finding that only when the pulse time is 2.8, 3, and 5.6 ns the switching is obtained. In Fig. 2.14, we illustrate the temporal evolution of <m_x>, <m_y>, and <m_z> when the pulse duration is 3 ns (Fig. 2.14(a)) and when it is 2.6 ns (Fig. 2.14(b)). After the current pulse is switched OFF, in the former case <m_z> switches from AP to P, whereas in the latter one the reverse does not occur and <m_z> returns to the AP state (<m_z>=+1).

The origin of such dependence can be understood by studying the spatial configuration of the magnetization before and after the current pulse is removed. Fig. 2.15 shows the spatial distribution of the magnetization in the case where the reversal occurs (Fig. 2.15(a) and (b)) and when it is not achieved (Fig. 2.15(c) and (d)). In OOP MgO-based MTJs, the easy axis of

the magnetization is mainly dependent on the competition between the $\mathbf{h_m}$ and $\mathbf{h_{k\perp}}$ (see subparagraph 1.1.3). Once we reduce the perpendicular anisotropy by applying the current pulse, $\mathbf{h_m}$ becomes comparable with $\mathbf{h_{k\perp}}$, and we obtain a quasi-IP structure. In this framework, the applied current is able to excite non-uniform chiral magnetization configurations, such as vortexes and antivortexes [110].

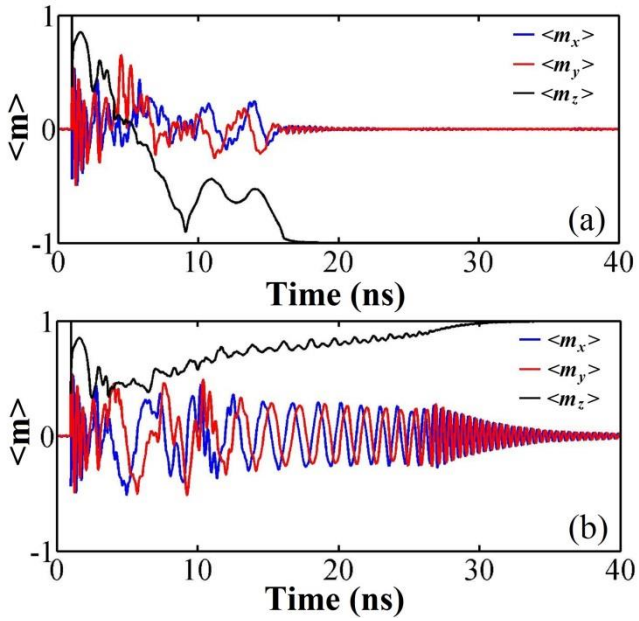

Fig. 2.14: time domain plot for the three normalized components of the magnetization $<m_x>$, $<m_y>$ and $<m_z>$, respectively represented in blue, red and black. (a) Pulse time of 3 ns. (b) Pulse time of 2.6 ns.

When the current pulse is applied, the circular symmetry of the Oersted field nucleates a vortex state. In this case, two vortexes are generated and they rotate in the plane of the structure. In particular, in Fig. 2.15(a) and (b), we can clearly identify two vortexes and two antivortexes (indicated with V and AV, respectively, in the figures); on the other hand, in Fig. 2.15(c) and (d), the second antivortex is pushed out from the free layer and only one antivortex is evident together with two vortexes. In addition, in the cases when the switching is obtained, a larger portion of the magnetization points down along the negative *z*-axis (Fig. 2.15(a) and (b) show blue background color), with respect to the other two cases (Fig. 2.15(c) and (d)). After removing the current pulse, the spatial distribution of

the magnetization evolves in a central domain oriented in the positive out-of plane direction and in two side domains pointing along −*z*-direction (Fig. 2.15(e)). At a later stage, the two side domains collapse each other forming only one domain. Finally, it expands across the whole section of the free layer. A magnetization configuration similar to the previous case is also observed when the current pulse is long 2.6 ns (Fig. 2.15(f)), with the exception that the central domain is larger and the lateral domains. Subsequently, the central domain expands, bringing back the magnetization in the AP state. After removing the current pulse, the vortex state (with +*z* polarity) is destroyed relaxing into a more uniform magnetization configuration pointing upward. The width of this region depends on the spatial position of the vortexes before removing the pulse. If the area of the nucleated central domain is confined in the center of the free layer, the side domains (pointing downward) are quite large to favor energetically the –*z*-magnetization direction (case of Fig. 2.15(e)).

Just to summarize, the AP→P switching is achieved only in the case where two vortexes and two antivortexes are simultaneously nucleated just before the current pulse is switched OFF. On the other hand, when two vortexes and only one antivortex are generated, the AP→P switching does not occur. The number of chiral configurations (four or three) excited when the current pulse is removed depends on the pulse duration.

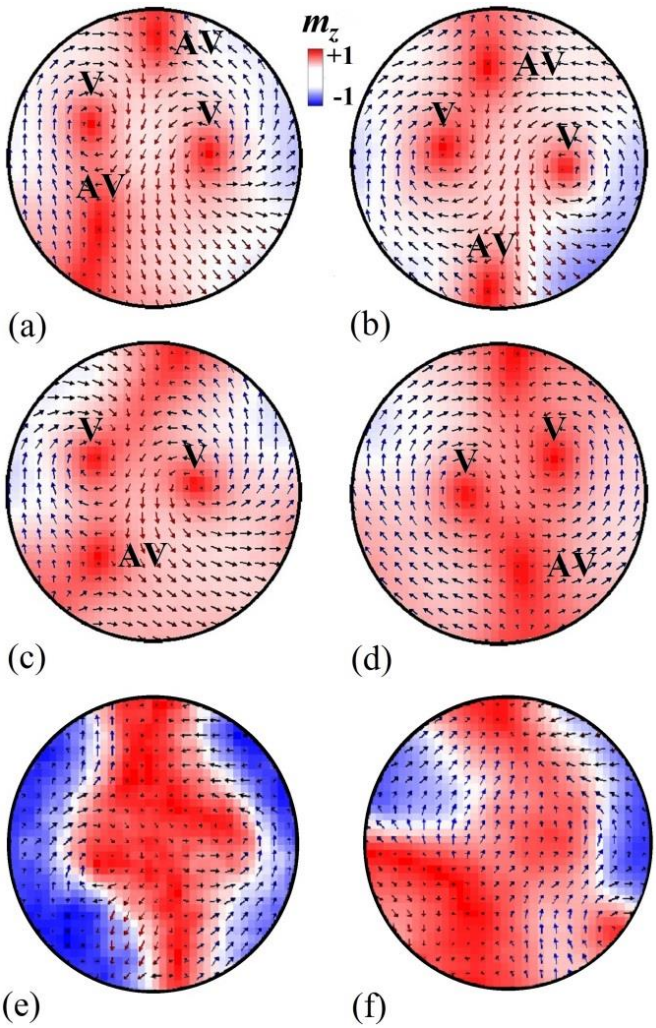

Fig. 2.15: spatial magnetization configurations before the current pulse is switched off. The arrows refer to the *y*-component of the magnetization (blue positive and red negative), whereas the background colors refer to the *z*-component (red positive direction and blue negative direction). The letter "V" indicates vortexes, while "AV" refers to antivortexes. (a) Pulse time of 3 ns. (b) Pulse time of 2.8 ns. (c) Pulse time of 2.6 ns. (d) Pulse time of 3.4 ns. (e) Spatial magnetization configuration after the current pulse is removed for a pulse time (e) t=3 ns and (f) t=2.6 ns.

Finally, we introduce the thermal field as computed at room temperature T=300 K. Fig. 2.16 shows the $<m_z>$ behavior for different current pulse durations in the P→AP switching (Fig. 2.16(a)) and in the AP→P one (Fig. 2.16(b)). In the first reversal process, pulse durations from 6 to 15 ns are considered and in all the cases the magnetization is fully reversed within 30 ns. On the other hand, the thermal effects make the

second switching harder. Only when the pulse durations are 3 and 6.2 ns, the magnetization switching is obtained and for time larger than 80 ns. Therefore, the thermal effect triggers the P→AP switching and delays the process for the AP→P one. This is related to the fact that the P→AP process is strongly dependent on the external field, while the AP→P is mainly related to STT.

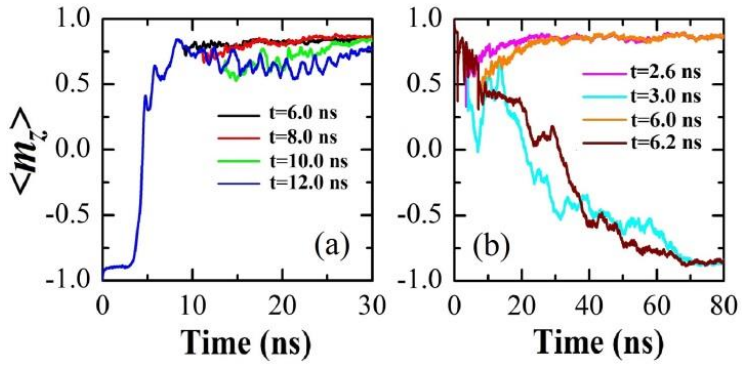

Fig. 2.16: time domain plot for the *z*-component of the magnetization for different time pulses at *T*=300 K. (a) P→AP switching process. (b) AP→P switching process.

In summary, the magnetization switching assisted by an electric field, studied experimentally in [29], has been described within a micromagnetic framework. The dependence of the full switching process on the current pulse time duration has been analyzed, highlighting that the AP→P one occurs only when two vortexes and two antivortexes are simultaneously excited before the current pulse is switched OFF. Thus, the switching behavior is characterized by strongly non-uniform magnetization configurations and, for this reason, it is not possible to describe it using a simple macrospin model. Furthermore, with respect to the experimental case, it has been shown how the whole magnetization reversal process can be executed in a time of about 50 ns, and, by considering also the thermal effect at room temperature, within about 100 ns (much less than the experimental evidence). In this perspective, the results suggest that the electrical-field-assisted switching mechanism can be very useful and achievable from a technological point of view.

2.3 Racetrack memory

Magnetic hard disk drives have been the main memories devoted to store digital data over the past 50 years [111]. The two dimensional technology of the magnetic hard disk drives uses the magnetization direction of small regions on a magnetic thin film as basic element to store information bits. Such regions are read and written by means of a mechanical head, standing few nanometers above the surface of the disk. However, nowadays, those magnetic regions have become so tiny that the technologies needed to read and write bits are reaching fundamental limits. In this concern, the racetrack memory [112] might represent a worthy alternative to hard disk drives, and potentially, it might store 100 times more data than flash memory does today [113].

The racetrack memory is, in its simplest version, composed of a ferromagnetic wire, where magnetic regions with opposite magnetization direction are separated by DWs. It has been introduced by IBM [112] in 2008 and its working principle concerns the displacement of the DWs via the STT (see subparagraph 1.2.6) and the detection of the bit by an MTJ read head (such memory architecture does not need mechanical parts). The DWs motion can be concordant with the electron flow and the achieved velocities are around 100 m/s for current densities of the order of 10^8 A/cm^2. The first prototypes of DWs racetrack memory were made by a soft magnetic material, Permalloy, and exhibited IP domains (see Fig. 2.17(a)) [112]. However, since the width of DWs depends on the shape anisotropy of the wire, soft materials are not suitable as the DWs size can drastically expand, especially in presence of the STT [111]. For this reason, an improved racetrack memory (see Fig. 2.17(b)) was realized using materials with an OOP easy axis of the magnetization due to high perpendicular anisotropy (such as, Cobalt, Cobalt-Nickel alloys, etc.) [114]. In this case, DWs are narrower and more stable, but the motion is not faster. In 2011 [43], large DWs velocities (about 350 m/s for current densities of the order of 10^8 A/cm^2) have been measured in FM/HM bilayers (see Fig. 2.17(c)),

essentially owed to spin-orbit interactions, in terms of enhancement of perpendicular anisotropy of the ferromagnet, nucleation of Néel DW because of the *i*-DMI (see subparagraph 1.3.3), and motion induced by the SHE (see subparagraph 1.3.1) [115]. In the last framework, the direction of motion and velocity of DWs particularly depends on the magnitude and sign of SHE and *i*-DMI. These can be tuned independently by varying the thickness of the HM layer and the composition of the ferromagnetic layer [116, 117]. Very recently, DWs have achieved velocities of about 800 m/s in racetracks formed by synthetic antiferromagnets (see Fig. 2.17(d)) [118]. Basically, two thin CoNi ferromagnets are coupled via the interlayer exchange coupling deriving from an ultra-thin Ruthenium layer placed between them.

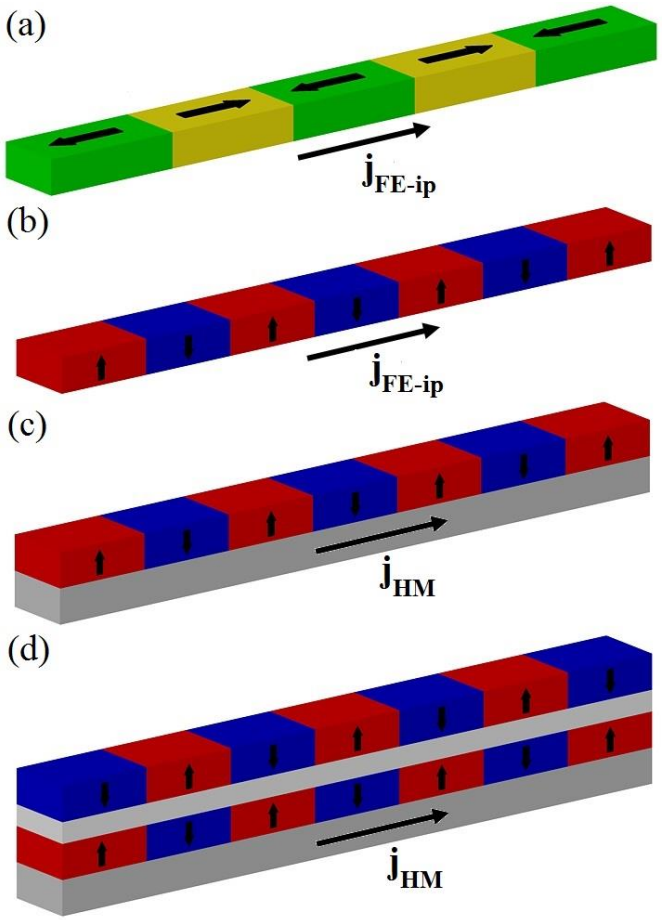

Fig. 2.17: evolution of DW racetrack memory. (a) and (b) represent a single ferromagnetic wire with IP and OOP domains, respectively. (c) bilayer where the DW motion is induced by the SHE. (d) motion of DWs due to the SHE in a synthetic antiferromagnet.

An alternative racetrack memory can be based on skyrmions (see paragraph 1.4). These topologically protected magnetic configurations can directly code information, namely the presence of the skyrmion represents the bit "1", its absence stores the bit "0". Skyrmion racetrack memories would consume less power, (the critical currents to move skyrmions would be lower than the ones for DWs), would be ultra-dense (a skyrmion would occupy less space than a DW, allowing to code more bits in a same racetrack), and would be less sensitive to pinning effects, resulting from the presence of defects (edge and/or surface roughness, dislocations, imperfection, etc.) [47]. This kind of memory has been predicted by Fert *et al.* in 2013 [47] and intensively studied by several groups in the past two years [64, 65, 119]. Currently, all the efforts are pointing towards a reliable experimental evidence of skyrmion motion in nanowires at room temperature.

2.4 Results on racetrack memories

2.4.1 A strategy for the design of skyrmion racetrack memories

A skyrmion racetrack memory can be obtained in four different scenarios (A), (B), (C) and (D) by combining the skyrmion type, Bloch or Néel (see subparagraph 1.4.1), and its motion driven by the STT (see subparagraph 1.2.6) or the SHE (see subparagraph 1.3.1). Fig. 2.18 summarizes the four different scenarios and the insets show the skyrmion types [120]. In scenarios A, C, and D the magnetic strip is 1000x100x1nm^3, while in B it is 100x1000x1nm^3. A Cartesian coordinate system has been also introduced. The current flows always along the positive *x*-direction. In all the scenarios, the skyrmion velocity has both a parallel (longitudinal) and a perpendicular (transversal) component to the electrical current flow [64, 121]. In Fig. 2.18, we indicate the direction of the drift velocity (the larger velocity component). The Bloch skyrmion has been nucleated in agreement with the MnSi phase diagram [63]. The Néel skyrmion has been nucleated by using the same method as described in [65].

The micromagnetic model used is based on the numerical solution of the LLG equation in Eq. (1.41).

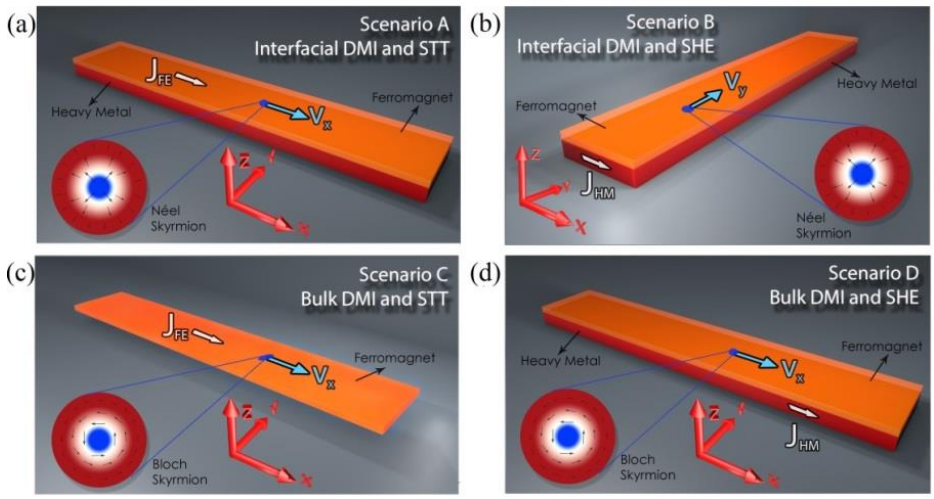

Fig. 2.18: (a) Néel skyrmion motion driven by the STT. (b) Néel skyrmion motion driven by the SHE. (c) Bloch skyrmion motion driven by the STT. (d) Bloch skyrmion motion driven by the SHE. The four insets show the spatial distribution of the Néel and Bloch skyrmion, where the background colors refer to the *z*-component of the magnetization (blue negative, red positive), while the arrows are related to the IP components of the magnetization. The current flows along the *x*-direction. The skyrmion moves along the *x*-direction in the scenarios A, C, and D and along the *y*-direction in the scenario B.

Fig. 2.19(a) shows the drift velocity of the skyrmion as a function of the current j_{FE} (scenarios A, C) and j_{HM} (scenarios B, D). Those results are achieved for an OOP H_{ext} of 250 mT. The external field is necessary to nucleate Bloch skyrmions for the scenarios C and D studied here. The skyrmion velocity is proportional to the injected current with different slopes depending on the scenario. In particular, the Bloch skyrmion velocity driven by the SHE (scenario D) exhibits the largest tunability on current. The STT moves both types of skyrmions (scenarios A and C) mainly along the direction of the electrical current (*x*-axis). The origin of this motion is related to the torque terms $\left(\mathbf{j}_{\mathbf{FE\text{-}ip}} \cdot \nabla\right)\mathbf{m}$ which are non-zero along the current direction only. On the other hand, the SHE moves Néel and Bloch skyrmions with the drift velocity in different directions, namely the former (scenario B) along the *y*-axis and the latter (scenario D) along the *x*-axis.

This is the first important result of our study. The physical origin of the different directions for the drift velocity for Néel and Bloch skyrmions can be heuristically understood by considering the SHE as source of anti-damping [35, 94, 42]. For a current flow along the $+\hat{x}$-axis, the electrons flow is along the $-\hat{x}$-axis, the spin polarization is along the $+\hat{y}$-axis (the spin-Hall angle is negative) and the SHE stabilizes the magnetization component parallel to the spin-current polarization (the spin current diffuses from the HM to the ferromagnet). Fig. 2.19(b) represents a sketch of the mechanism which provides the motion of the Néel skyrmion along the *y*-direction. The SHE reverses the IP component of the magnetization (arrow in the square) from -*y* to +*y* and, assuming rigidity, the magnetization reversing is achieved via a skyrmion shift. The same mechanism occurs for a Bloch skyrmion, but in this case because of the azimuthal chirality, the shift is along the *x*-direction (see Fig. 2.19(c)).

The Thiele's equation [122] for the scenario B has been derived for a comparison with the numerical results. The "hedgehog" like topological magnetic texture of a Néel skyrmion can be parameterized as $\mathbf{m}(x,y)=\sin\theta(\rho)\cos\phi_0\,\hat{\rho}+\sin\theta(\rho)\sin\phi_0\,\hat{\phi}+\cos\theta(\rho)\hat{z}$ by setting $\phi_0=0$ [123]. The translational motion is obtained by projecting the (LLG) equation including the SHE onto the relevant translational modes, yielding [122]:

$$\mathbf{G}\times\mathbf{v}-\alpha\vec{\mathcal{D}}\cdot\mathbf{v}+4\pi B\vec{\mathcal{R}}\left(\phi_0=0\right)\cdot\mathbf{j_{HM}}=0 \qquad (2.7)$$

Here, the vector **G** can be identified as the "gyrocoupling vector", $\mathbf{v}=[v_x,v_y]$ is the velocity of the skyrmion, the matrix $\vec{\mathcal{D}}=\begin{pmatrix}\mathcal{D} & 0\\ 0 & \mathcal{D}\end{pmatrix}$ is the dissipative tensor describing the effect of the dissipative forces on the moving magnetic skyrmion, $\vec{\mathcal{R}}$ is the IP rotation matrix. The coefficient *B* is linked to the SHE. From Eq. (2.7), a simple expression of the skyrmion velocities can be derived:

$$\begin{cases} v_x = \dfrac{\alpha \mathcal{D} B}{1+\alpha^2 \mathcal{D}^2} j_{HM} \\ v_y = \dfrac{B}{1+\alpha^2 \mathcal{D}^2} j_{HM} \end{cases} \tag{2.8}$$

Both components of the velocity are proportional to j_{HM}. However, being v_x also proportional to the Gilbert damping (α<<1), it follows that v_x<<v_y. This result confirms the micromagnetic predictions. On the other hand, the Thiele's equation derived for the scenario D related to the Bloch skyrmion $\left(\phi_0 = \pi / 2\right)$ shows that v_y<<v_x [121], confirming again our numerical results. A complete description of the derivation of the Thiele and the velocity equations for Néel and Bloch skyrmion driven by the SHE can be found in Supplementary Material S1 of [120].

The results of Fig. 2.19(a) also indicate that for the scenarios A, B and C, the skyrmion is stable for a wide range of current <120 A/cm^2. Considering the four scenarios, although the scenario D seems to be the most promising configuration from a technological point of view (larger slope of the velocity vs current curve), it is stable up to j_{HM}=15 MA/cm^2 and at low temperature [59, 124, 125]. Scenario C has been studied both theoretically and experimentally [63, 124, 126]. On the other hand, the experimental implementations of the scenarios A, B and D have not been achieved yet, representing challenges and routes in the design of magnetic materials and devices.

The analysis of the four scenarios leads to the conclusion that one of the most promising strategies for the design of a skyrmion racetrack memory is the framework of the scenario B (Néel skyrmion, SHE) when considering both the skyrmion velocity vs current, scaling and the relative ease of creating these systems (i.e. these systems can be created with standard magnetron-sputtering or evaporation deposition techniques and can be polycrystalline) [43, 115, 127]. For this reason, in the rest of this study we will focus on the scenario B. Fig. 2.19(d) shows the drift velocity as a

function of the current in presence of thermal fluctuations T=350 K and for both a perfect and rough strip. We consider an edge roughness by randomly removing regions from the strip boundaries with a uniform probability distribution characterized by the typical roughness size D_g=4 nm [128]. Those results show that the skyrmion motion is qualitatively not affected by thermal fluctuations and roughness. Quantitatively, the maximal applicable current reduces to 100 MA/cm^2 and, in presence of the roughness, the threshold current to move the skyrmion increases to 10 MA/cm^2.

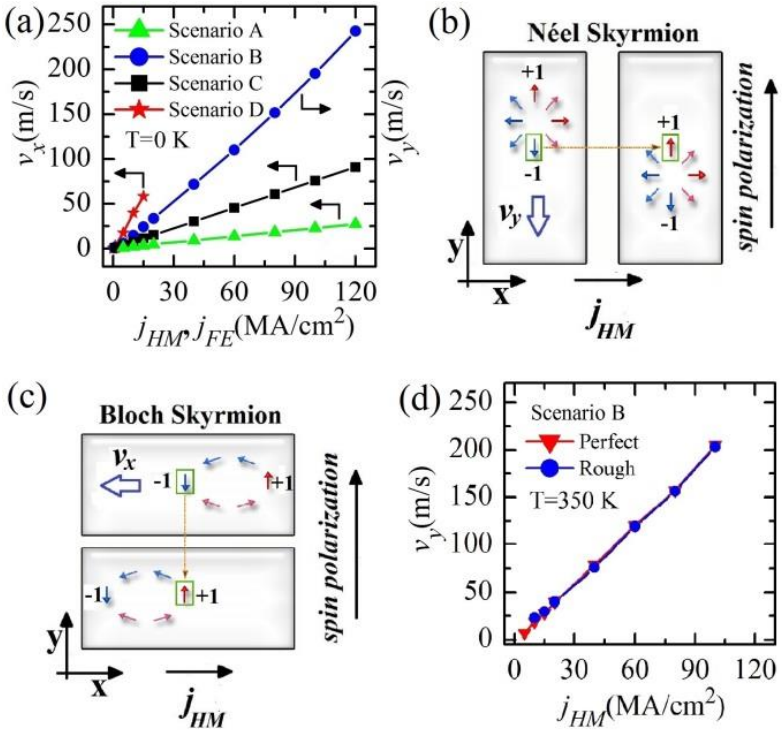

Fig. 2.19: (a) A comparison among the skyrmion velocities obtained for each scenario (A, B, C, and D). The current j_{FE} is related to the scenarios A and C while j_{HM} to the scenarios B and D. (b) Sketch of the motion mechanism of the Néel skyrmion driven by the SHE along the *y*-direction. (c) Sketch of the motion mechanism of the Bloch skyrmion driven by the SHE along the *x*-direction. (d) Skyrmion velocities as a function of j_{HM} obtained for the scenario B: (i) thermal fluctuations (T=350 K) and perfect strip (red curve) and (ii) thermal fluctuations (T=350 K) and rough strip (blue curve). The arrows for (b) and (c) refer to the IP components of the magnetization, the spin-polarization of j_{HM} is also displayed.

We have also performed a systematic study as a function of the external OOP H_{ext} obtaining no qualitative differences in terms of skyrmion velocity vs current. Fig. 2.20(a) shows the stability phase diagram of the

Néel skyrmion as a function of D and H_{ext}. The coloured part of the diagram identifies the region where the skyrmion is stable. It is interesting to notice how, reducing H_{ext}, the range of the i-DMI where the skyrmion is stable is also reduced. The line inside this region indicates the values of the i-DMI and H_{ext} which maintain the skyrmion diameter constant at 46 nm. In order to reduce the power dissipation and to make the design of the skyrmion racetrack memory much simpler, one of the most interesting solutions should be achieved with no bias field (the i-DMI parameter is 1.8 mJ/m^2). For a fixed thickness, D can be controlled experimentally by changing the thickness or the composition of the HM [129, 130] and the thickness of the ferromagnet [65].

Fig. 2.20(b) shows the skyrmion velocity as a function of j_{HM} at zero field, zero temperature and perfect strip (black curve). It increases linearly with the current up to 117 m/s at j_{HM}=60 MA/cm^2. Fig. 2.20(b) also shows the skyrmion velocity as computed from Eq. (2.8) (green line with triangles). The quantitative accordance between the analytical and the micromagnetic results is excellent, indicating a simple tool for a preliminary design of skyrmion racetrack memories (scenarios B and D). The comparison between the skyrmion velocity as a function of the current for different field configurations (compare Fig. 2.19(d) with Fig. 2.20(b)) points out that the slope does not change (skyrmion size is constant), while reductions of the maximal applicable current are observed up to 60 MA/cm^2 at zero external field. The reduction of the current working region is linked to the transient breathing mode [131] of the skyrmion, excited by the application of the current. In particular, for a fixed current, the expansion of the skyrmion increases as H_{ext} decreases (the OOP field stabilizes the magnetization state out of the skyrmion). Fig. 2.20(c) illustrates the time domain evolution of the skyrmion diameter for three different current densities (30, 40 and 50 MA/cm^2). The maximal expansion of the skyrmion increases with the current, reaching the boundary of the strip at j_{HM}=65 MA/cm^2; as consequence, the skyrmion state disappears giving rise to a

complicated magnetic pattern. This is the second important result of our study, underlining the technological limit of a skyrmion racetrack memory. In other words, at high currents, the information stored in the skyrmion can be lost. Fig. 2.20(d) also shows a comparison of the skyrmion velocity as a function of the current for an ideal strip (T=0 K) (black curve) and a rough strip and room temperature (T=350 K) (red curve). Again, the thermal fluctuations and the roughness do not qualitatively affect the skyrmion motion.

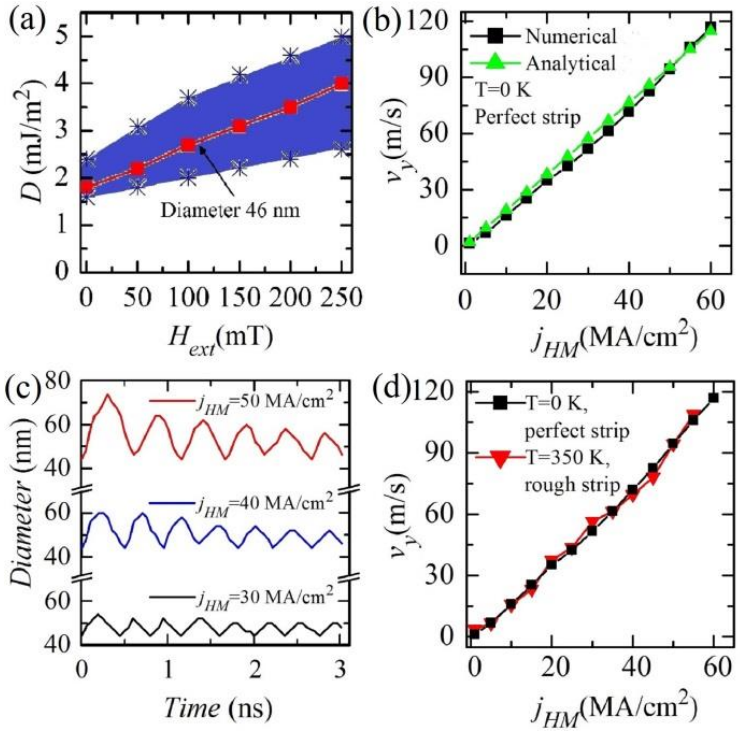

Fig. 2.20: (a) phase diagram (*i*-DMI parameter vs. external field) of the skyrmion stability. The colored part highlights the region where the skyrmion is stable and the red curve points out the values of D and H_{ext} for which the skyrmion diameter is 46 nm. (b) Skyrmion velocity as a function of the current calculated by micromagnetic (black curve) and analytical computations (green line). (c) Time domain evolution of the skyrmion diameter during the transient breathing mode at three different values of the j_{HM}, 30 MA/cm^2 (black curve), 40 MA/cm^2 (blue curve) and 50 A/cm^2 (red curve). (d) A comparison of skyrmion velocity as a function of the current for an ideal strip (T=0K) and a rough strip and room temperature.

We now wish to highlight the differences in our results of scenario B with a previous work [65], detailing a scheme for skyrmion motion. In that

work, the motion of the Néel skyrmion driven by the SHE is in the same direction of the applied electrical current and it is achieved for current densities $\leq$5 MA/cm^2. This seems to contradict both our analytical theory and the results from micromagnetics in scenario B where the skyrmion motion is orthogonal to the current flow direction. With this in mind, we studied the Néel skyrmion motion driven by the SHE, but now in a strip 1000x100x1 nm^3 (see Fig. 2.21(a) scenario B*). Fig. 2.21(b) shows the *x*-component of the skyrmion velocity as a function of the j_{HM}. At zero temperature and for a perfect strip (red curve), the threshold current density is 0.01 MA/cm^2, while the skyrmion motion is achieved up to 0.5 MA/cm^2 (v_x=22.8 m/s). This is in accordance with the previous result. However, one can also see that the *y*-position changes during the course of the trajectory and moves closer to the edge of the wire. Our results show that the *y*-position Δy_2, that the skyrmion equilibrates at during the course of its *x*-motion, is dependent on the current. At larger current, the skyrmion is expelled from the strip. The current range over which the skyrmion is stable and the current at which the skyrmion is expelled from the wire seems to depend heavily on thermal fluctuations (T=350K) and wire edge roughness (Fig. 2.21(b) black curve). Edge roughness tends to slow down the skyrmion and to facilitate its expulsion. These facts suggest that the *x*-directional motion of the skyrmion and the *y*-position of the skyrmion in the wire arises from an interplay among the SHE, magnetostatic confinement [123] and boundary conditions imposed by the *i*-DMI [48].

The role of the boundaries in skyrmion motion constitutes the key difference between the two skyrmion motions in B and B*. Eq. (2.8) for the velocity derived for the scenario B could, in fact, be generalized to the scenario B* by taking into account the confinement effect (additional term in Eq. (2.7)) [123].

We have further analyzed the effect of the confinement on the skyrmion motion in B* for different *w* of the strip. Fig. 2.21(c) shows the *x*-component of the skyrmion velocity as a function of j_{HM} for three values of

w (100, 150 and 200 nm). The three curves overlap indicates that the confinement effect gives rise to a steady-state velocity independent of w. When the current is injected, the skyrmion moves from the equilibrium position (at a distance Δy_1 (half width), see Fig. 2.21(a)), along y and x. After a transient time Δt_1, v_y=0 m/s and the skyrmion stabilizes at a distance Δy_2 from the boundary. Δy_2 decreases as the current increases. The transient time is around 30 ns for the current range studied, whereas the travelling distance Δx_1 during this transient time increases linearly with the current, from 74 nm at j_{HM}=0.01 MA/cm^2 to 406 nm at j_{HM}=0.5 MA/cm^2. In addition, the distance Δy_2 is independent of w for j_{HM} > 0.1 MA/cm^2. The existence of the transient Δt_1 introduces an additional bottleneck in this kind of racetrack memory.

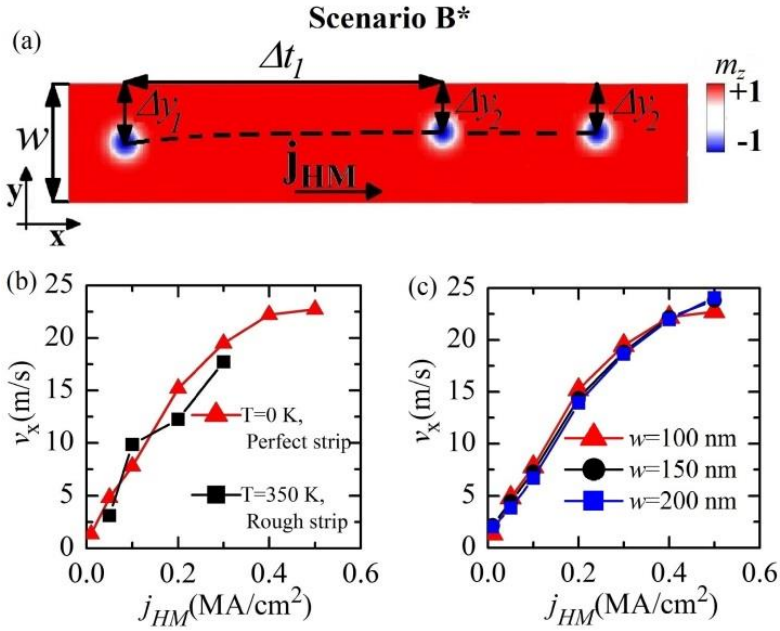

Fig. 2.21: (a) sketch of the skyrmion motion due to the SHE in a sample confined along the y-direction. (b) Skyrmion velocity (x-direction) as a function of the current: (i) no thermal fluctuations and perfect strip (red curve) and (ii) thermal fluctuations (T=350 K) and rough strip (black curve). (c) Skyrmion velocity as a function of the current when the strip width w is 100 nm (red curve), 150 nm (black curve) and 200 nm (blue curve). The colors for (a) refer to the z-component of the magnetization (blue negative, red positive).

A comparison of the scenario B* with the scenario B (Fig. 2.20(b) and Fig. 2.21(b)) demonstrates that the threshold current is smaller in scenario B*, and that therefore the geometry and setup of B* can be used for ultra-low power storage devices. However, the skyrmion motion in scenario B is much more robust to thermal fluctuations and is much less sensitive to defects and edge roughness that are present in real devices. Skyrmion motion in scenario B can also be achieved for a wider current range and it is stable at larger currents implying larger skyrmion velocities.

In summary, we have analyzed the possible technological scenarios for controlling the shifting Néel or Bloch skyrmions driven by SHE or STT. Our results indicate that scenario B (Néel skyrmion motion driven by the SHE) is one of the most promising from a technological point of view and its experimental implementation could be achieved bearing in mind that the skyrmion mainly moves perpendicularly to the electrical current flow. Our results suggest a new route to design and develop a more efficient skyrmion racetrack memory.

3. SPIN-TORQUE OSCILLATORS AND DIODES

This chapter describes the use of spintronic devices as oscillators and diodes. Paragraph 3.1 focuses on oscillators, providing a brief discussion on their most important properties. Paragraph 3.2 introduces the STNOs, describing the working principle, the classifications, and the state of the art. Paragraph 3.3 shows the results obtained about STNOs. Paragraph 3.4 deals with diodes, pointing out functionality and characteristics of STDs. The last paragraph includes the results achieved on STDs.

3.1 Introduction on oscillators

In general, an oscillator is a device where, from a constant input, a periodic output is generated. For instance, harmonic oscillators (the most important class of oscillators), exhibit an oscillating output characterized by a single mode, and, hence, by a single frequency. Oscillators have oodles of applications in many fields, such as digital circuits, quartz digital watches, satellite receivers, radio and video transmission, and can be technologically implemented in several ways: LC tank voltage controlled oscillators, crystal

oscillators, relaxation oscillators, STNOs, etc. The most significant features of oscillators are:

- *frequency tunability*, which should be adjustable as fast as possible in operation over a specified frequency range (fundamental requirements for radio applications, where radios receive and transmit signals at different frequencies);
- *phase noise*, which indicates short-time random variations of the frequency;
- *frequency stability*, which refers to the capability of keeping the same frequency over a certain time interval;
- *power dissipation*, which has to be as minimal as possible for applications;
- *supply voltage*, which is the input to be varied in order to tune the oscillator frequency. Noise in the supply voltage can introduce phase noise;
- *output power*, which has to be as large as possible. An approximated expression of the power efficiency $\eta_p = P_{out}/P_{in}$, being P_{in} the supply power and P_{out} the output power;
- *linewidth*, which defines the full width at half maximum (FWHM) of the frequency spectrum. Narrower linewidths are suitable for improving the quality of oscillators;
- *quality factor Q*, which can be defined as $Q = f_0/2\Delta f$, being f_0 the resonance frequency and Δf the linewidth;
- *injection locking*, which occurs when an input signal, characterized by a large enough amplitude and a frequency close enough to one of the multiples of the fundamental free-running frequency, locks the free-running oscillation frequency to its own one;
- *immunity to disturbances*, deriving from either the supply voltage or the substrate where the oscillator in embedded.

3.2 Spin-torque nano-oscillators

STNOs are among the smallest oscillators existing in nature [23]. A standard STNO can be composed of either a spin-valve or an MTJ (see Fig. 3.1(a)) and its working principle is due to the two spintronic fundamental phenomena (as for the case of STT-MRAMs): STT (see subparagraph 1.2.4) and Giant Magnetoresistance (GMR) for spin-valves (see subparagraph 1.2.5) or TMR (see subparagraph 2.1.1) for MTJs. Indeed, the last two effects originate from the same physical interaction, namely the spin-dependent scattering of electrons when they travel from the pinned layer to the free layer and vice versa, with the difference that the GMR involves electronic transport in metals (in spin-valves the spacer is an electrical conductor), whereas the TMR comprises electron tunneling. However, the definition of the GMR ratio is exactly the same of Eq. (2.1). The GMR was discovered in 1988 by Fert [132] and Grunberg [133] (both awarded by the Nobel Prize in Physics in 2007) and led to a revolution in the reading technology of hard disk drives by the fabrication and commercialization of GMR read heads in 1997 [134, 135, 136, 137]. It is necessary to specify that the TMR was discovered in 1975 (see subparagraph 2.1.1), but it did not receive much attention until higher quality barriers were developed. However, nowadays, the TMR is quite larger than the GMR, enabling an increase of the sensitivity of hard disk drives read heads, which have been based on the TMR since 2004 [138].

The functionality of an STNO can be described as follows: the STT, due to the perpendicular spin-polarized current created by the pinned layer, if large enough to compensate the damping losses of the free layer, induces a persistent precession of its magnetization. Consequently, the magnetoresistive effect (GMR or TMR) converts the magnetization oscillation into an electrical resistance oscillations (see Fig. 3.1(b)), and, thus, into a microwave voltage linked to the product of the dc injected current and the oscillating resistance.

The oscillation dynamics in STNOs are micromagnetically analyzed by means of Eq. (1.34) and Eq. (1.35) for spin-valve and MTJs, respectively.

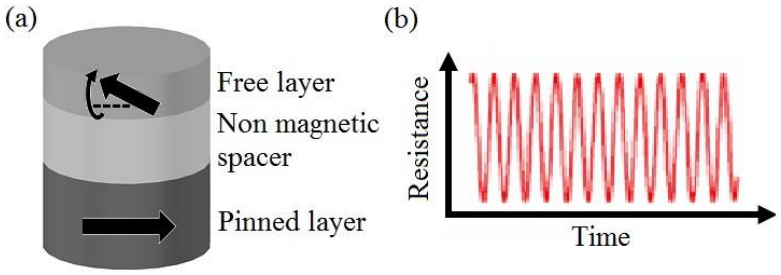

Fig. 3.1: (a) schematic illustration of an STNO. (b) example of time domain oscillation of the STNO electrical resistance, when precessions of the free layer magnetization are excited.

3.2.1 Classification of STNOs

A few classifications of STNOs can be done according to different parameters [23, 139]. As already discussed, a first categorization concerns the type of device, spin-valve or MTJ. A second classification regards the geometry. STNOs can be patterned into *nanopillars*, where the electrical currents flows through the entire cross section of the multilayer (see Fig. 3.2(a)), and into *nano-contacts* (also known as *point-contact geometry*), where the currents is locally injected via an electric contact into an extended free layer (see Fig. 3.2(b)). Thirdly, STNOs can be classified according to the magnetization configuration: *in-plane* oscillators, with both free and pinned layer magnetizations having an IP easy axis (see Fig. 3.2(c)); *perpendicular oscillators*, where both free and pinned layer magnetization orientations are orthogonal to the plane (see Fig. 3.2(d)); *in-plane-perpendicular* oscillators, having an IP pinned layer and an OOP free layer (see Fig. 3.2(e)). Finally, the oscillation can be related to a *quasi-uniform precession* of the magnetization or to a *soliton mode* (i.e. vortexes can rotate around the nano-contact [140], skyrmions can do the same [71] or can be characterized by an expansion and contraction of the core – breathing mode [69, 70]).

It is possible to highlight some characteristic linked to each of the previous classification.

In spin-valves, large currents can be injected to generate oscillations, however the output power will be relatively small as the GMR is low. On the other hand, MTJs exhibit a larger output power due to higher TMR than the GMR, but the maximal applicable current is limited by the barrier breakdown voltage (about 1 V) [23, 139].

The oscillating magnetization dynamics are excited by larger current densities (10^7-10^8 A/cm^2) in nano-contacts and lower ones (10^6-10^7 A/cm^2) for nanopillars. On the other hand, STNOs with point-contact geometry are characterized by a narrow linewidth (1-10 MHz) and, therefore, higher quality factor (up to 18000) [23, 139].

IP and perpendicular STNOs need the application of an external magnetic field, tilted a few degrees away from the free layer magnetization easy axis, in order to produce the microwave oscillations, whereas in-plane-perpendicular oscillators can emit microwave signals even at zero external field [23, 139].

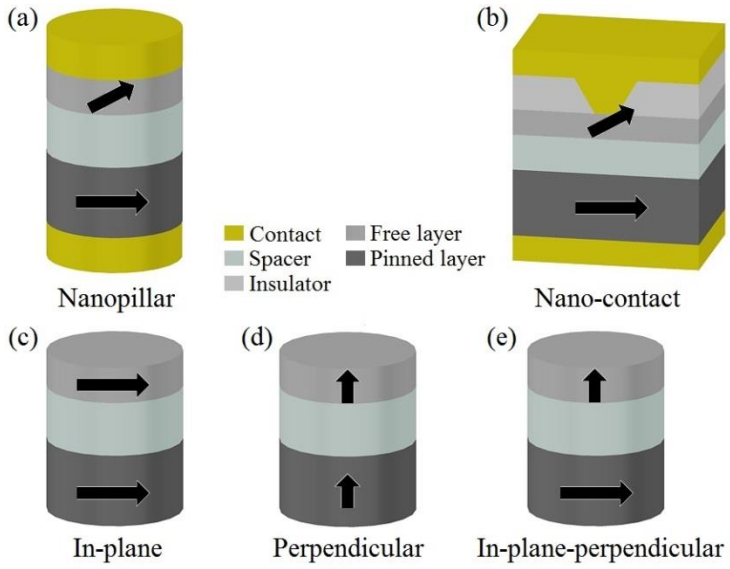

Fig. 3.2: (a) and (b) geometry classification of STNOs, (a) nanopillars and (b) nano-contact. (c), (d) and (e) magnetization configuration classification of STNOs, (c) in-plane, (d) perpendicular and (e) in-plane-perpendicular.

Vortex based STNOs exhibit an oscillation frequency limited to about 1 GHz, while the frequency range of uniform STNOs is much larger [23, 139].

Eventually, it is worthy to mention that, very recently, a further kind of oscillator has been designed, which is based on the SHE. Two SHE oscillator configurations have been experimentally studied: a FM/HM bilayer patterned as both a disk [36] and a wire [141], and the three terminal device (see subparagraph 1.3.4).

3.2.2 Output power and linewidth

Two of the most important features of STNOs are the output power and the linewidth. A major challenge in improving the performance of STNOs is to achieve high output power accompanied by narrow linewidth [23, 139].

The output power is linked to the magnetoresistive effects of spin-valves and MTJs. As explained above in this paragraph, the magnetization oscillation induced in the free layer by a dc I is converted in an oscillating resistance $R = R_m + (\Delta R/2)\cos(\omega t)$, being R_m the average resistance value, ΔR and ω the amplitude and the frequency of the oscillating resistance, respectively. If the STNO supplies an inductance load R_L, the time-averaged delivered power to the load is [23, 139]:

$$P_{out} = \frac{V_{out}^2}{2R_L} = \frac{I^2}{8}\frac{\Delta R^2 \cdot R_L}{(R_m + R_L)^2} \tag{3.1}$$

Therefore, in order to increase the STNO output power, the ratio R_L/R_m has to be enhanced as well as the amplitude of the oscillating resistance. In particular, $\Delta R = M_{\max} \cdot GMR(\text{or } TMR)$, hence the amplitude of the magnetization oscillation $M_{\max}$ can be increased too, together with the magnetoresistive effect. Larger oscillation amplitudes are obtaining by increasing the ratio J / J_{th}, where J_{th} indicates the threshold value of the

current density over which the persistent magnetization precession is excited. Unfortunately, in MTJ based STNOs the maximal applicable current is limited by the barrier breakdown voltage, therefore, the other possibility is to decrease J_{th}. On the other hand, spin-valve STNOs exhibit a lower GMR, even though it is possible to inject larger currents.

Let's, now, provide two examples for the output power. In the case of spin-valves, typical experimental values are GMR in the range (0.1–10%), I=1 mA, R_m=5 Ω, ΔR=0.5 Ω, and R_L=50 Ω, leading to P_{out}=0.5 nW. In the case of an MTJ, with TMR>50%, considering that I=1 mA, R_m =450 Ω, ΔR=150 Ω, and R_L=50 Ω, the output power can reach the value of 0.5 μW. Nowadays, the measured power has achieved a value of about 0.28 μW MgO based MTJs with large TMR and IPA. A correlated parameter is the power efficiency, which can be expressed as [139]:

$$\eta_p = \frac{P_{out}}{P_{in}} = \frac{V_{out}^2}{2R_L R_m I^2} = \frac{1}{8}\frac{\Delta R^2 \cdot R_L}{R_m \left(R_m + R_L\right)^2} \tag{3.2}$$

and it results low ($0.5\text{x}10^{-3}$ – $5\text{x}10^{-3}$) for both spin-valves and MTJs.

A method to increase the output power of STNOs is to synchronize more oscillators, i.e. via the phase locking phenomenon [142, 143]. In this way, considering 10 spin-valves connected in series, it would be possible to obtain an output power of 62 nW, while 16 μW for 10 typical MTJs, and 28 μW for 10 optimized MgO based MTJs [23, 139].

The linewidth, as defined above in this chapter, is deeply influenced by the geometry and material parameters of STNOs, as well as the working conditions. For instance, in point-contact oscillators the linewidth ranges from a few MHz to 100 MHz, whereas in nano-pillars can reach the order of GHz. This difference can be ascribed to the effective free layer area involved in the dynamics. Fig. 3.3 shows an example of linewidth at room temperature for an MTJ having a nanopillar geometry [23].

The linewidth is also related to thermal fluctuations and phase noise, and depends on the emitted power P_{out} [144], namely it decreases when P_{out}

increases. This implies that small oscillation amplitude are affected by the thermal fluctuations, whereas large amplitudes show a sharper linewidth. Moreover, an increase of the linewidth can be due also to effects caused by device edges, defects or inhomogeneous current injections, which induce non-uniform precessions characterized by different frequencies.

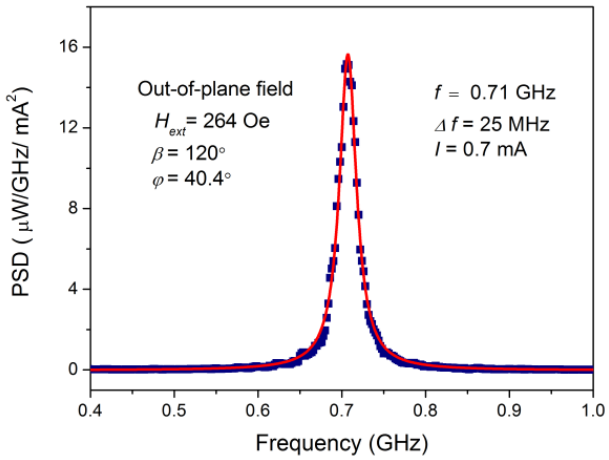

Fig. 3.3: example of MTJ-based nanopillar STNO spectra showing a narrow linewidth at room temperature [23].

Several strategies have been used to reduce the linewidth. One aims at the identification of operational points where the non-linear frequency shift is as low as possible [145, 146]. Another one involves the excitation of a vortex mode, which can be characterized by a sub-MHz linewidth [147, 148, 149]. A further method concerns the synchronization of more STNOs [150, 151, 152], which can exhibit a linewidth one order smaller than the same unsynchronized STNO.

3.2.2 State of the art

In 1998, Tsoi *et al.* [153] proved the excitation of steady-state magnetization dynamics in point-contact geometries where a perpendicular external field was applied. Later, these oscillations were demonstrated to be related to exchange-dominated cylindrical spin wave modes (called 'Slonczewski modes' [154]). In 2003, persistent magnetization precessions were measured in Co/Cu/Co spin-valves with a nanopillars geometry [155].

In the same year, Fuchs *et al.* showed persistent magnetization oscillations in MTJs with an AlO tunnel barrier [156]. A year later, experiments on point-contact geometries with an applied IP field were carried out, demonstrating the excitation of spin-wave localized modes called "bullet mode" [157]. Therefore, it was possible to represent a phase diagram of the magnetization dynamics in spin-valves with point-contact geometries as a function of the direction of the applied field [23]. Particularly, it exists a critical angle below which bullet modes are generated and above which Slonczewski modes are excited. Indeed, in presence of a large Oersted field, these two modes can be excited in a non-stationary way in a specific range of field angles and currents [158, 159].

In 2006, thanks to improvements in the oxide barrier fabrication, a clear oscillation was detected in MTJs, characterized by a narrow linewidth [160]. In 2007, the first in-plane-perpendicular nanopillar STNO was realized and the first observation of vortex dynamics in spin-valves with a thick enough free-layer (60 nm) was accomplished [147]. In 2008, the rotation of a vortex around the electric contact in point-contact spin-valve was achieved [161], and, in the same configuration, also rotating vortex–antivortex pairs were observed [162]. More in detail, in the former case, the dynamics is linked to both pinned and free layer. In 2009, Boone *et al.* [163] proposed an alternative design of STNOs, by using a ferromagnetic nanowire with the electric contact placed in the middle of the strip. A year later, vortex dynamics were measured in MTJs, and, differently from spin-valves, the dynamics was excited in only the free layer [148]. In 2010, magnetization precessions were also achieved in nano-contacts spin-valves with an OOP free layer [164]. Afterwards, thanks to the discovery of the IPA, it was possible to induce magnetization oscillations in IP and OOP MTJs [165, 166]. In those years, an STNO composed of two IP free layers and two OOP polarizers were fabricated, which exhibited a very large oscillation at zero bias field [167]. In 2012, persistent magnetization oscillations driven by the SHE were observed both in bilayered nano-disks

[36] and in three-terminal devices [49]. Later, in 2014, Duan *et al.* introduced the first nanowire oscillator based on the SHE [141].

Recently, skyrmion based STNO have been studied, characterized by either a rotation of the skyrmion around the electric contact in point-contact device [71] or an expansion-shrinkage mode of the skyrmion core, known as "breathing mode" in nano-contact spin-valves [69, 70].

3.3 Results on STNOs

3.3.1 Dynamical properties of three terminal magnetic tunnel junctions: spintronics meets spin-orbitronics

We study a three terminal device, which efficiently couples Spintronics with Spin-Orbitronics [168]. The pioneering idea of that system has been introduced by *Liu et al*. [49]. However, in that experimental work, the current injected via the third terminal was only used to control the IPA maintaining the STT negligible. Differently, here we predict the behavior of that system when also the STT contribution is significant. The three terminal device is composed of an MTJ CoFeB(2)/MgO(1.2)/CoFeB(4)/Ta(5)/Ru(5) (thicknesses in nm) built over a Tantalum (Ta) strip (6000x1200x6 nm^3) [49]. The CoFeB(2) and the CoFeB(4) act as free and pinned layer of the MTJ, respectively. Fig. 3.4 shows a detailed sketch of the system. We introduce a Cartesian coordinate system where the *x*-axis is oriented along the larger dimension of the Tantalum strip, the *y*- and *z*-axis are related to its width and thickness, respectively. There are many advantages to study this system. First of all, the magnetization precession is read via the tunneling magneto-resistive effect instead of the AMR [169]. In fact, the oscillator output power can reach the same order of magnitude of the *state of the art* MTJs-based oscillators [23, 166, 170]. Secondly, it is possible to control the injection of two current densities: the IP j_{HM} in the Tantalum strip and the perpendicular J_{MTJ} flowing into the MTJ-stack, achieving an additional degree of freedom

in the control of the magnetization dynamics. In addition, the use of Ta/CoFe/MgO gives rise to a spin-Hall angle two times larger than the one in Pt/Co/AlO [35].

Our findings are important both in the understanding the types of spatially-inhomogeneous dynamics, that can be excited in presence of SOTs, and for an optimized design of devices which couple Spintronics and Spin-Orbitronics. The two main results of this study are: (i) micromagnetic understanding of the dynamical properties of those oscillators in terms of oscillation frequency and spatial distribution of the excited modes, and (ii) a spintronic/spin-orbitronic synchronization scheme which can be used to improve the properties of the oscillators (linewidth, output power).

Eq. (1.48) has been numerically solved to study the dynamics of the free layer magnetization.

First of all, we carried out preliminary numerical simulations of the same structure studied by Liu *et al.* in [49], analyzing different cross-sections and free layer thicknesses, in order to geometrically optimize the device response in terms of magnetization dynamics. In the following, we present the micromagnetic study for the geometry configuration where we obtained large amplitude magnetization precession. In this case, the dimensions of the ellipse are: 100 nm along the *x*-axis, 300 nm along the *y*-axis, and thickness *t*=2 nm. The advantage to use a larger thickness (in the structure by Liu *et al.* [49] it was 1.5 nm) consists in a better understanding of the STT effect, being the perpendicular anisotropy and the *i*-DMI negligible [31, 166, 115]. Particularly, we identified a configuration which permits to excite a quasi-uniform mode and to achieve promising results for the injection locking phenomenon driven by a "weak" microwave STT and a fixed bias j_{HM}. The used physical parameters are: M_S=1000x10^3 A/m, A=2.0x10^{-11} J/m, α=0.015, θ_{SH} =-0.15, and η =0.66.

Fig. 3.5(a) shows the oscillation frequency as a function of j_{HM} related to the oscillation of the *y*-component of the free layer magnetization for two different field amplitudes H_{ext}=30 and 40 mT (J_{MTJ}=0 A/cm^2). The

external field is applied with an IP angle tilted ϕ=30° with respect to the *x*-axis of the ellipse. For this thickness, the critical current densities are of the order of 10^8 A/cm^2 and are almost independent of the field amplitude (at least for the simulated values 20-50 mT).

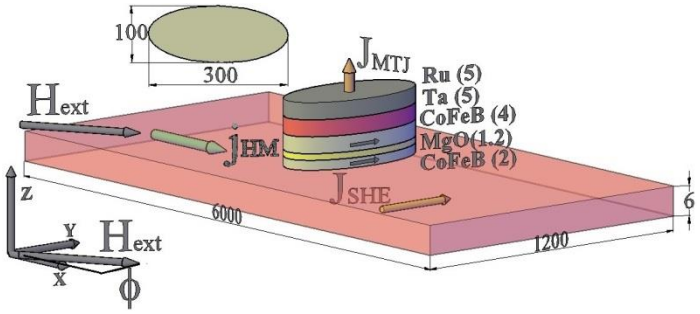

Fig. 3.4: schematic representation of the three terminal MTJ device.

As the field amplitude increases, a decrease of the current region where coherent magnetization dynamics is observed (e.g. at H_{ext}=40 and 30 mT the current range are between -1.65 and -1.95x10^{8}A/cm^2 and between -1.38 and -1.97x10^8 A/cm^2, respectively).

As expected, the oscillation frequency increases with the amplitude of the external field and its value at the critical current is 3.75 GHz for H_{ext}=30 mT and 4.60 GHz for H_{ext}=40 mT. The oscillation frequency exhibits a slightly red-shift as function of j_{HM}, indicating the presence of an IP oscillation axis, as also confirmed by the temporal evolution of the magnetization. Fig. 3.5(b) shows $<m_x>$, $<m_y>$, $<m_z>$ (dashed, solid, and dotted line respectively) for j_{HM}=-2.13x10^8 A/cm^2 and H_{ext}=30 mT for a time of 1 ns. In this case, a large amplitude of the oscillation mode in the *x*-*y* plane is shown. The spatial configuration of the magnetization snapshots are displayed in Fig. 3.5(c) (red positive and blue negative *y*-component of the magnetization, related to the numbers 1-6 as displayed in Fig. 3.5(b). Quasi-uniform magnetization dynamic is observed, with the magnetization oscillating of 180° back and forth (compare snapshot 1 and 4). In other words, the *y*-component of the magnetization rotates firstly clockwise (points 1-4) and then counter-clockwise (points 4-6).

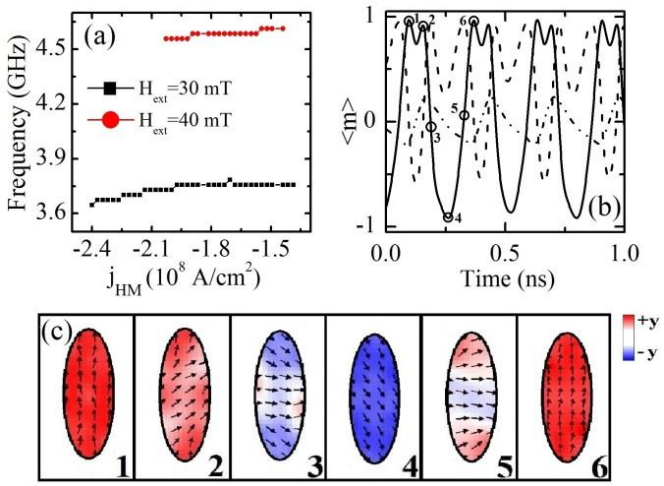

Fig. 3.5: (a) oscillation frequency of the magnetization as a function of the j_{HM} for H_{ext}=40 mT (top curve) and H_{ext}=30 mT (bottom curve) when the J_{MTJ} is zero. (b) Temporal evolution of the three normalized components of the magnetization $<m_x>$ (dashed curve), $<m_y>$ (solid curve), $<m_z>$ (dotted curve) during 1 ns of the magnetization oscillations, for j_{HM} =-2.13x10^8 A/cm^2, H_{ext}=30 mT. (c) Snapshots of the magnetization during an oscillation period in the time instants reported in Fig. 3.5(b). The color scale refers to the *y*-component of the magnetization (red positive, blue negative). The arrows indicate the magnetization direction.

Fig. 3.6(a) shows the oscillation frequency of the main excited mode for a fixed j_{HM}=-2.13x10^8 A/cm^2 as function of a bias J_{MTJ}. For positive J_{MTJ}, the oscillation frequency exhibits small variation near 3.75 GHz, while a large frequency tunability around 100 MHz/(10^6 A/cm^2) for negative J_{MTJ} is observed. This result can be explained in the following way. A positive J_{MTJ} acts as an additional positive damping, in fact, for J_{MTJ} larger than 7x10^6 A/cm^2, the microwave emission is switched off. On the contrary, a negative J_{MTJ} acts as a negative damping, showing a significant role in the oscillator frequency [26]. This behavior is different from the one observed experimentally [49], where a linear tunability of the oscillation frequency on current was found with both signs of the $J_{MTJ.}$ Indeed, in that particular framework, the J_{MTJ} was used to modify the perpendicular anisotropy, whereas in this case the anisotropy contribution is negligible. Fig. 3.6(b) shows the Fourier spectra for different values of the J_{MTJ}. In agreement with

the experimental data, it can be observed that the amplitude of the peak increases with increasing the negative value of the current.

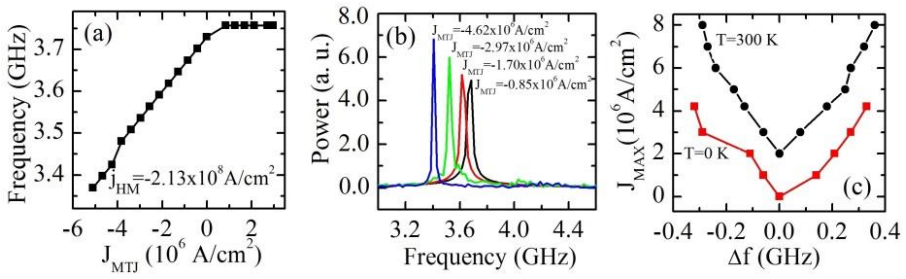

Fig. 3.6: (a) oscillation frequency for fixed H_{ext}=30 mT and j_{HM} =-2.13 x 10^8 A/cm^2 as function of the bias J_{MTJ}. (b) Fourier spectra for different values of the J_{MTJ}. (c) Arnold tongues showing the locking regions as function of J_{MAX} for T=0 K (lower curve) and T=300 K (upper curve) at j_{HM}=-2.13 x 10^8 A/cm^2.

One of the main properties of STNOs is the possibility to control the output frequency of the self-oscillation via the injection locking phenomenon [171, 172, 173]. For IP magnetized free layer, the injection locking has been observed at the 2nd-harmonic (in our case the frequency of the *y*-component of the magnetization) [174]. In general, the microwave currents were applied to the same terminal of the bias current [175]. Here, the magnetization precession is driven by the j_{HM}, while the injection locking is due to a microwave current density $j_{MTJrf} = J_{MAX}\text{sen}(2\pi f_{rf} t)$ applied via the third terminal (J_{MAX} and f_{rf} are the amplitude and the microwave frequency). In other words, this system permits to study the non-autonomous behavior of an STNO by separating electrically the biasing current from the microwave source. We fixed j_{HM}=-2.13x10^8 A/cm^2 and H_{ext}=30 mT, which corresponds to an oscillation frequency of 3.75 GHz. The locking properties have been studied for a j_{MTJrf} with amplitude J_{MAX} from 1 to 4.2x10^6 A/cm^2 at T=0 K and up to 8x10^6 A/cm^2 for T=300 K and a microwave frequency from 3.0 GHz to 8.0 GHz. Fig. 3.6(c) summarizes the locking range Δ_L as function of J_{MAX}, without and with the thermal fluctuations (T=300 K) [176, 177]. For example, at J_{MAX}=2x10^6 A/cm^2, the locking range is Δ_L=320 MHz, from 3.61 to 3.93 GHz. For current densities

up to 4.2x10^6 A/cm^2 the response is qualitatively the same, the Δ_L increases linearly with J_{MAX}. The presence of thermal fluctuations imposes a larger J_{MAX} to reach the same locking region Δ_L. No qualitative differences are observed by changing -0.1< θ_{SH} <-0.2 and 0.5< η <0.7, and by considering different MTJ cross sections of 310x100 nm^2 and 290x100 nm^2. Our results predict locking regions comparable or even larger than the experimental ones for microwave current densities of the same order [26, 171, 174]. In the synchronization region, where the resistance R oscillates at the same frequency ω_S of the microwave source, the signal can be written as $R=R_{m,S}+\Delta R_S \sin(\omega_S t+\phi_S)$, being ϕ_S the intrinsic phase shift in the synchronized state [176]. The output voltage v_{out} over the MTJ is given by:

$$\begin{aligned} v_{out} &= \left(R_{m,S}+\Delta R_S \sin(\omega_S t+\phi_S)\right) I_{MAX}\sin(\omega_S t) = \\ &= R_{m,S} I_{MAX}\,\mathrm{sen}(\omega_S t) + \frac{\Delta R_S I_{MAX}}{2}(\cos(\phi_S)-\cos(2\omega_S t+\phi_S)) \end{aligned} \quad (3.3)$$

where $I_{MAX}=SJ_{MAX}$. Together with the microwave signals at $2\omega_S$ and ω_S that can be used for the design of microwave oscillators, a dc component $0.5\Delta R_S I_{MAX}\cos\phi_S$ is also observed (as it will be described ahead in the paragraph 3.4).

Now, we focus on MTJs with different cross sections (MTJ$_1$, MTJ$_2$, and MTJ$_3$) with in plane axes 310 and 100 nm, 300 and 100 nm (same studied above), 290 and 100 nm, respectively. Fig. 3.7(a) shows a sketch of the proposed synchronization scheme for the three MTJs, but we stress the fact that this system is highly scalable and it can be extended to an array of *N*-three terminal systems.

The dependence of the oscillation frequency on j_{HM} in MTJ$_1$ and MTJ$_3$ is similar to the one related to the MTJ$_2$ (not shown). For a fixed j_{HM}, the locking range of the three MTJs is of the same order, but centered over a different oscillation frequency. For example, at j_{HM}=-2.13x10^8 A/cm^2 and J_{MAX}=2.0x10^6 A/cm^2, we achieved for MTJ$_1$ a magnetization precessional

frequency f_1=3.62 GHz and Δ_{L1}=390 MHz, for MTJ_2 f_2=3.75 GHz and Δ_{L2}=320 MHz, and for MTJ_3 f_3=3.78 GHz and Δ_{L3}=310 MHz. As illustrated in Fig. 3.7(b), the locking ranges are overlapped for a region of 290 MHz, suggesting a possible way to synchronize parallel connected three terminal oscillators.

The magnetization precession is excited by means of the SHE in all the MTJs. The synchronization is achieved via a microwave voltage applied to the third terminal $V_{app}=V_M \sin(\omega_S t)$. The output signal can be read as the voltage over R_0. For each *i*-MTJ, the conductance G_i is given by $G_i=G_{m,i}+\Delta G_i \sin(\omega_i t+\phi_i)$ where $G_{m,i}$ is the average conductance when the magnetization precession is excited, ΔG_i, ω_i and ϕ_i are, respectively, the amplitude, the frequency, and the intrinsic phase shift [176] of the oscillation generated in the *i*-MTJ. For *N*-synchronized MTJs at the frequency ω_S the total conductivity is given by $G_T=\sum_{i=1...N} G_{<M>,i}+\sum_{i=1...N}\Delta G_i \sin(\omega_S t+\phi_i)$. The electrical circuit is completed by adding two filters with the aim to use the synchronization scheme to enhance the output microwave power at $2\omega_S$. In the case of pass-band filters, Z_0 and Z_1 are composed by a capacitor and an inductor connected in series, where $L_0C_0=\frac{1}{4\omega_S^2}$ and $L_1C_1=\frac{1}{\omega_S^2}$ respectively. In this way, the output voltage over R_0 is given by:

$$v_{out}=R_0 i_0=\frac{R_0 V_M}{2}\sum_{i=1...N}\Delta G_i \cos(2\omega_S t+\phi_i) \qquad (3.4)$$

When ϕ_i values are the same (or within a range smaller than 10 degree), v_0 can be approximated to the sum of the signals from the MTJs as $v_0 \approx 0.5 R_0 V_M \cos(2\omega_S t+\phi_S)\sum_{i=1...N}\Delta G_i$. Eq. (3.4) points out how the proposed synchronization scheme can give rise to an improvement of the dynamical properties (for example power) if used as oscillator.

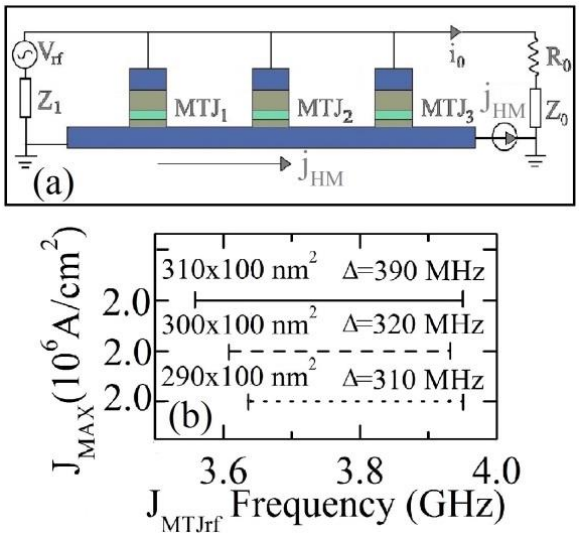

Fig. 3.7: (a) schematic representation of the proposed highly scalable synchronization scheme. (b) Locking ranges as a function of the cross-section dimensions for J_{MAX}=2.0 x 10^6 A/cm^2 and j_{HM} =-2.13 x 10^8 A/cm^2.

In summary, we have micromagnetically studied the dynamical behavior of a three terminal MTJs driven by the SOT and the STT. We have found that the control of the STT and the SOT via electrically separated terminals opens promising perspective from a technological point of view in the design of next generation of spintronic oscillators, overcoming the limit of the output power by means of an innovative highly scalable synchronization scheme.

3.3.2 Intrinsic synchronization of an array of spin-torque oscillators driven by the spin-Hall effect

Synchronization of more STNOs, by means of phase locking, has led to an increase of the output power and a reduction of the linewidth (see subparagraph 3.2.2). Since the initial demonstration, the advances in the STNOs synchronization are going ahead slowly, considering that only synchronization of three high frequency nano-contacts STNOs or of four vortex oscillators has been measured so far [152, 178].

Here [179], we have performed micromagnetic simulations of a Platinum (Pt)\Permalloy (Py≡$Ni_{80}Fe_{20}$) bilayer, where the magnetization

self-oscillations are driven by the SHE. The main result concerns the excitation of a uniform mode, spatially distributed in the whole ferromagnetic layer, for a certain range of current and external field. This outcome is in qualitative agreement with recent experimental evidences [141] and opens perspectives for the construction of an array of intrinsically synchronized conventional STNOs, which share the ferromagnet of the bilayer as free layer. This study has been completed by the investigation of the effect of the Oersted field on the magnetization dynamics and its characterization using a joint time frequency analysis [180, 181, 182].

Our research has been based on the numerical solution of Eq. (1.48). The magnetic parameters used for the micromagnetic study are: A=2.0x10^{-11} J/m, M_S=650x10^3 A/m [141, 183] α=0.02 and θ_{SH}=0.08 [37].

Fig. 3.8 illustrates the studied device whose IP dimensions are *lexw*=2000x200 nm^2 and the thicknesses of Py, t_{FE} , and Pt, t_{HM} , are equal to 5 nm. A cartesian coordinate system is introduced as depicted in the figure. The current j_{HM} flows in the x-direction, whereas H_{ext} is applied along the y-direction. The computation of the spatial distribution of the current density shows that the current flows mostly in the Pt layer (we have considered conductivities of 5.1x10^6 $(\Omega m)^{-1}$ and 2.2x10^6 $(\Omega m)^{-1}$ for Pt and Py, respectively) [141, 184], which makes the Rashba effect negligible.

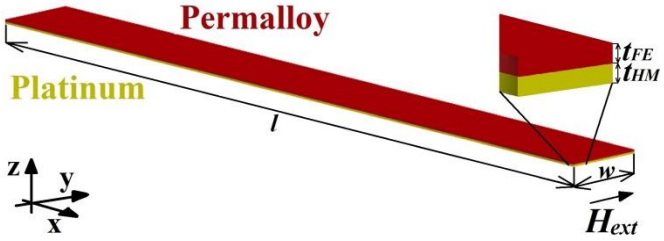

Fig. 3.8: schematic representation of the FM/HM bi-layered device. (Inset) Detailed sketch of the bylayer structure showing the thicknesses of the layers, the direction of the current density j_{HM} and the applied external magnetic field H_{ext}.

Fig. 3.9 shows the Fourier transform of the x-component of the self-oscillating magnetization, when H_{ext}=80 mT (Fig. 3.9(a)) and 90 mT (Fig. 3.9(b)), respectively, whereas j_{HM} is swept from -0.90x10^8 A/cm^2 to -1.20x10^8 A/cm^2. For a magnitude of $|j_{HM}|$=0.90x10^8 A/cm^2, no persistent

precession is excited. Results for H_{ext}=80 mT indicate the excitation of a single mode, whose frequency increases with higher values of j_{HM}. In the case of H_{ext}=80 mT, for $|j_{HM}|$=0.90x10^8 A/cm^2 only an excited mode is observed with a frequency peak P1, whereas, for $|j_{HM}|$=1.00x10^8 A/cm^2, two close frequency peaks P2 and P3 arise, revealing the existence of two independent modes. No relevant self-oscillations are observed for larger magnitude $|j_{HM}|$>1.00x10^8 A/cm^2.

In Fig. 3.10 the Fourier transform as a function of H_{ext} is represented for two values of the current: j_{HM}=-0.90x10^8 A/cm^2 (Fig. 3.10(a)) and -1.00x10^8 A/cm^2 (Fig. 3.10(b)), respectively. For both current density values, the frequency of the self-oscillation increases as the H_{ext} increases. In particular, we obtain the generation of a single mode for all the H_{ext} values, except for the configuration H_{ext}=90 mT and j_{HM}=-1.00x10^8 A/cm^2, where two modes are observed (same configuration previously represented in Fig. 3.9(b)).

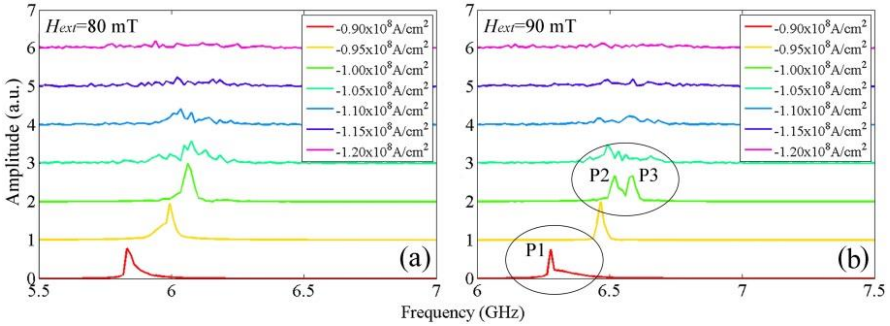

Fig. 3.9: Fourier spectra as a function of j_{HM}. (a) H_{ext}=80 mT. (b) H_{ext}=90 mT.

In order to achieve a deeper understanding of the dynamics described above, we have studied the action of the Oersted field, the spatial mode distributions (SMDs) [185], and the results of a time-frequency analysis as performed by computing the Micromagnetic Wavelet Scalogram (MWS) according to the method described in [180].

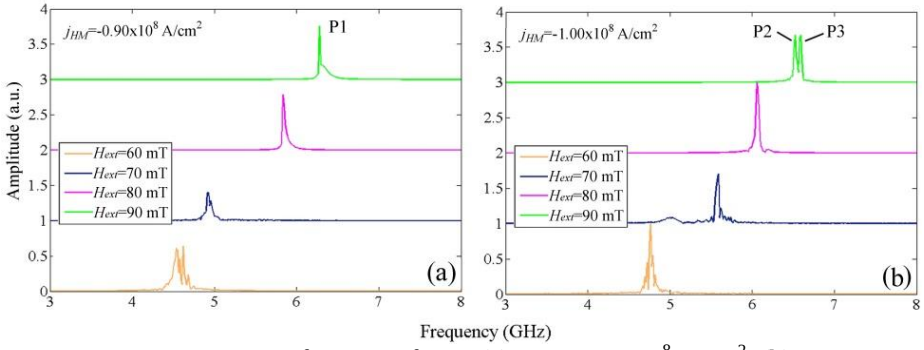

Fig. 3.10: Fourier spectra as a function of H_{ext}. (a) j_{HM}=-0.90x10^8 A/cm^2, (b) j_{HM}=-1.00x10^8 A/cm^2.

When the Oersted field is neglected, no significant changes in the frequency spectra are detected (not shown). This is an expected result, since in such kind of bi-layered device the Oersted field is uniform in the whole ferromagnet and it is oriented in the same direction of H_{ext}. On the contrary, in conventional STNOs, the Oersted field is non-uniform, exhibiting a higher amplitude near the contacts and lower towards the boundaries. When the lateral dimensions of STNOs are increased, it will exist a critical size over which the Oersted field will become predominant on the STT, leading to the nucleation of non-uniform magnetization patterns, such as vortexes.

Fig. 3.11 reports the time-frequency study based on the Wavelet Analysis (WA), as computed by means of MWS (the amplitude of the wavelet coefficient increases from white to black), whereas the SMDs are calculated using micromagnetic spectral mode decomposition mapping technique (MSMDMT) [186]. In detail, Fig. 3.11(a) represents the results for the case H_{ext}=90 mT and j_{HM}=-0.90x10^8 A/cm^2. In this scenario, when a single mode is observed (inset of Fig. 3.11(a)), it is uniform in the whole ferromagnetic cross section (its frequency is f_{P1}=6.2 GHz), and WA reveals that the mode P1 is also stationary in time. Fig. 3.11(b) refers to the configuration H_{ext}=90 mT and j_{HM}=-1.00x10^8 A/cm^2. As it can be clearly seen, the two modes P2 (f_{P2}=6.4 GHz) and P3 (f_{P3}=6.5 GHz) are uniform (see insets in Fig. 3.11(b)) but non-stationary in time, being excited in two different time windows. In addition, no differences in both the SMDs and WA are found when the Oersted field is neglected, as well as in the

computation of the power that highlights a non-linear trend with current (not shown) [173].

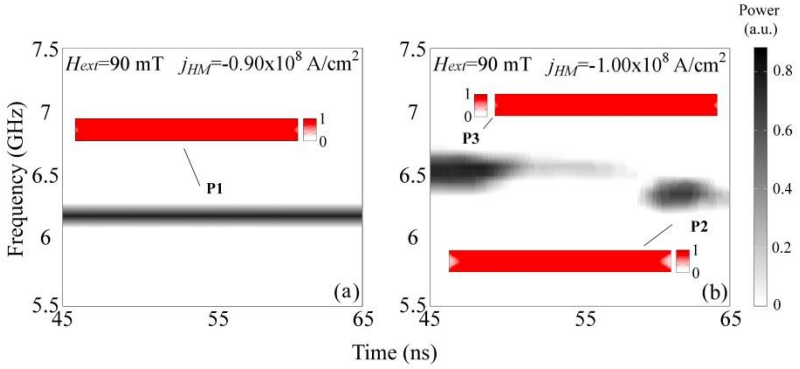

Fig. 3.11: MWS for H_{ext}=90 mT, where the power increases from white to black. (a) j_{HM}=-0.90x10^8 A/cm^2, (b) j_{HM}=-1.00x10^8 A/cm^2. Insets: SMDs related to the *x* component of the magnetization (the power increases from white to red).

In summary, our results are interesting from a technological point of view, since when a uniform mode is generated it is possible to design an embedded microwave oscillator made by an array of conventional STNOs intrinsically synchronized. The architecture would be similar to the array of three-terminal MTJs described in the previous subparagraph, where, likewise, the self-oscillations were achieved through the SHE and the output power was read via the tunnelling magnetoresistance. Differently from that geometry, the device here proposed is an array of STNOs built over the HM and sharing also the free layer (Py ferromagnet), with the advantage to attain the synchronization without applying any external microwave source.

3.4 Spin-torque diode

The *diode* is a non-linear circuital component that reacts in a different way according to the sign of the applied voltage. In a typical case, it behaves like a switch: it allows the current to flow when the applied voltage is positive (switch ON), otherwise, it hampers the charges flow (switch OFF). More in general, the diode acts as a switch-converter, like direct current to direct current (dc–dc) or alternating current to direct current (ac–dc) converter [187]. Diodes are fundamental elements of the modern

technology; just think that, without them, there wouldn't be transistors and all the digital world around them, electronic signals could not be processed, and electric current would just be used for powering motors, heaters, and light bulbs. Another particular aspect, that highlights the importance of diodes, is that 18 Nobel Prizes have been awarded in relation with the discovery and development of diodes and their technologies [187].

From the early high-frequency prototype fabricated by Hertz at the end of 1800, a lot of progress has been made in the research and development of diodes (known as also *rectifiers*), leading, nowadays, to four basic technologies: *Schottky*, *Tunnel*, *Metal-Insulator-Metal*, and *MTJ spin* diodes [187]. In particular, the Schottky technology is currently the most matured, with well-established and reliable processes [188]. The "common factor" among all the technologies is the conversion of a radio-frequency signal into a dc signal, by means of an electrical non-linear element. The "deviation from the Ohm's law" is efficiently achieved by using a potential barrier: for Schottky diodes, electrons overcome the barrier through thermal activation, while, in the other cases, they tunnel the insulator barrier. The diode effect can be applied as *mixer* in radio receivers (the diode operates like a switch and it converts a radio-frequency in an intermediate frequency as efficiently as possible), *microwave detectors* (it returns a dc signal proportional to the magnitude of the input radio-frequency signal, simply indicating its presence of absence), and in the field of *energy harvesting* (diodes play a central role in the conversion process of solar panel harvesters, wind/ocean-wave energy harvesters, thermal harvesters, kinetic energy harvesters as well as radio-frequency and electromagnetic energy harvesters) [187, 188].

3.4.1 Spin-torque diode effect in MTJs

The STD effect is a rectification effect occurring when an input microwave current $i_{MTJrf} = I_{MAX}\sin(2\pi f_{rf} t + \varphi_I)$ is passed by an MTJ with a frequency f_{rf} close to f_0. The free layer magnetization starts to oscillate

because of the STT and, consequently, the magnetoresistive effect related to the TMR converts this oscillation in a resistance oscillation $R = \Delta R_S \sin(2\pi f_{rf} t + \varphi_R)$. Coupling the input microwave current to the oscillating resistance, the output voltage is obtained $v_{out} = i_{MTJrf} \cdot R = I_{MAX} \Delta R_S \sin(2\pi f_{rf} t + \varphi_I) \sin(2\pi f_{rf} t + \varphi_R)$. Making some calculations, the following expression is reached:

$$v_{out} = \frac{1}{2} I_{MAX} \Delta R_S \left[\cos\left(\varphi_I - \varphi_R\right) - \cos\left(4\pi f_{rf} + \varphi_I + \varphi_R\right) \right] \tag{3.5}$$

Neglecting the voltage contribution at twice the angular frequency $v_2 = \frac{1}{2} I_{MAX} \Delta R_S \cos\left(4\pi f + \varphi_I + \varphi_R\right)$, only a dc component of the voltage remains:

$$V_{dc} = \frac{1}{2} I_{MAX} \Delta R_S \cos\left(\Phi_S\right) \tag{3.6}$$

where Φ_S represents the phase difference between the input current and the resulting oscillating resistance. Just to summarize, a conveniently designed MTJ having as input a microwave signal, gives back a dc signal and thus it behaves as an ac–dc converter.

The STD can be related to two different operational regimes [189]. In the case of IP MTJs, the STT gives rise to small-angle precession of the free layer magnetization around an IP axis (see Fig. 3.12(a)). For perpendicular MTJs, the STT induces large-angle oscillations of the magnetization around the OOP axis (see Fig. 3.12(b)).

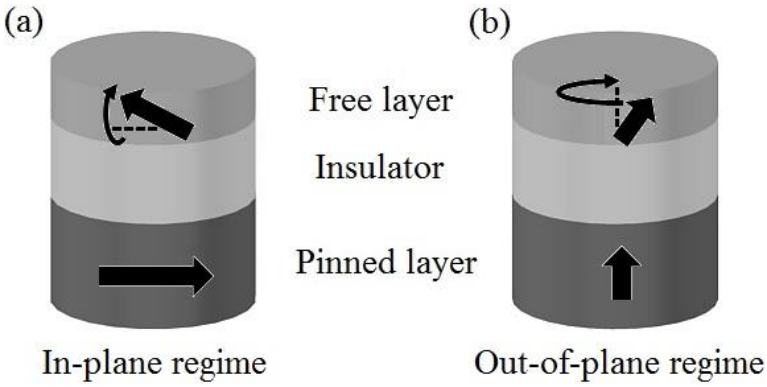

Fig. 3.12: schematic representation of an STD working in the (a) IP regime and (b) in the OOP regime.

One of the most significant parameter which can be seen as a figure of merit for the STD efficiency in converting an input power into a usable voltage is the *sensitivity*. This represents the conversion of the microwave input power P_{in} to the output dc voltage V_{dc}, which is typically expressed in V/W or mV/mW:

$$\varepsilon = \frac{V_{dc}}{P_{in}} \tag{3.7}$$

For instance, the sensitivity of a commercial Schottky diode ranges from 500 to 3800 V/W, while the highest sensitivity of STD is 75000 V/W [190].

In order to increase the sensitivity of STDs, both eternal magnetic fields and dc currents can be applied together with the microwave current. In this configuration, the device is called *biased* STD.

3.4.2 State of the art

The first experimental observation of the STD effect occurred in MgO-based MTJs in presence of an external field in 2005 [191]. Since the measured sensitivity was very low (1.4 V/W), the STD was afterwards used only to quantitatively estimate the torques (Slonczewski, field-like, and voltage-controlled torques) in MTJs and to clarify their underlying physics [27, 192]. Different strategies were used to improve the sensitivity performance, such as choosing optimized external field configurations [193, 194], using the stochastic resonance together with a bias dc current [195] as

well as using the VCMA (sensitivity of 317 V/W in unbiased scenario and of 440 V/W with external field) [30]. In 2014, Miwa *et al.* [196] measured a sensitivity of 12000 V/W in MTJs where a tilted external field and a bias current were simultaneously applied. In the same experiment, the STD exhibited a sensitivity of 630 V/W at zero bias current. Very recently, the largest sensitivity (75000 V/W) of STDs have been measured in MgO-based MTJs characterized by high perpendicular anisotropy (this avoids the use of external fields) and TMR, and where the injection locking phenomenon arises due to the application of both an dc and ac component of the current [190]. In the same study, Fang *et al.* showed a sensitivity of 900 V/W for unbiased devices. Fig. 3.13 summarizes the sensitivity achievements for STDs compared with the Schottky diode sensitivity.

As mentioned above, diodes have a fundamental role in the field of energy harvesting. In this concern, unbiased MTJ spin-diodes (no need of external inputs, meaning zero input power) could represent the basic brittle to develop the next generation of diodes.

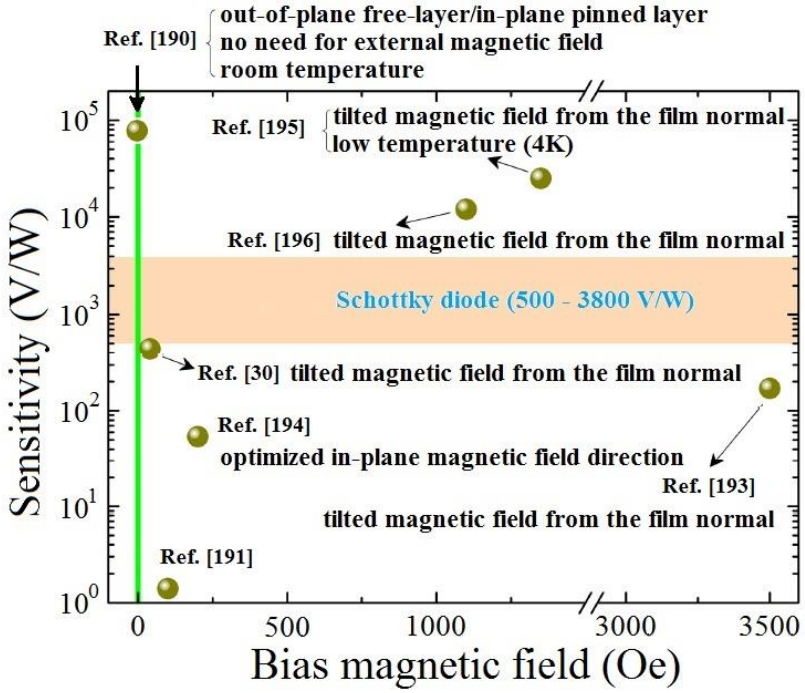

Fig. 3.13: comparison of STD sensitivities with the one of the Schottky diode [190].

3.5 Results on Spin Torque Diode

3.5.1 Influence of the Dzyaloshinskii-Moriya interaction on the spin-torque diode effect

In three terminal MTJs (see subparagraph 1.3.4), we can use the additional degree of freedom regarding the SHE (see subparagraph 1.3.1) to control the STD response. We have performed a numerical study based on the solution of Eq. (1.48) of the ferromagnetic resonance (FMR) response in three terminal MTJs [197]. We have studied a system similar to the experimental one reported by Liu *et al.* [49]. The MTJ stack is made by (CoFeB(1)/MgO(1.2)/CoFeB(4)/Ta(5)/Ru(5) (thicknesses in nm)), milled over a Tantalum (Ta) strip (6000 nm x 1200 nm x 6 nm). We introduce a Cartesian coordinate system where the *x*-axis is positioned along the larger dimension of the Ta strip, the *y*-and *z*-axes are consequently oriented along the other IP direction and along the thickness of the Ta strip. The MTJ has an elliptical cross section 180x50 nm^2 with the larger dimension oriented in the *y*-direction. The ultra-thin CoFeB(1) acts as free layer (M_S=1x10^6 A/m) and because of the very low thickness, the IPA is large enough (k_u=7x10^5 J/m^3 related only to the IPA energy contribution) [100] to impose an OOP easy axis. The CoFeB(4) is the reference layer and its magnetization is IP fixed along the negative *y*-direction. We apply an external magnetic field H_{ext}=8 mT in the negative *y*-direction to balance the dipolar field from the reference layer. The magnetic parameters for the micromagnetic study are: A=2.0 x 10^{-11} J/m, α=0.021 and θ_{SH}=-0.15.

Firstly, we consider the STT effect (FMR response with no j_{HM}) for j_{MTJrf} with an amplitude J_{MAX}=0.5x10^6 A/cm^2 and sweeping f_{rf} from 3.0 GHz to 7.6 GHz. The FMR signal is computed as the difference between the maximum and the minimum value of the oscillating *y*-component of the average magnetization. Two scenarios are investigated: the first one, where the *i*-DMI (see subparagraph 1.3.3) effect is neglected (D=0.0 mJ/m^2) and the other one when the *i*-DMI is relevant (D=-1.2 mJ/m^2) [44]. Without the

i-DMI contribution, the FMR shows only one peak at 5.8 GHz, (see Fig. 3.14(a) upper curve). The insets near the peak of Fig. 3.14(a) illustrate the SMDs for the *y*- and *z*-component of the magnetization at the FMR frequency, as computed with the MSMDMT [94]. As can be noticed, a central mode is excited for the two magnetization components. By considering the *i*-DMI (see lower curve), the FMR response displays two peaks: the first one at a frequency of 5.7 GHz (indicated with 1 in Fig. 3.14(a)) and the second one at 6.1 GHz (indicated with 2 in Fig. 3.14(a)). This FMR behavior is clearly due to the effect of the *i*-DMI, which splits the FMR mode in two, as also observed in the SMDs. In fact, while the SMD of the *y*-component shows a similar central mode, the SMD of the *z*-component displays the generation of two edge modes for the first peak and four edge modes for the second peak. Moreover, observing the time domain plot (not represented here), we note that for the frequency of 5.7 GHz, the TMR is in advance with respect to the injected microwave current; on the contrary, at the frequency of 6.1 GHz, the TMR is lagging behind the j_{MTJrf}. The *i*-DMI influences only the *z*-component because of the edge non-uniformities induced by the dipolar field.

Fig. 3.14(b) represents the FMR responses for a microwave current of J_{MAX}=0.1x10^6 A/cm^2. The FMR frequency increases, either without DMI (top curve), reaching 6.1 GHz, or with *i*-DMI (bottom curve), attaining 6.2 GHz and, additionally, both the FMR curves have a single peak. The evidence of only one frequency peak, even considering the *i*-DMI, is ascribed to the use of a weak microwave current, which keeps the FMR response in a linear regime. Also in this case, the SMD of the magnetization *z*-component shows an edge mode. In addition, the FMR frequency changes (value and shape) with J_{MAX} because a higher amplitude of the microwave current generates non-linear dynamics [166, 198]. As demonstrated in [27] (see Fig. 3(a)), this non-uniform regime can be observed by the presence of an asymmetric FMR spectrum.

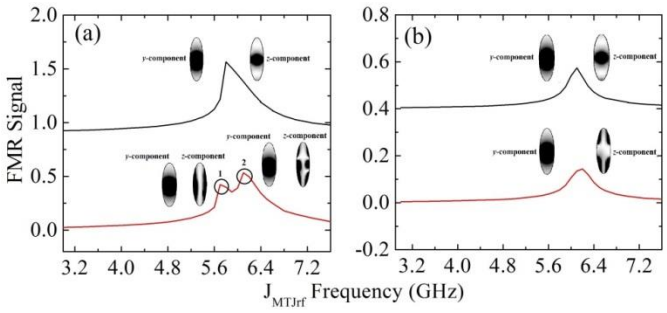

Fig. 3.14: FMR responses for j_{HM}=0 A/cm^2. a) J_{MAX}=0.5x10^6 A/cm^2 without *i*-DMI (top curve) and with *i*-DMI (bottom curve); b) J_{MAX}=0.1x10^6 A/cm^2 with no *i*-DMI (upper curve) and with *i*-DMI (lower curve). The insets represent the SMDs for the *y*- and *z*-components of the magnetization.

Fig. 3.15 shows the FMR response when a bias j_{HM}=-1.50x10^7 A/cm^2 flows in the Ta strip with (upper curve) and without (lower curve) the *i*-DMI contribution. A microwave current with J_{MAX}=0.5x10^6 A/cm^2 is injected in the MTJ stack. The top curve shows a similar behavior with respect to the corresponding curve without the IP current (Fig. 3.14(a)); in fact, a main central mode is visible in the SMDs for both *y*- and *z*-component of the magnetization. A similar behavior is also obtained in presence of the *i*-DMI: two FMR peaks are visible and the SMDs have a configuration similar to the one previously investigated (see for comparison the SMDs in Fig. 3.14(a) lower curve). Hence, the FMR behavior is not affected by a sub-critical j_{HM}, and the *i*-DMI effect concerns again the splitting of the main mode.

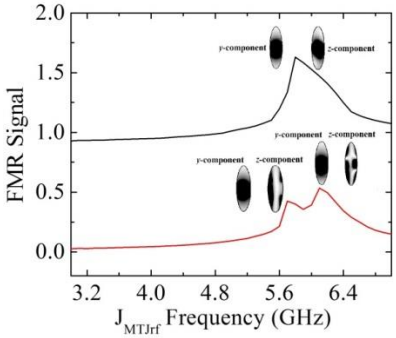

Fig. 3.15: FMR responses for a sub-critical j_{HM}=-1.50x10^7 A/cm^2 and a J_{MAX}=0.5x10^6 A/cm^2 without *i*-DMI (top curve) and with *i*-DMI (bottom curve). The insets represent the SMDs for the *y*- and *z*- components of the magnetization.

The FMR behavior is different when the j_{HM} is increased. Fig. 3.16(a) shows the computed FMR with (upper curve) and without (lower curve) *i*-DMI, when both the j_{HM}=-1.40x10^8 A/cm^2 (this value is very close to the switching one, which leads the free layer from OOP to IP) and the microwave current with amplitude J_{MAX}=0.5x10^6 A/cm^2 are applied. Without the *i*-DMI, the increase of j_{HM} does not change the FMR qualitatively, but it induces a reduction of the FMR frequency, from 5.8 GHz (Fig. 3.16(a)) to 4.8 GHz. Whereas, taking into account the *i*-DMI, a decrease of the FMR frequency and a low power peak at higher frequency are observed. Furthermore, the SMDs of the lower frequency peak show that the main excited mode is shifted from the central position. Thus, with a j_{HM} large enough (that means a relevant SHE contribution), the *i*-DMI moves the SMD of the main central mode towards the left side of the sample. Changing the sign of *D*, the central mode moves to the right side (not shown). Fig. 3.16(b) displays the FMR for j_{HM}=-1.40x10^8 A/cm^2 and J_{MAX}=0.1x10^6 A/cm^2. In this case, while the FMRs with and without the *i*-DMI are very similar (top and bottom curves respectively), a small displacement of the central mode is observed in the resonance frequency SMDs including the *i*-DMI.

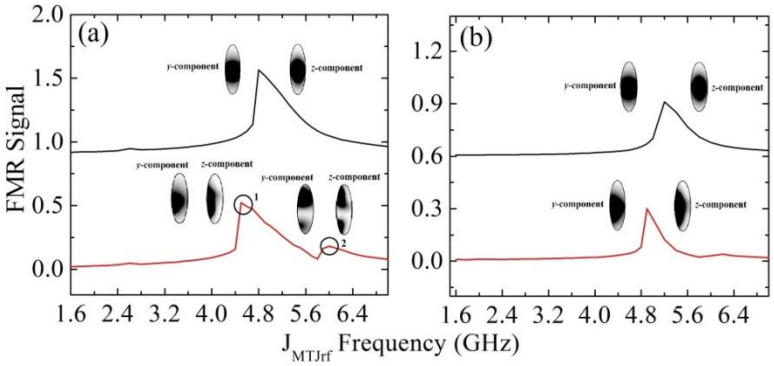

Fig. 3.16: FMR responses for j_{HM}=-1.40x10^8 A/cm^2. a) J_{MAX}=0.5x10^6 A/cm^2 without *i*-DMI (top curve) and with *i*-DMI (bottom curve); b) J_{MAX}=0.1x10^6 A/cm^2 with no *i*-DMI (upper curve) and with *i*-DMI (lower curve). The insets represent the SMDs for the *y*- and *z*-components of the magnetization.

In summary, the effect of the *i*-DMI on the FMR has been analyzed in both cases with and without the IP Ta current. We have observed that, regardless of the j_{HM}, the effect of the *i*-DMI is to break the symmetry of the main central excited mode. However, the way of the symmetry breaking has been dependent on the Ta current. If j_{HM} is negligible or it assumes a sub-critical value, we have observed that *i*-DMI breaks the symmetry of the main central mode in two (or more, as function of the peak) different edge modes. For larger j_{HM}, the *i*-DMI contribution is not so large to divide the main excited mode and its effect is the displacement of the main central mode towards a lateral position only.

4. SPIN-TORQUE OSCILLATOR AND DIODE BASED ON SKYRMION

This chapter discusses the results obtained on microwave oscillators and detectors based on the non-uniform state of the magnetization, which is the skyrmion. Paragraph 4.1 deals with the use of skyrmions in STNOs, while paragraph 4.2 describes the STD based on skyrmions and the implications in the energy harvesting field.

4.1 Topological, non-topological and instanton droplets driven by STT in materials with perpendicular magnetic anisotropy and DMI

Solitons are self-localized wave packets that can be observed in media characterized by non-linear and dispersive constitutive laws and can be also classified on the basis of their topology, i.e. the skyrmion number (see Eq. (1.49)). The study of magnetic solitons [52, 199], has been reinforced by the experimental evidence that the STT (see subparagraph 1.2.4) can nucleate both static and dynamic solitons from a uniform state or

manipulate strongly non-uniform magnetic configurations. In particular, static solitons can be achieved in either IP (vortexes, antivortexes, and DWs) or OOP devices (bubbles, skyrmions, and DWs) and they can behave like particles, e.g. vortex [140] and skyrmion [71] can rotate around a nanocontact in point contact geometries (oscillators), skyrmions and DWs can be shifted in a track (racetrack memory) [47, 65, 120, 111, 115] (see paragraphs 2.3 and 2.4). On the other hand, dynamical solitons, that are unstable in dissipative magnetic materials, can be sustained by the STT and used as source of microwave emissions (self-oscillations) in nanoscale oscillators [53, 200, 201, 202]. In the recent literature, only few works have been devoted to the identification and study of topological modes [70]. In detail, the excitation of a topological mode was predicted by Zhou *et al.* [70] and used to explain recent experimental observations in CoNi [69].

Here [203], the adjectives "non-topological" and "topological" are used to identify a mode with a skyrmion number zero (S=0) and one (S=1), respectively. The numerical results are achieved by numerically solving Eq. (1.34).

Fig. 4.1 shows a sketch of the studied device, consisting of a spin-valve of Pt(5 nm)/Co(0.6 nm)/Cu (4 nm)/CoPt(4 nm). The ultrathin Co layer acts as free layer (square cross section of 400×400 nm^2 and thickness of 0.6 nm), while the CoPt acts as fixed layer or polarizer and it is shaped as a circular point contact (diameter d_c=70 nm) in order to locally inject the current into the free layer. Both free layer and polarizer have an OOP magnetic state at zero bias field. A Cartesian coordinate system, with the x- and y-axes oriented along the IP directions of the device and the z-axis along its thickness, has been introduced.

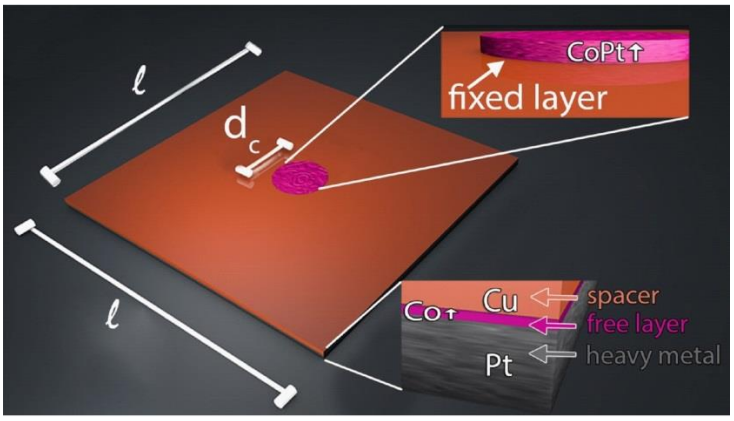

Fig. 4.1: spin valve with a point contact geometry, where the Co free layer is coupled to the Pt underlayer. For the sake of clarity, an enlarged view of the nanocontact (fixed layer) and the diameter d_c of the nanocontact are illustrated, together with the dimensions $l \times l$ of the square cross section.

Fig. 4.2(a) summarizes the phase diagram of the magnetization as a function of the current density (swept back and forth) and the *i*-DMI parameter *D*. For the sake of simplicity, in the following, the current density $J<0$ (the current flows from the free layer to the fixed layer) is given in modulus. Five different states can be identified, two static states: uniform state along the *z*-direction (FM) and static skyrmion (SS), and three dynamical states, NTD [53, 202], TD and ID. The *i*-DMI regions described above are separated by straight horizontal lines, as obtained with a *D* resolution of 0.05 mJ/m^2, whereas the dotted line for D=3.7 mJ/m^2 marks the *i*-DMI value above which the skyrmion, once nucleated, is stable without current. In some current regions, the FM state is overlapped with the three dynamical states, since all the modes deal with a sub-critical Hopf bifurcation [204] (finite power at the threshold, current density hysteresis, the mode is switched off at a current density smaller than the excitation value, and the oscillation axis is different from the equilibrium configuration in the FM state). Starting from the FM state, the modes are excited at J=7.0×10^7 A/cm^2 (D<3.0 mJ/m^2) independently of the *i*-DMI, while the switch-off current density depends on the *i*-DMI. This is due to the dependence of the *i*-DMI field (see Eq. (1.46)) on the spatial derivative of

the magnetization that does not influence the excitation current in the uniform state. The SS state is achieved for $1.6<D\leq 3.0$ mJ/m^2 from the TD state with a reversible transition, while a static skyrmion, once excited, is stable with no current for $D\geq 3.7$ mJ/m^2. From the theory developed in [48], the critical *i*-DMI parameter which stabilizes the skyrmion state is given by $D_c = 4\frac{\sqrt{Ak_{eff}}}{\pi} = 4.4$ mJ/m^2, where $k_{eff} = k_u - \frac{1}{2}\mu_0 M_s^2$. As expected and already well discussed in [48], the analytical value is larger than the micromagnetic one because the D_c expression has been derived within a 1D model.

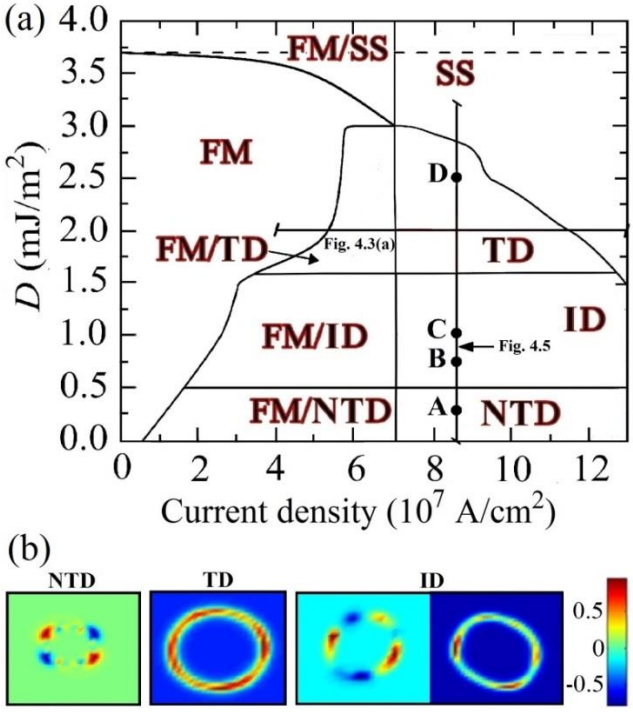

Fig. 4.2: (a) stability phase diagram of the magnetization ground-state as a function of the modulus of the current density and of *D* at zero external magnetic field. Letters A, B, C and D are linked to Fig. 4.4. The meaning of the symbols in the phase diagram are as follows. FM: ferromagnetic; SS: static skyrmion; TD: topological droplet; NTD: non-topological droplet, ID: instanton droplet. (b) Spatial distribution of the topological density (a color scale is represented, red +1, blue -1) for the three dynamical states NTD, TD, and ID at *i*-DMI values of 0.00, 2.50, and 1.25 mJ/m^2, respectively.

We have also performed a systematic study of the stability phase diagram as a function of different physical parameters, namely k_u, the A and α. We found that, in order to achieve magnetization dynamics at zero external magnetic field, a high perpendicular anisotropy (k_u>0.95 MJ/m^3) is needed, whose values have been already measured in similar devices [34].

The NTD mode is excited for $D\leq$0.5 mJ/m^2 and its dynamics concerns a 360^o IP rotation of domain wall spins [53, 200, 202]. Unlike previous studies, where the NTD is characterized by two or four regions [53, 201] of opposite topological density, here the NTD exhibits a more complex behavior as can be also seen from a snapshot of the topological density in Fig. 4.2(b). Close to D=0.25 mJ/m^2, the NTD is characterized by a small shift of the droplet core together with the domain wall spins rotations. The origin of the different topological density of the NTD will be discussed ahead.

The TD is excited for 1.6<$D\leq$ 3.0 mJ/m^2. It exhibits a core breathing dynamics that is synchronized with a 360^o in phase rotation (space and time) of the domain wall spins, which can be seen as a continual change from Néel to Bloch skyrmion magnetic texture (S=-1, see a snapshot of the topological density in Fig. 4.2(b))

Fig. 4.3(a) and Fig. 4.3(b) show the frequency-current and the output power vs current for D=2.0 mJ/m^2 as computed from simulations, respectively. The oscillation frequency of the TD (at values smaller than the FMR frequency, about 37 GHz) decreases with increasing current [201]. The oscillation power computed from the z-component of the magnetization (perpendicular polarizer) shows a finite value at the excitation current when the initial state is the FM, as expected for a sub-critical Hopf bifurcation, whereas it tends to zero as soon as the SS state is approached. These results show that the TD state can be seen as a reversible linear mode of the SS justifying the name of dynamical skyrmion already used in literature.

Looking at the spatial distribution of the oscillating spins of the TD modes (see Fig. 4.3(c)) for the two-dimensional profile of the TD for D=2.5

mJ/m^2 and J=8.5×10^7 A/cm^2 as computed with the micromagnetic spectral mapping technique [173, 205], it is easy to demonstrate that the dimensionless output power p_{out}, due to a variation in the GMR signal, is related to the breathing mode as:

$$p_{out} = \begin{cases} \left(1 - \frac{r_{\min}^2}{r_{\max}^2}\right) & r_{\max} \le r_c \\ \left(1 - \frac{r_{\min}^2}{r_c^2}\right) & r_{\max} > r_c \end{cases} \tag{4.1}$$

being $r_{\min}$ and $r_{\max}$ the minimum and maximum radius of the TD during the breathing and r_c the radius of the point contact (see Fig. 4.3(c)). The dimensionless output power calculated according to Eq. (4.1) shows a very good agreement with the one computed by means of micromagnetic simulations (Fig. 4.3(b)).

The TD mode described in this study, already observed in [70], is different from the ones seen in the subparagraph 2.4.1, where the breathing mode is just a transient due to the application of the spin current, in [68] where the breathing mode is a resonant state of a static skyrmion excited by a microwave field, and in [69] where no synchronization between the core breathing and domain wall spins precessions is detected.

In general, in 2D systems the topological states are represented by local minima in the free energy landscape separated by a finite energy barrier. This energy barrier is proportional to the exchange contribution in a texture where the spins are not locally parallel but resemble through a hedgehog-like spin configuration with a singular point in the middle. This magnetic structure can be called “instanton”, which in our framework is a time-dependent magnetization configuration connecting different topological states [206, 207]. In the *i*-DMI region 0.5<D≤1.6 mJ/m^2, time domain changes in the topology (skyrmion number) of the topological mode are found, in particular a configuration linkable to NTD or to TD can be observed.

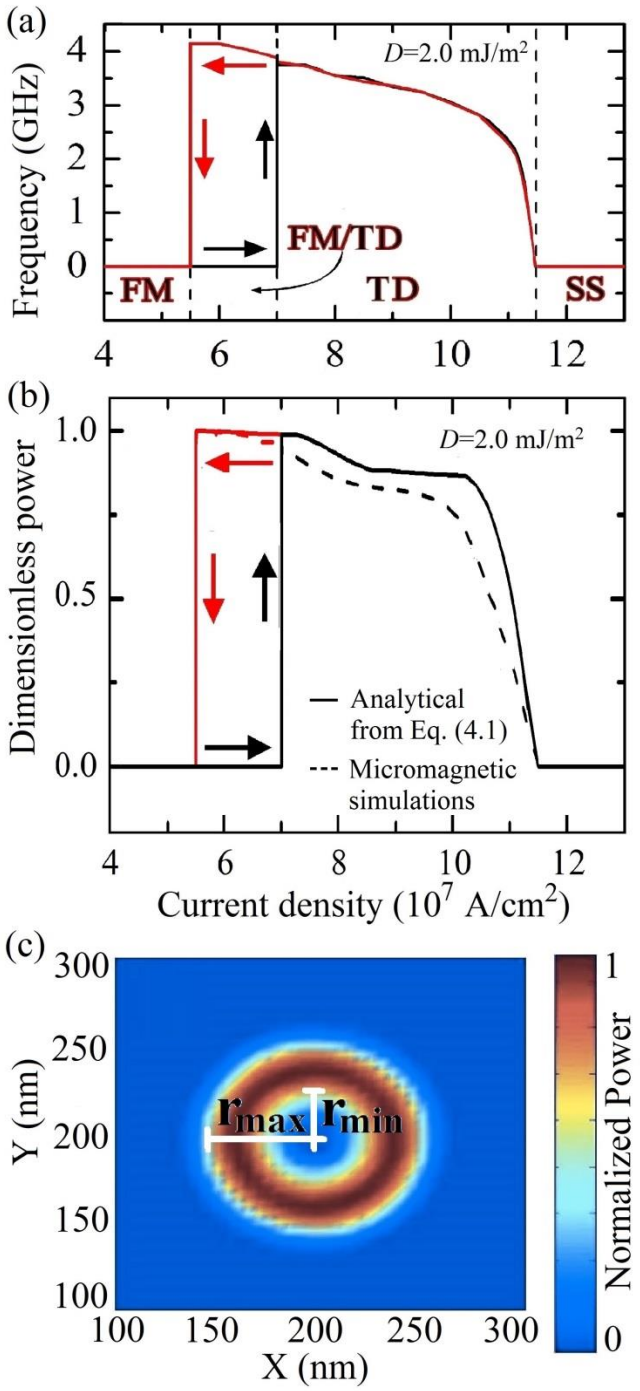

Fig. 4.3: (a) frequency-current density hysteresis loop at D=2.0 mJ/m^2: the black (red) arrows indicate the path where the initial state is FM (SS). (b) Output power as a function of current density for D=2.0 mJ/m^2. The solid line refers to the analytical computation from Eq. (4.1), while the dotted line is determined by micromagnetic calculations. The black (red) arrows indicate the path where the initial state is FM (SS). (c) Two dimensional spatial profile of the TD for D=2.5 mJ/m^2.

The first definition of instanton was classical and referred to localized finite-action solutions of the classical Euclidean field equations with finite Euclidean action [206]. Recently, an instanton dynamics has been introduced to study the quantum dynamics of vortexes in magnetic disks starting from the generalized Thiele's equation [208]. In analogy, we have defined an instanton as a time-dependent configuration connecting different topological states. In other words, in our framework the term "instanton" has been introduced with the aim to extend this important notion to low-dimensional semi-classically described magnetic systems, thus achieving the classical correspondence of the pseudoparticles theoretically found in [209]. This has been obtained by solving micromagnetically the LLGS equation (Eq. (1.4)) of motion for low-dimensional magnetic systems. Specifically, we identify with "instanton droplet" only the *i*-DMI region where the dynamics is characterized by a variation in time of the topological charge (skyrmion number) passing from TD (S=-1) to NTD (S=0) and vice versa.

The continual changes in the droplet topology generate incoherent emission of spin waves [131, 210] being the topological transition non periodic. To highlight the main characteristics of the dynamical states of the phase diagram, the Fourier spectra for different values of *i*-DMI (D=0.25, 0.75, 1.00, and 2.50 mJ/m^2) are shown in Fig. 4.4.

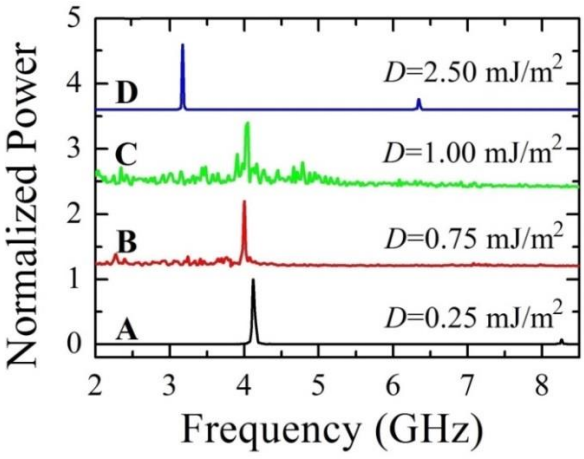

Fig. 4.4: frequency spectra as a function of the *i*-DMI, when J=8.5x10^7 A/cm^2. Capital letters A, B, C, and D are linked to the phase diagram of Fig. 4.2.

The NTD and TD are characterized by a single mode (the Fourier spectra exhibit a main frequency peak at 4.12 GHz for D=0.25 mJ/m^2 and at 3.17 GHz for D=2.5 mJ/m^2, respectively). In the ID region, the time-domain non-stationary topological transitions give rise to the excitations of incoherent spin waves leading to noisy Fourier spectra (see the spectra for D=0.75 and D=1.00 mJ/m^2). From an experimental point of view, it is possible to detect the ID region by performing microwave emission measurements.

Fig. 4.5 summarizes the oscillation frequency linked to the mode with larger power as a function of the *i*-DMI for a fixed current density of 8.5×10^7 A/cm^2, as indicated in Fig. 4.2. The transition from a dynamical region to the other one is similar to the topological transitions from skyrmion to a uniform ferromagnetic state or vice versa as described in [211]. In particular, the topological changes characterizing the instanton droplet can be seen as finite-time singularities [211] which are driven by the spin-polarized current. The inset of Fig. 4.5 shows the energy related to the continual change of the topology as a function of D, within a time window of 42 ns. The energy increases with D because more stable topological droplets are achieved.

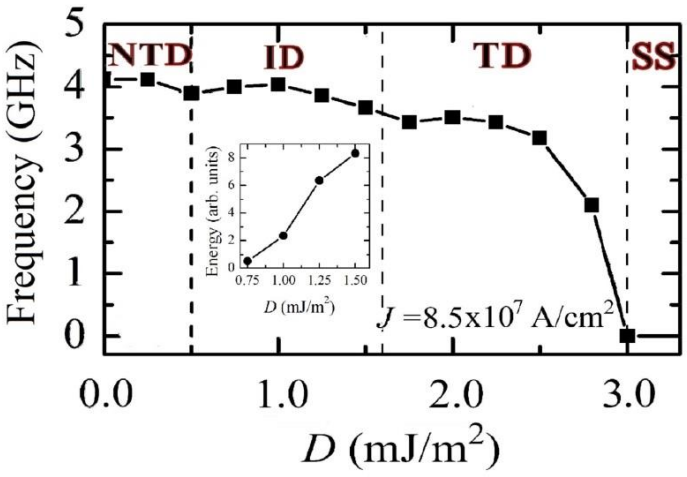

Fig. 4.5: oscillation frequency as a function of D for J=8.5×10^7 A/cm^2. The different states are indicated. The inset shows the energy related to ID transitions as a function of D for J=8.5×10^7 A/cm^2.

Finally, we have studied the mode excitation for different contact diameters. Fig. 4.6 shows the Fourier spectra of the magnetization dynamics when J=8.5×10^7 A/cm^2 and zero i-DMI for three different values of d_c. As expected, by injecting the same current density, the frequency of the domain wall rotation increases while decreasing the nanocontact diameter due to energy balance between the current input and the Gilbert damping. Moreover, for the smallest d_c, the spatial distribution of the topological density is composed of four different regions, whereas for the larger diameters a more complicated topological density distribution is obtained, including several alternated regions with positive and negative topological density. Our results show that the topological density of the NTD can be controlled by the size of the nanocontact d_c.

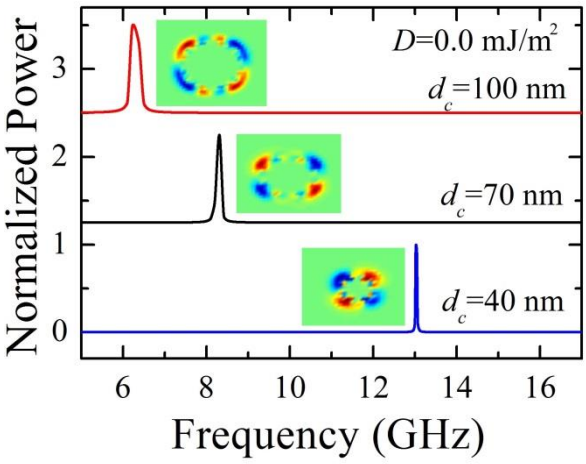

Fig. 4.6: frequency spectra as a function of the contact diameter d_c, when J=8.5x10^7 A/cm^2 and zero i-DMI, together with the spatial distribution of the topological density (red +1, blue -1) which corresponds to the frequency peak in the NTD dynamical state.

Micromagnetic simulations show qualitatively the same phase diagrams for contact size larger than 50 nm. In particular, for D=2.50 mJ/m^2, the TD state is excited in the range (3.0≤J≤ 6.5)×10^7 A/cm^2 and (7.0<J≤ 9.0)×10^7 A/cm^2 for d_c = 100 nm and d_c=70 nm, respectively. When d_c=40 nm, the TD mode is not excited, even when the spin-polarized current is increased. This is due to the fact that the small size of the nanocontact hampers the breathing mode of the droplet. However, at reduced contact

diameter sizes d_c<50 nm, to stabilize a TD, an external OOP field is necessary (not shown).

In summary, micromagnetic results point out that the additional degree of freedom of the *i*-DMI energy together with a spin-polarized current can drive transitions from either static to dynamical or dynamical to dynamical states, also implying a change in the topology during these transitions. These results indicate a route for the fundamental study of topological transitions in driven systems. Moreover, we have identified a new mode we called "instanton droplet", which is characterized by time domain transitions of the topological charge.

Finally, the breathing mode of the TD can be used as basis for the design of high power spin-transfer torque oscillators by considering a redesign of this system in an MTJ [166], where it is possible, in a phenomenological way, to link the microwave output power and the size of the breathing mode.

4.2 Skyrmion based microwave detectors and harvesting

We report the results of micromagnetic simulations of STD where a Néel skyrmion is the magnetic ground state of the free layer of an MTJ. We have considered the skyrmion based STD as response to a microwave current locally injected into the ferromagnet via a nano-contact [212].

We have studied an MTJ (see sketch in Fig. 4.7), with a circular cross section of diameter l=100 nm. The stack is composed of an iron-rich free layer, with thickness of 0.8 nm, and an MgO spacer with on top a nano-contact of CoFeB acting as current polarizer of diameter $d_c<l$. The system is designed in order that the IPA is large enough to induce an OOP easy axis (*z*-axis) in both ferromagnets [31]. Furthermore, the free layer is coupled to a Pt layer to introduce in its energy landscape the *i*-DMI (see Eq. (1.46)).

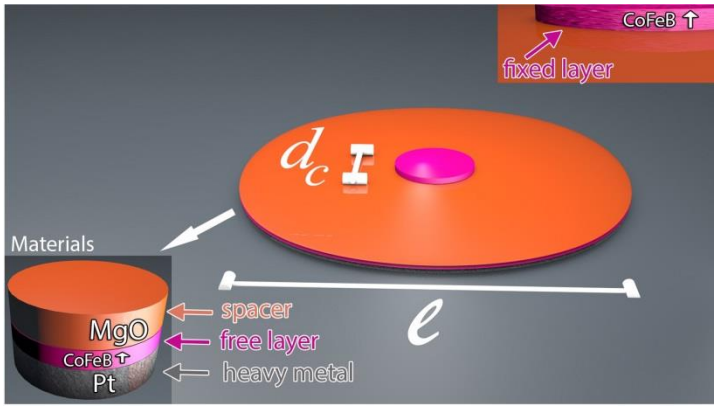

Fig. 4.7: sketch of the device under investigation. The extended CoFeB acts as free layer while the top nano-contact made by CoFeB is the current polarizer (d_c is the contact diameter, l=100 nm). The Pt layer is necessary to introduce the i-DMI.

All the results are achieved at zero external field. The main simulation parameters are: M_S=900 kA/m, A=20 pJ/m, and α =0.03. We have performed micromagnetic simulations based on Eq. (1.35) to study the stability and the dynamical response of a single Néel skyrmion as a function of k_u and of D.

The inset of Fig. 4.8(a) shows a snapshot of a skyrmion (the arrows refer to the IP component of the magnetization, while the color is linked to its OOP component - blue negative and red positive) as ground state of the free layer, where also its diameter d_{SK} is indicated (the radius is calculated as the distance from the geometrical center of the skyrmion, where m_z is -1 to the region where m_Z=0). The main panel of Fig. 4.8(a) shows the profile of m_z as computed by considering the section AA'. The negative region coincides with the skyrmion core, while the non-monotonic behavior near the edges is due to the boundary conditions in presence of the i-DMI (see Eq. (1.47)). For the nucleation of the skyrmion, we apply a localized dc spin-polarized current following the same procedure described in [65], finding that the nucleation in a time smaller than 5 ns is achieved with bias J_{MTJ}=30 MA/cm^2.

Fig. 4.8 (b) and (c) show d_{SK} as a function of D for two values of k_u=0.8 and 0.9 MJ/m^3 and as a function of k_u for D=3.0 and 3.5 mJ/m^2, respectively. In our study, we have used DMI parameters larger than the one

estimated in *state of the art* materials (>2.0 mJ/m^2 for a ferromagnetic thickness of 0.8 nm) [213, 214, 215]. However, *ab initio* computations have predicted values of D close to 3.0 mJ/m^2 for Pt/Co bilayers [216]. In addition, this choice can permit to have a comparison with previous numerical studies [68]. The fixed layer diameter d_c, which also corresponds to the nano-contact size, has been chosen to be comparable or larger than the skyrmion diameter. This aspect is important to design the skyrmion based microwave detector in order to optimize its sensitivity as it will be discussed below.

Numerically, the resistance of the device R is given by $\mathrm{R} = \mathrm{R}_P + (\mathrm{R}_{AP} - \mathrm{R}_P)(1 - < m_z >)$ being the polarizer aligned along the positive *z*-axis. Within the approximation that the direction of the magnetization changes sharply from down (-1) to up (+1) when moving across a skyrmion, the R can be estimated directly from the skyrmion diameter d_{SK} as follow:

$$\mathrm{R} = \begin{cases} \mathrm{R}_P \left(1 - \dfrac{d_{SK}^2}{d_c^2}\right) + \mathrm{R}_{AP} \dfrac{d_{SK}^2}{d_c^2}; & d_{SK} < d_c \\ \mathrm{R}_{AP}; & d_{SK} \geq d_c \end{cases} \tag{4.2}$$

for $d_{SK} < d_c$ the left (right) contribution is related to the micromagnetic cells below the nanocontact where $m_z > 0$ ($m_z < 0$).

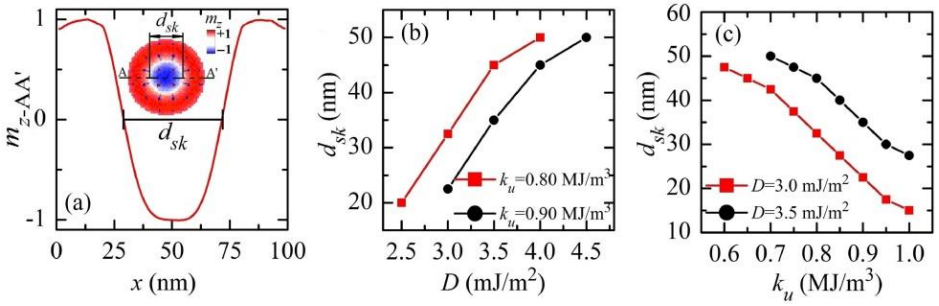

Fig. 4.8: (a) profile of the OOP component of the magnetization corresponding to the section AA', as indicated in the inset. d_{sx} represents the skyrmion diameter. Inset: example of a snapshot of a Néel skyrmion stabilized by the *i*-DMI, where the arrows indicate the IP component of the magnetization while the colors are linked to the OOP component (blue

negative, red positive). (b) and (c) Skyrmion diameter as computed by means of micromagnetic simulations (the radius is computed as the distance from the geometrical center of the skyrmion, where m_Z=-1 to the region where m_Z=0). Skyrmion diameter (b) as a function of D for k_u=0.8 and 0.9 MJ/m^3 and (c) as a function of k_u for D=3.0 and 3.5 mJ/m^2.

To characterize the dynamical response of the STD, we have also used the detection sensitivity ε (see Eq. (3.7)), where $P_{in} = 0.5 J_M^2 S^2 R$.

Fig. 4.9(a) and (b) show the STD responses as a function of the microwave frequency (d_c=40 nm) achieved for J_{MAX} =3 MA/cm^2, in (a) k_u=0.8 MJ/m^3 is maintained fixed while D=2.5, 3.0, 3.5 and 4.0 mJ/m^2, in (b) D=3.0 mJ/m^2 while k_u changes from 0.7 MJ/m^3 to 0.9 MJ/m^3. The skyrmion response is mainly characterized by the excitation of a breathing mode of its core, with a preserved radial symmetry, similarly to the fundamental mode described in literature [68, 210, 217]. The weak sinusoidal microwave current (quasi-monochromatic signal) excites the fundamental mode, being the skyrmion response in a quasi-linear regime. This mode induces a resistance oscillation of amplitude ΔR_S linked to the minimum and maximum skyrmion core diameter $d_{SK\text{-}min}$ and $d_{SK\text{-}max}$ and given by

$$\Delta \mathrm{R_S} = \begin{cases} \left(\mathrm{R}_{AP} - \mathrm{R}_P\right) \dfrac{d_{SK-\max}^2 - d_{SK-\min}^2}{d_c^2} & d_{SK-\max} < d_c \\ \left(\mathrm{R}_{AP} - \mathrm{R}_P\right)\left(1 - \dfrac{d_{SK-\min}^2}{d_c^2}\right) & d_{SK-\max} \geq d_c \end{cases} \tag{4.3}$$

$\Delta \mathrm{R_S}$ is as larger as $d_{SK-\min}^2 -> 0$ and $d_{SK-\max} -> d_c$. Moreover, as expected, the FMR frequency does not change with the contact diameter d_c (not shown), being linked to the excitation of the fundamental mode of the skyrmion.

The FMR frequencies as a function of D for different k_u are summarized in Fig. 4.9(c). This non-monotonic trend can be attributed to a different effect of the confining force (self-magnetostatic field) on the skyrmion fundamental mode. To qualitatively understand this behavior, we

refer to the concept of critical D introduced in [48]. For extended ferromagnets, when D is below D_{crit}, the confining force is negligible, whereas for D near or above D_{crit}, the confining force plays a crucial role in fixing the skyrmion size. We argue that this fact gives rise to the different slopes of the FMR frequency vs D for our system. Those arguments are confirmed by micromagnetic simulations performed for devices with diameter l=75nm and 150nm (k_u=0.80 MJ/m^3) and displayed in Fig. 4.9(d). For l=75nm, the confining force acts on the skyrmion also at small D giving rise to a monotonic FMR frequency vs D curve. On the other hand, for l=150nm the non-monotonic trend is exhibited again and the minimum moves towards D= D_{crit}=3.07 mJ/m^2, as expected.

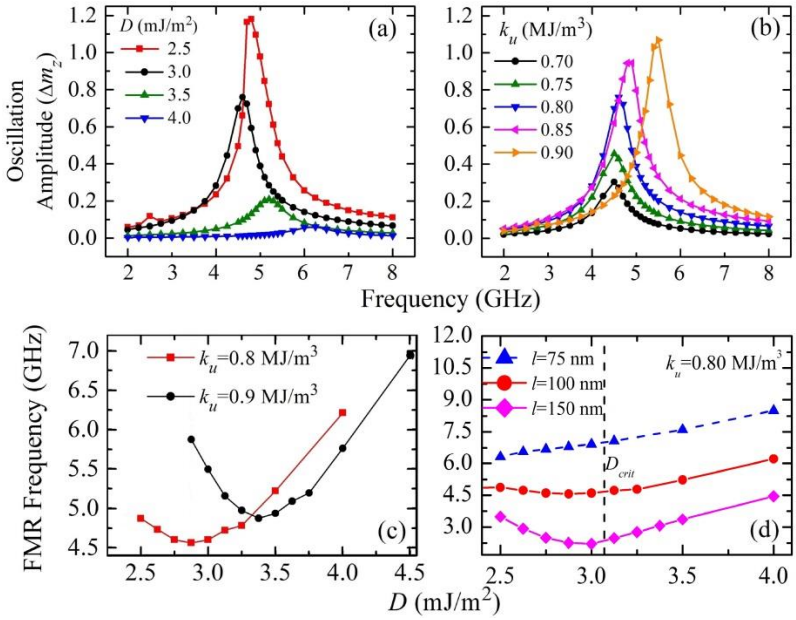

Fig. 4.9: (a) STD response as a function of D for k_u=0.8 MJ/m^3. (b) STD response as a function of k_u for D=3.0 mJ/m^2. (c) FMR frequency as a function of D for two different values of k_u as indicated in the panel. (d) FMR frequency as a function of D (k_u=0.8 MJ/m^3) for three different values of the cross section diameter l=75, 100, and 150 nm with the indication of the critical DMI parameter D_{crit}.

To compare the skyrmion-based STD to the *state of the art* MTJ-based STDs, we have performed a systematic study of the sensitivity computed at the FMR frequency as a function of the d_c (30 nm< d_c < 60 nm). All the data discussed below are obtained for k_u=0.8 MJ/m^3 and D=3.0

mJ/m^2, however qualitative similar results have been achieved for k_u=0.9 MJ/m^3 and D=2.5 and 3.5 mJ/m^2.

Fig. 4.10(a) summarizes the sensitivities computed for four different current amplitudes J_{MAX} =1-4 MA/cm^2 maintained constant at different d_c (R_{AP} =1.5 kΩ and R_P =1 kΩ) [218]. One key finding is the existence of an optimal contact size where the sensitivity exhibits a maximum value. This result can be qualitatively understood as follow. For a fixed skyrmion ground state, the change in the d_c introduces a change in the microwave power (both static resistance R and contact cross section depend on d_c). Fig. 4.10(b) displays the detection voltage and the input microwave power as a function of the contact size for J_{MAX} =1 MA/cm^2. As can be observed, both the detection voltage and the input microwave power increases as a function of d_c. Their ratio determines the optimal d_c, as reported in Fig. 4.10(a). In particular, the key condition to be fulfilled is:

$$\frac{d\varepsilon}{d(d_c)} = \frac{1}{P_{in}^2}\left(P_{in}\frac{dV_{dc}}{d(d_c)} - V_{dc}\frac{dP_{in}}{d(d_c)} \right) = 0 \qquad (4.4)$$

which should be solved numerically. The second result is the prediction, for an optimal configuration, of sensitivities of the order of 2,000 V/W, which are larger than the ones of *state of the art* unbiased MTJ-based STDs around 900 V/W [190].

Fig. 4.10(c) summarizes the sensitivities computed as a function of the d_c for different values of the microwave power. Those computations also show the existence of an optimal contact, which coincides with the maximum of the detection voltage, as summarized in Fig. 4.10(d). In fact, for the last computational framework, the Eq. (4.4) holds $\frac{d\varepsilon}{d(d_c)} = \frac{dV_{dc}}{d(d_c)} = 0.$ As can be observed, the two maxima differ of less than 5 nm (compare Fig. 4.10 (a) and Fig. 4.10 (c)).

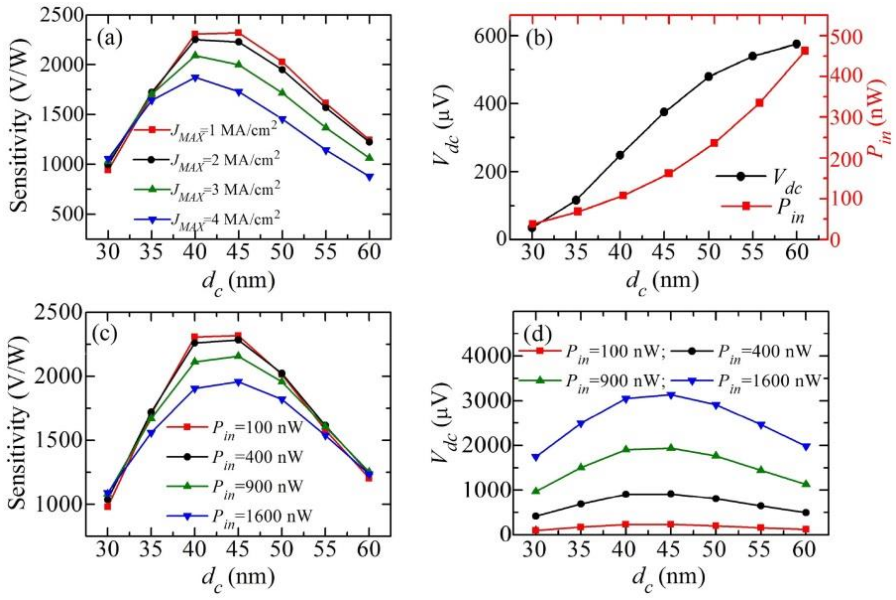

Fig. 4.10:(a) sensitivity as a function of the contact diameter for different amplitudes of the microwave current as indicated in the main panel. (b) Detection voltage and microwave power as a function of the contact diameter for J_{MAX} =1 MA/cm^2. (c) Sensitivity as a function of the contact diameter for different microwave powers as indicated in the main panel. In both (a) and (c) an optimal contact diameter corresponding to a maximum in the sensitivity can be observed. (d) Detection voltage as a function of the contact diameter for different microwave powers. All the data reported in this figure are obtained for k_u=0.8 MJ/m^3 and D=3.0 mJ/m^2.

The last part of this study investigates a possible contribution of the VCMA (see subparagraph 1.2.7) to the sensitivity of skyrmion based STDs. We have implemented this contribution as an additive field to the effective field as $H_{VCMA} = \Delta H_{VCMA} \sin(\omega t)$ applied along the OOP direction [219]. We have performed an ideal numerical experiment considering the optimal scenario of Fig. 4.10(a) (d_c=40 nm, FMR frequency $\approx$ 4.6 GHz). At J_{MAX} =0 MA/cm^2, the H_{VCMA} drives an oscillating z-component of the magnetization, whose amplitude as a function of ΔH_{VCMA}, is displayed in Fig. 4.11(a). The key difference with parametric resonance is the absence of a threshold value for the excitation of dynamics. In other words, the VCMA acts on a skyrmion state as linear excitation [219]. Fig. 4.11(b) shows the sensitivities as a function of the ΔH_{VCMA} for J_{MAX} =1 and 2 MA/cm^2. The minimum in

the sensitivity around ΔH_{VCMA}=4 mT can be explained by the change in the phase Φ_s (see Fig. 4.11(c)). While the amplitude of the ΔR_S monotonically increases with the ΔH_{VCMA}, the Φ_S is non-monotonic: firstly it decreases up to a minimum value at ΔH_{VCMA}=4 mT (Φ_S =0.66π for J_{MAX} =1 MA/cm^2) and then increases. An in-depth analysis of the micromagnetic configurations show that at low ΔH_{VCMA} both $d_{SK-\min}$ and $d_{SK-\max}$ change ($d_{SK-\min}$ decreases and $d_{SK-\max}$ increases). On the other hand, as the ΔH_{VCMA} increases, it exists a critical value at which the $d_{SK-\max}$ saturates to d_c, while $d_{SK-\min}$ will continue to decrease. In this way, ΔR_S (see Eq. (4.3)) and, consequently, V_{dc} increases, proving that the presence of a large enough VCMA effect can significantly improve the sensitivity of the skyrmion based STD.

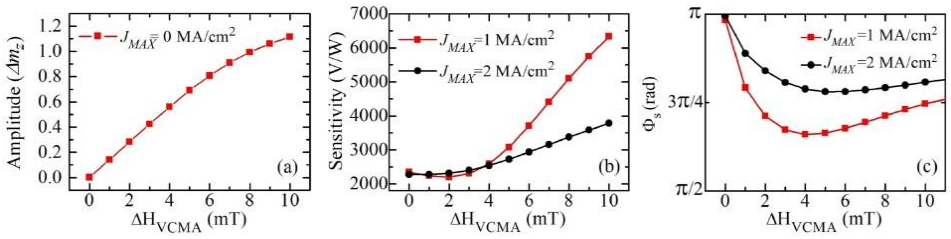

Fig. 4.11: (a) amplitude of the *z*-component of the magnetization driven by ΔH_{VCMA} at J_{MAX} =0 MA/cm^2; (b) sensitivity as a function of the ΔH_{VCMA}, considering the optimal contact diameter of Fig. 4(a) (d_C=40 nm), computed for J_{MAX} =1 and 2 MA/cm^2. (c) Phase shift Φ_S as a function of ΔH_{VCMA} for the same microwave currents amplitudes of (b).

To estimate the VCMA contribution, we consider the optimal case of Fig. 4.10(a), J_{MAX} =1 MA/cm^2 and a typical experimental VCMA value of 60 mT/V [30]. However, by using *state of the art* values of VCMA, the $\Delta H_{VCMA} \approx 1$ mT would result negligible giving rise to a negligible effect in our devices.

In summary, we have proposed a zero field and an unbiased skyrmion based STD for passive microwave detection and energy

harvesting application. The skyrmion is stabilized by the *i*-DMI and when it is supplied by a microwave spin current with perpendicular polarization, a breathing mode is excited. The change in the size of the skyrmion is converted to a change of the TMR signal, which gives rise to a detection voltage. We have pointed out that sensitivities as large as 2,000 V/W can be achieved for optimized contact diameter. Our results open a path for fundamental physics in understanding the skyrmion dynamical properties and for the design of STD with a non-uniform ground state.

5. JOURNAL ARTICLES

5.1 Published articles

J1. Riccardo Tomasello, Mario Carpentieri, Giovanni Finocchio. "*Dynamical properties of three terminal magnetic tunnel junctions: spintronics meets spin-orbitronics*".
Applied Physics Letters, Vol.103, December 2013, pp. 252408-1-5. ISSN: 0003-6951. IF: 3.52. DOI: 10.1063/1.4851939 – 2013.

J2. Riccardo Tomasello, Mario Carpentieri, Giovanni Finocchio. "*Influence of the Dzyaloshinskii-Moriya interaction on the spin-torque diode effect*".
Journal of Applied Physics, Vol. 115, March 2014, 17C730-1-3 .
ISSN: 0021-8979. IF: 2.18. DOI: 10.1063/1.4867750 – 2014.

J3. Riccardo Tomasello, Vito Puliafito, Bruno Azzerboni, Giovanni Finocchio.
"Switching properties in Magnetic Tunnel Junctions with Interfacial Perpendicular Anisotropy: micromagnetic study".
IEEE Transactions on Magnetics, Vol. 50, Issue 7, July 2014, pp. 1-5. ISSN:0018-9464. IF:1.39. DOI: 10.1109/TMAG.2014.2307280 – 2014.

J4. Riccardo Tomasello, Eduardo Martinez, Roberto Zivieri, Luis Torres, Mario Carpentieri, Giovanni Finocchio.
"*A strategy for the design of skyrmion racetrack memories*".
Scientific Reports, Vol. 4, 6784, October 2014.
ISSN: 2045-2322. IF: 5.58. DOI: 10.1038/srep06784 – 2014.

J5. Marco Ricci, Pietro Burrascano, Mario Carpentieri, Riccardo Tomasello, Giovanni Finocchio.
"*Chirp Spectroscopy Applied to the Characterization of Ferromagnetic Resonance in Magnetic Tunnel Junctions*".
IEEE Transactions on Magnetics, Vol. 50, Issue 11, November 2014, 1402305.
ISSN:0018-9464. IF:1.39. DOI: 10.1109/TMAG.2014.2323269-2014.

J6. Mario Carpentieri, Riccardo Tomasello, Marco Ricci, Pietro Burrascano, Giovanni Finocchio.
"*Micromagnetic Study of Electrical-Field-Assisted Magnetization Switching in MTJ Devices*".
IEEE Transactions on Magnetics, Vol. 50, Issue 11, November 2014, 1401804.
ISSN:0018-9464. IF:1.39. DOI: 10.1109/TMAG.2014.2327192-2014.

J7. Giulio Siracusano, Riccardo Tomasello, Vito Puliafito, Anna Giordano, Bruno Azzerboni, Aurelio La Corte, Mario Carpentieri, Giovanni Finocchio.
"*Intrinsic synchronization of an array of spin-torque oscillators driven by the spin-Hall effectt*".
Journal of Applied Physics, Vol. 117, March 2015, 17E504-1-4.
ISSN: 0021-8979. IF: 2.18. DOI: 10.1063/1.4914880- 2015.

J8. Mario Carpentieri, Riccardo Tomasello, Roberto Zivieri, Giovanni Finocchio.
"*Topological, non-topological and instanton droplets driven by spintransfer torque in materials with perpendicular magnetic anisotropy and Dzyaloshinskii–Moriya Interaction*".
Scientific Reports, Vol. 5, 16184, November 2015.
ISSN: 2045-2322. IF: 5.60. DOI: 10.1038/srep16184-2015.

5.2 Submitted articles

J9. S. Fin, R. Tomasello, D. Bisero, M. Marangolo, M. Sacchi, H. Popescu, M. Eddrief, C. Hepburn, G. Finocchio, M. Carpentieri, A. Rettori, M. G. Pini, and S. Tacchi
"*In plane rotation of magnetic stripe domains in $Fe_{1-x}Ga_x$ thin films*".
Accepted for publication on Physical Review B.

J10. Giovanni Finocchio, Marco Ricci, Riccardo Tomasello, Anna Giordano, Marco Lanuzza, Vito Puliafito, Pietro Burrascano, Bruno Azzerboni, and Mario Carpentieri
"*Skyrmion based microwave detector and harvesting*".
Submitted to Applied Physics Letters.

J11. Giulio Siracusano, Francesco Lamonaca, Riccardo Tomasello, Francesca Garescì, Aurelio La Corte, Domenico Luca Carnì, Mario Carpentieri, Domenico Grimaldi, and Giovanni Finocchio
"*Damage evaluation through Hilbert-Huang Transform of acoustic emission signals*".
Submitted to Mechanical Systems and Signal Processing.

BIBLIOGRAPHY

[1] G. Bertotti, "Hysteresis in Magnetism - For Physicists, Materials Scientists and Engineers", *Academic Press* (1998).

[2] B. Hillebrands, and K. Ounadjela, "Spin Dynamics in Confined Magnetic Structures I", *Springer*, Berlin (2002).

[3] B. Hillebrands, and A. Thiaville, "Spin Dynamics in Confined Magnetic Structures III", *Springer*, Berlin (2006).

[4] L. D. Landau, and E. Lifshitz, "On the theory of the dispersion of magnetic permeability in ferromagnetic bodies", *Phys. Z. Sowjetunion* **8**,153-169 (1935).

[5] L. D. Landau, and E. Lifshitz, "Electrodynamics of Continuous Media", *Pergamon Press*, Oxford (1960).

[6] W. F. Brown, "Magnetostatic Principles in Ferromagnetism", *North-Holland Pub. Co.* (1962).

[7] W. F. Brown, "Micromagnetics", *Interscience Tracts on Physics and Astronomy*, Interscience Publishers (John Wiley and Sons), *New York – London* (1963).

[8] W. F. Jr. Brown, and A. E. La Bonte, "Structure and energy of one-dimensional domain walls in ferromagnetic thin films", *J. Appl. Phys.* **36**, 1380–1386 (1965).

[9] E. Della Torre, "Fine particle micromagnetics", *IEEE Trans. Magn.* **21**, 1423-1425 (1985).

[10] E. Della Torre, "Magnetization calculation of fine particles", *IEEE Trans. Magn.* **22**, 484-489 (1986).

[11] J. D- Jackson. "Classical Electrodynamics", *New York: Wiley* (1999).

[12] W. T. Coffey, Y. P. Kalmykov, and J. T. Waldrom, "The Langevin Equation, with applications to stochastic problems in Physics, Chemistry and Electrical Engineering", *Singapore: World Scientific* (1996).

[13] W.F. Brown, "Thermal fluctuations of a single-domain particle", *Phys. Rev.* **130**, 1677-1686 (1963).

[14] G. Finocchio, I. N. Krivorotov, X. Cheng, L. Torres, and B. Azzerboni, "Micromagnetic understanding of stochastic resonance driven by spin-transfer-torque", *Phys. Rev. B* **83**, 134402-1-9 (2011).

[15] A. Landé, "Über den anomalen Zeemane_ekt (Teil I)", *Zeitschrift für Physik* **5,** 231 (1921).

[16] A. Landé, "Über den anomalen Zeemane_ekt (Teil II)", *Zeitschrift für Physik* **7,** 398 (1921).

[17] T. Gilbert, "A Lagrangian formulation of the gyromagnetic equation of the magnetic field", *Phys. Z. Sowjetunion* **100,** 1243 (1955).

[18] T. Gilbert, "A phenomenological theory of damping in ferromagnetic materials", *IEEE Trans. Magn.* **40**, 3443 (2004).

[19] J. Slonczewski, "Current driven excitation of magnetic multilayers", *J. Magn. Magn. Mater*. **159**, L1-L7(1996).

[20] L. Berger, "Emission of spin waves by a magnetic multilayer traversed by a current", *Phys. Rev. B* **54**, 9353-9358 (1996).

[21] D. C. Ralph, and M. D. Stiles, "Spin-Transfer Torques", *J. Magn. Magn. Mater*. **320**, 1190-1216 (2008).

[22] J. Åkerman, "Toward a universal memory", *Science* **308**, 508–510 (2005).

[23] Z. Zeng, G. Finocchio, and H. Jiangc, "Spin-Transfer nano-oscillators", *Nanoscale* **5**, 2219-2231(2013).

[24] D. Bhowmik, L. You, and S. Salahuddin, "Spin Hall effect clocking of nanomagnetic logic without a magnetic field", *Nat. Nanotech.* **9**, 59-63 (2014).

[25] J. Slonczewski, "Currents, torques, and polarization factors in magnetic tunnel junctions", *Phys. Rev B*, **71**, 024411, (2005).

[26] A. Slavin, and V. Tiberkevich, "Nonlinear Auto-Oscillator Theory of Microwave Generation by Spin-Polarized Current", *IEEE Trans. Magn.* **45**, 1875-1918 (2009).

[27] J. C. Sankey, Y.-T. Cui, J. Z. Sun, J. C. Slonczewski, R. A. Buhrman, and D. C. Ralph, "Measurement of the spin-transfer-torque vector in magnetic tunnel junctions", *Nat. Phys.* **4**, 67-71 (2008).

[28] S. Zhang, and Z. Li, "Roles of Nonequilibrium Conduction Electrons on the Magnetization Dynamics of Ferromagnets", *Phys. Rev. Lett.* **93**, 127204 (2004).

[29] W.-G. Wang, M. Li, S. Hageman, and C. L. Chien, "Electric-field-assisted switching in magnetic tunnel junctions", *Nat. Mater.* **11**, 64-68 (2012).

[30] J. Zhu, J. A. Katine, G. E. Rowlands, Y.-J. Chen, Z. Duan, J. G. Alzate, P. Upadhyaya, J. Langer, P. K. Amiri, K. L. Wang, and I. N. Krivorotov, "Voltage-Induced Ferromagnetic Resonance in Magnetic Tunnel Junctions", *Phys. Rev. Lett.* **108**, 197203 (2012).

[31] S. Ikeda, K. Miura, H. Yamamoto, K. Mizunuma, H. D. Gan, M. Endo, S. Kanai, J. Hayakawa, F. Matsukura, and H. Ohno, "A perpendicular-anisotropy CoFeB–MgO magnetic tunnel junction", *Nat. Mater.* **9**, 721-724 (2010).

[32] T. Maruyama, Y. Shiota, T. Nozaki, K. Ohta, N. Toda, M. Mizuguchi, A. A. Tulapurkar, T. Shinjo, M. Shiraishi, S. Mizukami, Y. Ando, and Y. Suzuki, "Large voltage-induced magnetic anisotropy change in a few atomic layers of iron", *Nat. Mater.* **4**, 158-161 (2008).

[33] J. E. Hirsch, "Spin Hall effect", *Phys. Rev. Lett.* **83**, 1834 (1999).

[34] I. M. Miron, K. Garello, G. Gaudin, P.-J. Zermatten, M. V. Costache, S. Auffret, S. Bandiera, B. Rodmacq, A. Schuhl, and P. Gambardella, "Perpendicular switching of a single ferromagnetic layer induced by in-plane current injection", *Nature* **476**, 189-193 (2011).

[35] L. Liu, C.-F. Pai, Y. Li, H. W. Tseng, D. C. Ralph, and R. A. Buhrman, "Spin-Torque Switching with the Giant Spin Hall Effect of Tantalum", *Science* **336**, 555-558 (2012).

[36] V. E. Demidov, S. Urazhdin, H. Ulrichs, V. Tiberkevich, A. Slavin, D. Baither, G. Schmitz, and S. O. Demokritov, "Magnetic nano-oscillator driven by pure spin current", *Nat. Mater.* **11**, 1028-1031 (2012).

[37] L. Liu, C.-F. Pai, D. C. Ralph, and R. A. Buhrman, "Current-induced switching of perpendicularly magnetized magnetic layers using spin torque from the Spin-Hall effect", *Phys. Rev. Lett.* **109**, 186602 (2012).

[38] P. Gambardella, and I. M. Miron, "Current-induced spin–orbit torques", *Phil. Trans. R. Soc. A* **369**, 3175–3197 (2011).

[39] A. Manchon, and S. Zhang, "Theory of spin torque due to spin-orbit coupling", *Phys. Rev. B* **79**, 094422 (2009).

[40] M .I. Dyakonov, and V. I. Perel, "Possibility of orientating spins with current", *Sov. Phys. JETP Lett.* **13**, 467 (1971).

[41] M .I. Dyakonov, and V. I. Perel, "Current-induced spin orientation of electrons in semiconductors", *Phys. Lett.* A **35**, 459 (1971).

[42] A. Hoffmann, "Spin-Hall effects in metals", *IEEE Trans. Magn.* **49**, 5172–5193 (2013).

[43] I. M. Miron, T. Moore, H. Szambolics, L. D. Buda-Prejbeanu, S. Auffret, B. Rodmacq, S. Pizzini, J. Vogel, M. Bonfim, A. Schuhl, and G. Gaudin, "Fast current-induced domain-wall motion controlled by the Rashba effect", *Nat. Mater.* **10**, 419-423 (2011).

[44] E. Martinez, S. Emori, and G. S. D. Beach, "Current-driven domain wall motion along high perpendicular anisotropy multilayers: The role of the Rashba field, the spin Hall effect, and the Dzyaloshinskii-Moriya interaction", *Appl. Phys. Lett.* **103**, 072406 (2013).

[45] I. Dzyaloshinskii, "A thermodynamic theory of 'weak' ferromagnetism of antiferromagnetics", *J. Phys. Chem. Solids* **4**, 241–255 (1958).

[46] T. Moriya, "New mechanism of anisotropic superexchange interaction", *Phys. Rev. Lett.* **4**, 228 (1960).

[47] A. Fert, V. Cros, and J. Sampaio, "Skyrmions on the track", *Nat. Nanotech.* **8**, 152-156 (2013).

[48] S. Rohart, and A. Thiaville, "Skyrmion confinement in ultrathin film nanostructures in the presence of Dzyaloshinskii- Moriya interaction", *Phys. Rev. B* **88**, 184422 (2013).

[49] L. Liu, C.-F. Pai, D. C. Ralph, and R. A. Buhrman, "Magnetic Oscillations Driven by the Spin Hall Effect in 3-Terminal Magnetic Tunnel Junction Devices", *Phys. Rev. Lett.* **109**, 186602 (2012).

[50] T. Jungwirth, J. Wunderlich, and K. Olejník, "Spin Hall effect devices", *Nat. Mater.* **11**, 382–390 (2012).

[51] T. H. R. Skyrme, "A unified field theory of mesons and baryons", *Nucl. Phys.* **31,** 556–569 (1962).

[52] C. Moutafis, S. Komineas, and J. A. C. Bland, "Dynamics and switching processes for magnetic bubbles in nanoelements", *Phys. Rev. B* **79**, 224429 (2009).

[53] G. Finocchio, V. Puliafito, S. Komineas, L. Torres, O. Ozatay, T. Hauet and B. Azzerboni, "Nanoscale spintronic oscillators based on the excitation of confined soliton modes", *J. Appl. Phys.* **114,** 163908 (2013).

[54] H.-B. Braun, "Topological effects in nanomagnetism: from superparamagnetism to chiral quantum solitons", *Adv. Phys.* **61**, 1-116 (2012).

[55] Y. Zhou, and M. Ezawa, "A reversible conversion between a skyrmion and a domain-wall pair in a junction geometry", *Nat. Comm.* **5**, 4652 (2014).

[56] T. Shinjo, T. Okuno, R. Hassdorf, K. Shigeto, and T. Ono, "Magnetic Vortex Core Observation in Circular Dots of Permalloy", *Science* **289**, 930-932 (2000).

[57] A. Giordano, V. Puliafito, L. Torres, M. Carpentieri, B. Azzerboni, and G. Finocchio, "Micromagnetic study of Spin-Transfer-Driven vortex dipole and vortex quadrupole dynamics", *IEEE Trans. Magn.* **50**, 4300404 (2014).

[58] U. K. Rossler, A. N. Bogdanov, and C. Pfleiderer, "Spontaneous skyrmion ground states in magnetic metals", *Nature* **442**, 797–801 (2006).

[59] S. Mühlbauer, B. Binz, F. Jonietz. C. Pfleiderer, A. Rosch, A. Neubauer. R. Georgii, P. Böni, "Skyrmion lattice in a chiral magnet", *Science* **323**, 915–919 (2009).

[60] X. Z. Yu, Y. Onose, N. Kanazawa, J. H. Park, J. H. Han, Y. Matsui, N. Nagaosa, and Y. Tokura, "Real-space observation of a two-dimensional skyrmion crystal", *Nature* **465**, 901-904 (2010).

[61] S. Heinze, K. von Bergmann, M. Menzel, J. Brede, A. Kubetzka, R. Wiesendanger, G. Bihlmayer and S. Blügel, "Spontaneous atomic-scale magnetic skyrmion lattice in two dimensions", *Nature Phys.* **7**, 713-718 (2011).

[62] S. X. Huang and C. L. Chien, "Extended skyrmion phase in epitaxial FeGe (111) thin films", *Phys. Rev. Lett.* **108**, 267201 (2012).

[63] J. Iwasaki, M. Mochizuki, and N. Nagaosa, "Universal current-velocity relation of skyrmion motion in chiral magnets", *Nat. Comm.* **4**, 1463 (2013).

[64] J. Iwasaki, M. Mochizuki, and N. Nagaosa, "Current-induced skyrmion dynamics in constricted geometries", *Nat. Nanotech.* **8**, 742-747 (2013).

[65] J. Sampaio, V. Cros, S. Rohart, A. Thiaville, and A. Fert, "Nucleation, stability and current-induced motion of isolated magnetic skyrmions in nanostructures", *Nat. Nanotech.* **8**, 839-844 (2013).

[66] X. Zhang, M. Ezawa, and Yan Zhou, "Magnetic skyrmion logic gates: conversion, duplication and merging of skyrmions", *Sci. Rep.* **5**, 9400 (2015).

[67] X. Zhang, Y. Zhou, M. Ezawa, G. P. Zhao, and W. Zhao, "Magnetic skyrmion transistor: skyrmion motion in a voltage-gated nanotrack", *Sci. Rep.* **5**, 11369 (2015).

[68] J. -V. Kim, F. Garcia-Sanchez, J. Sampaio, C. Moreau-Luchaire, V. Cros, and A. Fert, "Breathing modes of confined skyrmions in ultrathin magnetic dots", *Phys. Rev.* B **90,** 064410 (2014).

[69] R. H. Liu, W. L. Lim, and S. Urazhdin, "Dynamical Skyrmion State in a Spin Current Nano-Oscillator with Perpendicular Magnetic Anisotropy", *Phys. Rev. Lett.* **114,** 137201 (2015).

[70] Y. Zhou, E. Iacocca, A. A. Awad, R. K. Dumas, F. C. Zhang, H. B. Braun, and J. Åkerman, "Dynamically stabilized magnetic skyrmions", *Nat. Comm.* **6**, 8193 (2015).

[71] S. Zhang, J. Wang, Q. Zheng, Q. Zhu, X. Liu, S. Chen, C. Jin, Q. Liu, C. Jia, D. Xue, "Current-induced magnetic skyrmions oscillator", *New Journal of Physics* **17,** 023061 (2015).

[72] C. Moreau-Luchaire, C. Moutafis, N. Reyren, J. Sampaio, N. Van Horne, C.A.F. Vaz, K. Bouzehouane, K. Garcia, C. Deranlot, P. Warnicke, P. Wohlhüter, J.M. George, J. Raabe, V. Cros, and A. Fert, "Skyrmions at room temperature : From magnetic thin films to magnetic multilayers", arXiv:1502.07853.

[73] S. Woo, K. Litzius, B. Krüger, M.-Y. Im, L. Caretta, K. Richter, M. Mann, A. Krone, R. Reeve, M. Weigand, P. Agrawal, P. Fischer, M. Kläui, and G. S. D.

Beach, "Observation of room temperature magnetic skyrmions and their current-driven dynamics in ultrathin Co films", arXiv:1502.07376.

[74] http://www.toshiba.co.jp/about/press/2012_12/pr1001.htm

[75] M. Julliere, "Tunneling between ferromagnetic films", *Phys. Lett. A* **54**, 225-226 (1975).

[76] T. Miyazaki, and N. Tezuka, "Giant magnetic tunneling effect in Fe/Al2O3/Fe junction", *J. Magn. Magn. Mater*. **139**, L213-L234 (1995).

[77] J. S. Moodera, L. R. Kinder, Terrilyn M. Wong, and R. Meservey, "Large Magnetoresistance at Room Temperature in Ferromagnetic Thin Film Tunnel Junctions", *Phys. Rev. Lett.* **74**, 3273 (1995).

[78] D. Wang, C. Nordman, J. Daughton , Z. Qian, and J. Fink, "70% TMR at room temperature for SDT sandwich junctions with CoFeB as free and reference Layers", *IEEE Trans. Magn.* **40**, 2269 (2004).

[79] S. Yuasa, T. Nagahama, A. Fukushima, Y. Suzuki, and K. Ando, "Giant room-temperature magnetoresistance in single-crystal Fe/MgO/Fe magnetic tunnel junctions", *Nat. Mater.* **3**, 868 - 871 (2004).

[80] Y. M. Lee, J. Hayakawa, S. Ikeda, F. Matsukura and H. Ohno, "Effect of electrode composition on the tunnel magnetoresistance of pseudo-spin-valve magnetic tunnel junction with a MgO tunnel barrier", *Appl. Phys. Lett.* **90**, 212507 (2007).

[81] S. Tehrani, J. Slaughter, M. Deherrera, B. Engel, N. Rizzo, J. Salter, M. Durlam, R. Dave, J. Janesky, and B. Butcher, "Magnetoresistive random access memory using magnetic tunnel junctions", *Proc. IEEE* **91**, 703-714 (2003).

[82] M. Durlam, D. Addie, J. Akerman, B. Butcher, P. Brown, J. Chan, M. DeHerrera, B. N. Engel, B. Feil, G. Grynkewich, J. Janesky, M. Johnson, K. Kyler, J. Mob, J. Martin, K. Nagel, J. Ren, N.D. Rizzo, T. Rodriguez, L. Savtchenko, J. Salter, J.M. Slaughter, K. Smith, J.J. Sun, M. Lien, K. Papworth, P. Shah, W. Qin, R Williams, L. Wise, and S. Tehrani, "A 0.18 mm 4 Mb toggling MRAM", *IEEE IEDM Tech. Dig.* **9**, 995 (2003)

[83] Y. Nishi, "Advances in non-volatile memory and storage technology", *Elsevier* (2014).

[84] J.-G. Zhu, "Magnetoresistive random access memory: The path to competitiveness and scalability", *Proc. IEEE* **96**, 1786-1798 (2008).

[85] J. A. Katine, and E. E. Fullerton, "Device implications of spin-transfer torques", *J. Magn. Magn. Mater.* **320**, 1217-1226 (2008).

[86] S. Mangin, Y. Henry, D. Ravelosona, J. A. Katine, and E. E. Fullerton, "Reducing the critical current for spin-transfer switching of perpendicularly magnetized nanomagnets", *Appl. Phys. Lett.* **94**, 012502 (2009).

[87] Z. Diao, D. Apalkov, M. Pakala, Y. Ding, A. Panchula, and Y. Huai, "Spin transfer switching and spin polarization in magnetic tunnel junctions with MgO and AlO*x* barriers", *Appl. Phys. Lett.* **87**, 232502 (2005).

[88] Z. Diao, A. Panchula, Y. Ding, M. Pakala, S. Wang, Z. Li, D. Apalkov, H. Nagai, A. Driskill-Smith, L.-C. Wang, E. Chen, and Y. Huai, "Spin transfer switching in dual MgO magnetic tunnel junctions", *Appl. Phys. Lett.* **90**, 132508 (2007).

[89] A. V. Khvalkovskiy, D. Apalkov, S. Watts, R. Chepulskii, R. S. Beach, A. Ong, X. Tang, A. Driskill-Smith, W. H. Butler, P. B. Visscher, D. Lottis, E. Chen, V.

Nikitin, and M. Krounbi, "Basic principles of STT-MRAM cell operation in memory arrays", *J. Phys. D: Appl. Phys.* **46**, 074001 (2013).

[90] M. Tsoi, A. G. M. Jansen, J. Bass, W.-C. Chiang, M. Seck, V. Tsoi, and P. Wyder, "Excitation of a Magnetic Multilayer by an Electric Current", *Phys. Rev. Lett.* **80**, 4281 (1998).

[91] Y. Huai, F. Albert, P. Nguyen, M. Pakala, and T. Valet, "Observation of spin-transfer switching in deep submicron-sized and low-resistance magnetic tunnel junctions", *Appl. Phys. Lett.* **84**, 3118 (2004).

[92] S. Mangin, D. Ravelosona, J. A. Katine, M. J. Carey, B. D. Terris, and E. E. Fullerton, "Current-induced magnetization reversal in nanopillars with perpendicular anisotropy", *Nat. Mater.* **5**, 210 - 215 (2006).

[93] D. C. Worledge, G. Hu, D. W. Abraham, J. Z. Sun, P. L. Trouilloud, J. Nowak, S. Brown, M. C. Gaidis, E. J. O'Sullivan, and R. P. Robertazzi, "Spin torque switching of perpendicular Ta|CoFeB|MgO-based magnetic tunnel junctions", *Appl. Phys. Lett.* **98**, 022501 (2011).

[94] G. Finocchio, M. Carpentieri, E. Martinez, and B. Azzerboni, "Switching of a single ferromagnetic layer driven by spin Hall effect", *Appl. Phys. Lett.* **102**, 212410 (2013).

[95] Y. Kim, X. Fong, K.-W. Kwon, M.-C. Chen, and K. Roy, "Multilevel Spin-Orbit Torque MRAMs", *IEEE Trans. Magn.* **62**, 561-568 (2015).

[96] M. Hosomi, H. Yamagishi, T. Yamamoto, K. Bessho, Y. Higo, K. Yamane, H. Yamada, M. Shoji, H. Hachino, C. Fukumoto, H. Nagao, and H. Kano, "A novel nonvolatile memory with spin torque transfer magnetization switching: Spin-RAM", *IEDM Tech. Dig.*, 473 (2005).

[97] T. Kawahara, R. Takemura, K. Miura, J. Hayakawa, S. Ikeda, Y. Lee, R. Sasaki, Y. Ito, T. Meguro, F. Matsukura, H. Takahashi, H. Matsuoka, and H. Ohno, "2 Mb spin-transfer torque RAM with bit-bt-bit bidirectional current write and parallelizing-direction current read", *ISSCC Tech. Digest*, 480 (2007).

[98] C. Demerjian, "Everspin makes ST-MRAM a reality LSI AIS 2012: Non-volatile memory with DDR3 speeds" (2012).

[99] Data drawn from public sources.

[100] P. K. Amiri, Z. M. Zeng, J. Langer, H. Zhao, G. Rowlands, Y. J. Chen, I. N. Krivorotov, J.-P. Wang, H. W. Jiang, J. A. Katine, Y. Huai, K. Galatsis, and K. L. Wang, "Switching current reduction using perpendicular anisotropy in CoFeB-MgO magnetic tunnel junctions", *Appl. Phys. Lett.* **98**, 112507 (2011).

[101] R. Tomasello, V. Puliafito, B. Azzerboni, and G. Finocchio, "Switching Properties in Magnetic Tunnel Junctions With Interfacial Perpendicular Anisotropy: Micromagnetic Study", *IEEE Trans. Magn.* **50**, 7100305 (2014).

[102] R. Lavrijsen, P. V. Paluskar, C. T. J. Loermans, P. A. van Kruisbergen, J. T. Kohlhepp, H. J. M. Swagten, B. Koopmans, E. Snoeck, "Magnetism in Co80−*x* Fe*x* 20: Effect of crystallization", *J. Appl. Phys.*, **109**, 093905 (2011).

[103] M. Carpentieri, G. Finocchio, B. Azzerboni, L. Torres, L. Lopez- Diaz, and E. Martinez, "Effect of the classical ampere field in micromagnetic computations of spin polarized current-driven magnetization processes", *J. Appl. Phys.* **97**, 10C713 (2005).

[104] K. Ito, T. Devolder, C. Chappert, M. J. Carey, and J. A. Katine, "Micromagnetic simulation on effect of oersted field and hard axis field in spin transfer torque switching", *J. Phys. D, Appl. Phys.* **40**, 1261 (2007).

[105] M. Carpentieri, M. Ricci, P. Burrascano, L. Torres, and G. Finocchio, "Wideband microwave signal to trigger fast switching processes in magnetic tunnel junctions", *J. Appl. Phys.* **111**, 07C909 (2012).

[106] S. Kanai, M. Yamanouchi, S. Ikeda, Y. Nakatani, F. Matsukura, and H. Ohno, "Electric field-induced magnetization reversal in a perpendicular-anisotropy CoFeB-MgO magnetic tunnel junction", *Appl. Phys. Lett.* **101**, 122403 (2012).

[107] S. Kanai, M. Yamanouchi, S. Ikeda, Y. Nakatani, F. Matsukura, and H. Ohno, "Electric field-induced magnetization switching in CoFeB-MgO—Static magnetic field angle dependence", *IEEE Trans. Magn.* **50**, 4200103 (2014).

[108] P. K. Amiri, P. Upadhyaya, J. G. Alzate, and K. L. Wang, "Electric-field-induced thermally assisted switching of monodomain magnetic bits", *J. Appl. Phys.* **113**, 013912 (2013).

[109] M. Carpentieri, R. Tomasello, M. Ricci, P. Burrascano, and G. Finocchio, "Micromagnetic Study of Electrical-Field-Assisted Magnetization Switching in MTJ Devices", *IEEE Trans. Magn.* **50**, 140804 (2014).

[110] G. Finocchio, O. Ozatay, L. Torres, R. A. Buhrman, D. C. Ralph, and B. Azzerboni, "Spin-torque-induced rotational dynamics of a magnetic vortex dipole", *Phys. Rev. B* **78**, 174408 (2008).

[111] S. Parkin, and S.-H. Yang, "Memory on the racetrack", *Nat. Nanotech.* **10**, 195-198 (2015).

[112] S. S. P. Parkin, M. Hayashi, and L. Thomas, "Magnetic Domain-Wall racetrack memory", *Science* **320**, 190-194 (2008).

[113] M. H. Kryder, and C. S. Kim, "After Hard Drives—What Comes Next?", *IEEE Trans. Magn.* **45**, 3403-3413 (2009).

[114] D. Chiba, G. Yamada, T. Koyama, K. Ueda, H. Tanigawa, S. Fukami, T. Suzuki, N. Ohshima, N. Ishiwata, Y. Nakatani, and T. Ono, "Control of Multiple Magnetic Domain Walls by Current in a Co/Ni Nano-Wire", *Appl. Phys. Express* **3,** 073004 (2010).

[115] S. Emori, U. Bauer, S.-M. Ahn, E. Martinez, and G. S. D. Beach, "Current-driven dynamics of chiral ferromagnetic domain walls", *Nat. Mater.* **12**, 611–616 (2013).

[116] K.-S. Ryu, L. Thomas, S.-H. Yang, and S. Parkin, "Chiral spin torque at magnetic domain walls", *Nat. Nanotech.* **8**, 527–533 (2013).

[117] K.-S. Ryu, S.-H. Yang, L. Thomas, and S. S. P. Parkin, "Chiral spin torque arising from proximity-induced magnetization", *Nat. Comm.* **5**, 3910 (2014).

[118] S.-H. Yang, K.-Su Ryu, and S. S. P. Parkin, "Domain-wall velocities of up to 750 m s−1 driven by exchange-coupling torque in synthetic antiferromagnets", *Nat. Nanotech.* **10**, 221–226 (2015).

[119] X. Zhang, G. P. Zhao, H. Fangohr, J. P. Liu, W. X. Xia, J. Xia, and F. J. Morvan, "Skyrmion-skyrmion and skyrmion-edge repulsions in skyrmion-based racetrack memory", *Sci. Rep.* **5**, 7643 (2015).

[120] R. Tomasello, E. Martinez, R. Zivieri, L. Torres, M. Carpentieri, and G. Finocchio, "A strategy for the design of skyrmion racetrack memories", *Sci. Rep.* **4**, 6784 (2014).

[121] K. M. D. Hals, and A. Brataas, "Spin-orbit torques and anisotropic magnetization damping in skyrmion crystals", *Phys. Rev. B* **89**, 064426 (2014).

[122] A. A. Thiele, "Steady-state motion of magnetic domains", *Phys. Rev. Lett.* **30**, 230 (1972).

[123] M. E. Knoester, J. Sinova, and R. A. Duine, "Phenomenology of current-skyrmion interactions in thin films with perpendicularmagnetic anisotropy", *Phys. Rev. B* **89**, 064425 (2014).

[124] A. Neubauer, C. Pfleiderer, B. Binz, A. Rosch, R. Ritz, P. G. Niklowitz, and P. Böni "Topological Hall effect in the A phase of MnSi", *Phys. Rev. Lett.* **102**, 186602 (2009).

[125] T. Schulz, R. Ritz, A. Bauer, M. Halder, M. Wagner, C. Franz, C. Pfleiderer, K. Everschor, M. Garst, and A. Rosch, "Emergent electrodynamics of skyrmions in a chiral magnet", *Nat. Phys.* **8**, 301–304 (2012).

[126] M. Bode, M. Heide, K. von Bergmann, P. Ferriani, S. Heinze, G. Bihlmayer, A. Kubetzka, O. Pietzsch, S. Blügel, and R. Wiesendanger, "Chiral magnetic order at surfaces driven by inversion asymmetry", *Nature* **447**, 190–193 (2007).

[127] C.-F. Pai, L. Liu, Y. Li, H. W. Tseng, D. C. Ralph, and R. A. Buhrman, "Spin transfer torque devices utilizing the giant spin Hall effect of tungsten", *Appl. Phys. Lett.* **101**, 122404 (2012).

[128] Y. Nakatani, A. Thiaville, and J. Miltat, "Faster magnetic walls in rough wires", *Nat. Mater.* **2**, 521–523 (2003).

[129] A. Hrabec, N. A. Porter, A. Wells, M. J. Benitez Romero, G. Burnell, S. McVitie, D. McGrouther, T. A. Moore, C. H. Marrows, "DMI meter: Measuring the Dzyaloshinskii-Moriya interaction inversion in Pt/Co/Ir/Pt multilayers", arXiv:1402.5410v1.

[130] M. Heide, G. Bihlmayer, and S. Blugel, "Dzyaloshinskii-Moriya interaction accounting for the orientation of magnetic domains in ultrathin films: Fe/W(110)", *Phys. Rev. B* **78**, 140403(R) (2008).

[131] M. Mochizuki, "Spin-Wave Modes and Their Intense Excitation Effects in Skyrmion Crystals", *Phys. Rev. Lett.* **108**, 017601 (2012).

[132] M. N. Baibich, J. M. Broto, A. Fert, F. Nguyen Van Dau, F. Petroff, P. Etienne, G. Creuzet, A. Friederich, and J. Chazelas, "Giant Magnetoresistance of (001)Fe/(001)Cr Magnetic Superlattices", *Phys. Rev. Lett.* **61**, 2472 (1988).

[133] G. Binasch, P. Grünberg, F. Saurenbach, and W. Zinn, "Enhanced magnetoresistance in layered magnetic structures with antiferromagnetic interlayer exchange", *Phys. Rev. B* **39**, 4828(R) (1989).

[134] R. Scranton, "IBM Deskstar 16 GP (14GXP); First Use of Giant Magnetoresistance (GMR) Heads in a Commercial Product", *Computer History Museum article* (2012).

[135] B. Dieny, B. A. Gurney, S. E. Lambert, D. Mauri, S. S. P. Parkin, V. S. Speriousu, and D. Wilholt, "Magnetoresisitive Sensor Based on the Spin Valve Effect", *patent* **5**, 206, 590 (1993).

[136] D. E. Heim, R. E. Fontana, V. S. Speriousu, B. A. Gurney, and M. L. Williams, "Design and Operation of Spin Valve Sensors", *IEEE Trans. Magn.* **30**, 316 (1994).

[137] B. A. Gurney, and V. S. Speriousu, "For key technical contributions to the development of spin valve giant magnetoresistance recording heads for computer

data storage devices", *IEEE Reynold B. Johnson Information Storage Systems Award* (2004).

[138] Seagate 100 GB Backup Plus circa 3Q 2004.

[139] S. E. Russek, W. H. Rippard, T. Cecil and R. Heindl, "Handbook of Nanophysics: Functional Nanomaterial", *CRC PrlLic*, ch. 38 (2010).

[140] S. Petit-Watelot, J.-V. Kim, A. Ruotolo, R. M. Otxoa, K. Bouzehouane, J. Grollier, A. Vansteenkiste, B. Van de Wiele, V.t Cros, and T. Devolder, "Commensurability and chaos in magnetic vortex oscillations", *Nat. Phys*. **8,** 682–687 (2012).

[141] Z. Duan, A. Smith, L. Yang, B. Youngblood, J. Lindner, V. E. Demidov, S. O. Demokritov, and I. N. Krivorotov, "Nanowire spin torque oscillator driven by spin orbit torques", *Nat. Comm*. **5**, 5616 (2014).

[142] A. N. Slavin, and V. S. Tiberkevich, "Nonlinear self-phase-locking effect in an array of current-driven magnetic nanocontacts", *Phys. Rev. B* **72**, 092407 (2005).

[143] J. Grollier, V. Cros, and and A. Fert, "Synchronization of spin-transfer oscillators driven by stimulated microwave currents", *Phys. Rev. B* **73**, 060409 (2005).

[144] V. S. Tiberkevich, A. N. Slavin, and J.-V. Kim, "Microwave power generated by a spin-torque oscillator in the presence of noise", *Appl. Phys. Lett.* **91**, 192506 (2007).

[145] K. V. Thadani, G. Finocchio, Z.-P. Li, O. Ozatay, J. C. Sankey, I. N. Krivorotov, Y.-T. Cui, R. A. Buhrman, and D. C. Ralph, "Strong linewidth variation for spin-torque nano-oscillators as a function of in-plane magnetic field angle", *Phys. Rev. B* **78**, 024409 (2008).

[146] K. Mizushima, T. Nagasawa, K. Kudo, Y. Saito, and R. Sato, "Decrease of nonlinearity and linewidth narrowing in spin-transfer oscillators under the external field applied near the hard axis", *Appl. Phys. Lett.* **94**, 152501 (2009).

[147] V. S. Pribiag, I. N. Krivorotov, G. D. Fuchs, P. M. Braganca, O. Ozatay, J. C. Sankey, D. C. Ralph, and R. A. Buhrman, "Magnetic vortex oscillator driven by d.c. spin-polarized current", *Nat. Phys.* **3**, 498–503 (2007).

[148] A. Dussaux, B. Georges, J. Grollier, V. Cros, A. V. Khvalkovskiy, A. Fukushima, M. Konoto, H. Kubota, K. Yakushiji, S. Yuasa, K. A. Zvezdin, K. Ando, and A. Fert, "Large microwave generation from current-driven magnetic vortex oscillators in magnetic tunnel junctions", *Nat. Comm.* **1**, 1–6 (2010).

[149] P. Bortolotti, A. Dussaux, J. Grollier, V. Cros, A. Fukushima, H. Kubota, K. Yakushiji, S. Yuasa, K. Ando, and A. Fert, "Temperature dependence of microwave voltage emission associated to spin-transfer induced vortex oscillation in magnetic tunnel junction", *Appl. Phys. Lett.* **100**, 042408 (2012).

[150] S. Kaka, M. R. Pufall, W. H. Rippard, T. J. Silva, S. E. Russekand, and J. A. Katine, "Mutual phase-locking of microwave spin torque nano-oscillators", *Nature* **437**, 389–392 (2005).

[151] F. B. Mancoff, N. D. Rizzo, B. N. Engeland, and S. Tehrani, "Phase-locking in double-point-contact spin-transfer devices", *Nature* **437**, 393–395 (2005).

[152] A. Ruotolo, V. Cros, B. Georges, A. Dussaux, J. Grollier, C. Deranlot, R. Guillemet, K. Bouzehouane, S. Fusil, and A. Fert, "Phase-locking of magnetic vortices mediated by antivortices", *Nat. Nanotech.* **4**, 528 (2009).

[153] M. Tsoi, A. G. M. Jansen, J. Bass, W.-C. Chiang, M. Seck, V. Tsoi, and P. Wyder, "Excitation of a Magnetic Multilayer by an Electric Current", *Phys. Rev. Lett.* **80**, 4281–4284 (1998).

[154] J. C. Slonczewski, "Excitation of spin waves by an electric current", *J. Magn. Magn. Mater.* **195**, L261–L268 (1999).

[155] S. I. Kiselev, J. C. Sankey, I. N. Krivorotov, N. C. Emley, R. J. Schoelkopf, R. A. Buhrman, and D. C. Ralph, "Microwave oscillations of a nanomagnet driven by a spin-polarized current", *Nature* **425**, 380–383 (2003).

[156] G. D. Fuchs, N. C. Emley, I. N. Krivorotov, P. M. Braganca, E. M. Ryan, S. I. Kiselev, J. C. Sankey, D. C. Ralph, R. A. Buhrman, and J. A. Katine, "Spin-transfer effects in nanoscale magnetic tunnel junctions", *Appl. Phys. Lett.*, **85**, 1205–1207 (2004).

[157] W. H. Rippard, M. R. Pufall, S. Kaka, S. E. Russek, and T. J. Silva, "Direct-Current Induced Dynamics in $Co_{90}Fe_{10}/Ni_{80}Fe_{20}$ Point Contacts", *Phys. Rev. Lett.* **92**, 027201 (2004).

[158] V. E. Demidov, S. Urazhdin, and S. O. Demokritov, "Direct observation and mapping of spin waves emitted by spin-torque nano-oscillators", *Nat. Mater.* **9**, 984–988 (2010).

[159] S. Bonetti, V. Tiberkevich, G. Consolo, G. Finocchio, P. Muduli, F. Mancoff, A. Slavin, and J. A. Akerman, "Experimental evidence of self-localized and propagating spin wave modes in obliquely magnetized current-driven nanocontacts", *Phys. Rev. Lett.* **105**, 217204 (2010).

[160] A. V. Nazarov, H. M. Olson, H. Cho, K. Nikolaev, Z. Gao, S. Stokes, and B. B. Pant, "Spin transfer stimulated microwave emission in MgO magnetic tunnel junctions", *Appl. Phys. Lett.* **88**, 162504 (2006).

[161] Q. Mistral, M. van Kampen, G. Hrkac, J.-V. Kim, T. Devolder, P. Crozat, C. Chappert, L. Lagaeand, and T. Schre, "Current-Driven Vortex Oscillations in Metallic Nanocontacts", *Phys. Rev. Lett.* **100**, 257201 (2008).

[162] G. Finocchio, O. Ozatay, L. Torres, R. A. Buhrman, D. C. Ralph, and B. Azzerboni, "Spin-torque-induced rotational dynamics of a magnetic vortex dipole", *Phys. Rev. B* **78**, 174408 (2008).

[163] C. Boone, J. A. Katine, J. R. Childress, J. Zhu, X. Cheng and I. N. Krivorotov, "Experimental test of an analytical theory of spin-torque-oscillator dynamics", *Phys. Rev. B* **79**, 140404(R) (2009).

[164] W. H. Rippard, A. M. Deac, M. R. Pufall, J. M. Shaw, M. W. Keller, S. E. Russek, G. E. W. Bauer, and C. Serpico, "Spin-transfer dynamics in spin valves with out-of-plane magnetized CoNi free layers", *Phys. Rev. B* **81**, 014426 (2010).

[165] Y. Masugata, S. Ishibashi, H. Tomita, T. Seki, T. Nozaki, Y. Suzuki, H. Kubota, A. Fukushima, and S. Yuasa, "Spin-torque induced rf oscillation in magnetic tunnel junctions with an Fe-rich CoFeB free layer", *J. Phys.: Conf. Ser.* **266**, 012098 (2011).

[166] Z. Zeng, G. Finocchio, B. Zhang, P. K. Amiri, J. A. Katine, I. N. Krivorotov, Y. Huai, J. Langer, B. Azzerboni, K. L. Wang, and H. Jiang, "Ultralow-current-density and bias-field-free spin-transfer nano-oscillator", *Sci. Rep.* **3**, 1426 (2013).

[167] T. Moriyama, G. Finocchio, M. Carpentieri, B. Azzerboni, D. C. Ralph, and R. A. Buhrman, "Phase locking and frequency doubling in spin-transfer-torque oscillators with two coupled free layers", *Phys. Rev. B* **86**, 06041 (2012).

[168] R. Tomasello, M. Carpentieri, and G. Finocchio, "Dynamical properties of three terminal magnetic tunnel junctions: Spintronics meets spin-orbitronics", *Appl. Phys. Lett.* **103**, 252408 (2013).

[169] R. H. Liu, W. L. Lim, and S. Urazhdin, "Spectral Characteristics of the Microwave Emission by the Spin Hall Nano-Oscillator", *Phys. Rev. Lett.* **110**, 147601 (2013).

[170] Z. M. Zeng, P. K. Amiri, I. N. Krivorotov, H. Zhao, G. Finocchio, J.-P. Wang, J. A. Katine, Y. Huai, J. Langer, O. K. Galatsis, K. L. Wang, and H. Jiang, "High-Power Coherent Microwave Emission from Magnetic Tunnel Junction Nano-oscillators with Perpendicular Anisotropy", *ACS Nano* **6**, 6115–6121 (2012).

[171] W. H. Rippard, M. R. Pufall, S. Kaka, T. J. Silva, S. E. Russek, and J. A. Katine, "Injection Locking and Phase Control of Spin Transfer Nano-oscillators", *Phys. Rev. Lett.* **95**, 067203 (2005).

[172] B. Georges, J. Grollier, M. Darques, V. Cros, C. Deranlot, B. Marcilhac, G. Faini, and A. Fert, "Coupling Efficiency for Phase Locking of a Spin Transfer Nano-Oscillator to a Microwave Current", *Phys. Rev. Lett.* **101**, 017201 (2008).

[173] M. Carpentieri, G. Finocchio, B. Azzerboni, and L. Torres, "Spin-transfer-torque resonant switching and injection locking in the presence of a weak external microwave field for spin valves with perpendicular materials", *Phys. Rev. B* **82**, 094434 (2010).

[174] M. Quinsat, J. F. Sierra, I. Firastrau, V. Tiberkevich, A. Slavin, D. Gusakova, L. D. Buda-Prejbeanu, M. Zarudniev, J.-P. Michel, U. Ebels, B. Dieny, M.-C. Cyrille, J. A. Katine, D. Mauri, and A. Zeltser, "Injection locking of tunnel junction oscillators to a microwave current", *Appl. Phys. Lett.* **98**, 182503 (2011).

[175] M. Carpentieri, T. Moriyama, B. Azzerboni, and G. Finocchio, "Injection locking at zero field in two free layer spin-valves", *Appl. Phys. Lett.* **102**, 102413 (2013).

[176] Y. Zhou, J. Persson, S. Bonetti, and J. Åkerman, "Tunable intrinsic phase of a spin torque oscillator", *Appl. Phys. Lett.* **92**, 092505 (2008).

[177] X. Cheng, J. A. Katine, G. E. Rowlands, and I. N. Krivorotov, "Nonlinear ferromagnetic resonance induced by spin torque in nanoscale magnetic tunnel junctions", *Appl. Phys. Lett.* **103**, 082402 (2013).

[178] S. Sani, J. Persson, S. M. Mohseni, Y. Pogoryelov, P. K. Muduli, A. Eklund, G. Malm, M. Käll, A. Dmitriev, and J. Åkerman, "Mutually synchronized bottom-up multi-nanocontact spin–torque oscillators", *Nat. Comm.* **4**, 2731(2013).

[179] G. Siracusano, R. Tomasello, V. Puliafito, A. Giordano, B. Azzerboni, A. La Corte, M. Carpentieri, and G. Finocchio, "Intrinsic synchronization of an array of spin-torque oscillators driven by the spin-Hall effect", *J. Appl. Phys.* **117**, 17E504 (2015).

[180] G. Siracusano, G. Finocchio, A. La Corte, G. Consolo, L. Torres, and B. Azzerboni, "Nonstationary magnetization dynamics driven by spin transfer torque", *Phys. Rev. B* **79**, 104438 (2009).

[181] G. Siracusano and A. La Corte, "A comparison between advanced time–frequency analyses of non-stationary magnetization dynamics in spin-torque oscillators", *Phys. B* **435**, 66–70 (2014).

[182] V. Puliafito, G. Siracusano, B. Azzerboni, and G. Finocchio, "Self-Modulated Soliton Modes Excited in a Nanocontact Spin-Torque Oscillator", *IEEE Magn. Lett.* **5**, 3000104 (2014).

[183] I. N. Krivorotov, N. C. Emley, A. G. F. Garcia, J. C. Sankey, S. I. Kiselev, D. C. Ralph, and R. A. Buhrman, "Temperature Dependence of Spin-Transfer-Induced Switching of Nanomagnets", *Phys. Rev. Lett.* **93**, 166603 (2004).

[184] L. Liu, T. Moriyama, D. C. Ralph, and R. A. Buhrman, "Spin-Torque Ferromagnetic Resonance Induced by the Spin Hall Effect", *Phys. Rev. Lett.* **106**, 036601 (2011).

[185] L. Torres, L. Lopez-Diaz, E. Martinez, G. Finocchio, M. Carpentieri, and B. Azzerboni, "Coupling of spin-transfer torque to microwave magnetic field: A micromagnetic modal analysis", *J. Appl. Phys.* **101**, 053914 (2007).

[186] G. Siracusano, A. La Corte, V. Puliafito, and G. Finocchio, "A generalized tool for accurate time-domain separation of excited modes in spin-torque oscillators", *J. Appl. Phys.* **115**, 17D108 (2014).

[187] S. Hemour, and K. Wu, "Radio-Frequency Rectifier for Electromagnetic Energy Harvesting: Development Path and Future Outlook", *Proc. IEEE* **102**, 1667-1691 (2014).

[188] S. Hemour, Y. Zhao, C. H. Petzl Lorenz, D. Houssameddine, Y. Gui, C.-M. Hu, and K. Wu, "Towards Low-Power High-Efficiency RF and Microwave Energy Harvesting", *IEEE Trans. Micro. Theo. Tech.* **62**, 965-976 (2014).

[189] O. V. Prokopenko, I. N. Krivorotov, T. J. Meitzler, E. Bankowski, V. S. Tiberkevich, A. N. Slavin, "Magnonics", *Springer* **11**, 143-161 (2012).

[190] B. Fang, M. Carpentieri, X. Hao, H. Jiang, J. A. Katine, I. N. Krivorotov, B. Ocker, J. Langer, K. L. Wang, B. Zhang, B. Azzerboni, P. K. Amiri, G. Finocchio, and Z. Zeng, "Giant spin-torque diode sensitivity at low input power in the absence of bias magnetic field", arXiv:1410.4958v1.

[191] A. A. Tulapurkar, Y. Suzuki, A. Fukushima, H. Kubota, H. Maehara, K. Tsunekawa, D. D. Djayaprawira, N. Watanabe, and S. Yuasa, "Spin-torque diode effect in magnetic tunnel junctions", *Nature* **438**, 339-342 (2005).

[192] H. Kubota, A. Fukushima, K. Yakushiji, T. Nagahama, S. Yuasa, K. Ando, H. Maehara, Y. Nagamine, Koji Tsunekawa, David D. Djayaprawira, N. Watanabe, and Y. Suzuki, "Quantitative measurement of voltage dependence of spin-transfer torque in MgO-based magnetic tunnel junctions", *Nature Phys.* **4**, 37-41 (2008).

[193] S. Ishibashi, K. Ando, T. Seki, T. Nozaki, H. Kubota, S. Yakata, H. Maehara, A. Fukushima, S. Yuasa, and Y. Suzuki, "High Spin-Torque Diode Sensitivity in CoFeB/MgO/CoFeB Magnetic Tunnel Junctions Under DC Bias Currents", *IEEE Trans. Magn.* **47**, 3373-3376 (2011).

[194] C. Wang, Y.-T. Cui, J. Z.Sun, J. A. Katine, R. A. Buhrman, and D. C. Ralph, "Sensitivity of spin-torque diodes for frequency-tunable resonant microwave detection", *J. Appl. Phys.* **106**,053905 (2009).

[195] X. Cheng, C. T. Boone, J. Zhu, and I. N. Krivorotov, "Nonadiabatic stochastic resonance of a nanomagnet excited by spin torque", *Phys. Rev. Lett.* **105**, 047202 (2010).

[196] S. Miwa, S. Ishibashi, H. Tomita, T. Nozaki, E. Tamura, K. Ando, N. Mizuochi, T. Saruya, H. Kubota, K. Yakushiji, T. Taniguchi, H. Imamura, A. Fukushima, S. Yuasa, and Y. Suzuki, "Highly sensitive nanoscale spin-torque diode", *Nat. Mater.* **13**, 50–56 (2014).

[197] R. Tomasello, M. Carpentieri, and G. Finocchio, "Influence of the Dzyaloshinskii-Moriya interaction on the spin-torque diode effect", *J. App. Phys.* **115**, 17C730 (2014).

[198] J. C. Sankey, P. M. Braganca, A. G. F. Garcia, I. N. Krivorotov, R. A. Buhrman, and D. C. Ralph, "Spin-Transfer-Driven Ferromagnetic Resonance of Individual Nanomagnets", *Phys. Rev. Lett.* **96**, 227601 (2006).

[199] A. M. Kosevich, B. A. Ivanov, and A. S. Kovalev, "Magnetic Solitons", *Physics Reports* **194,** 117–238 (1990).

[200] S. M. Mohseni, S. R. Sani, J. Persson, T. N. Anh Nguyen, S. Chung, Y. Pogoryelov, P. K. Muduli, E. Iacocca, A. Eklund, R. K. Dumas, S. Bonetti, A. Deac, M. A. Hoefer, J. Åkerman, "Spin Torque–Generated Magnetic Droplet Solitons", *Science* **339,** 1295 (2013).

[201] M. A. Hoefer, T. J. Silva, and M. W. Keller, "Theory for a dissipative droplet soliton excited by a spin torque nanocontact", *Phys. Rev. B* **82,** 054432 (2010).

[202] V. Puliafito, L. Torres, O. Ozatay, T. Hauet, B. Azzerboni, and G. Finocchio, "Micromagnetic analysis of dynamical bubble-like solitons based on the time domain evolution of the topological density", *J. Appl. Phys.* **115,** 17D139 (2014).

[203] M. Carpentieri, R. Tomasello, R. Zivieri, and G. Finocchio, "Topological, non-topological and instanton droplets driven by spin-transfer torque in materials with perpendicular magnetic anisotropy and Dzyaloshinskii–Moriya Interaction", *Sci. Rep.* **5**, 16184 (2015).

[204] G. Finocchio, A. Prattella, G. Consolo, E. Martinez, A. Giordano, and B. Azzerboni "Hysteretic spin-wave excitation in spin-torque oscillators as a function of the in-plane field angle: a micromagnetic description", *J. Appl. Phys.* **110,** 123913 (2011).

[205] G. Finocchio, M. Carpentieri, A. Giordano, and B. Azzerboni, "Non-Adlerian phase slip and nonstationary synchronization of spin-torque oscillators to a microwave source", *Phys. Rev.* B **86**, 014438 (2012).

[206] R. Rajaraman, "Solitons and Instantons", *North-Holland*, Amsterdam, (1982).

[207] B. A. Ivanov, R. S. Khymyn, and A. K. Kolezhuk, "Pairing of Solitons in Two-Dimensional S=1 Magnets", *Phys. Rev. Lett.* **100**, 047203 (2008).

[208] R. Zarzuela, E. M. Chudnovsky, J. M. Hernandez, and J. Tejada, "Quantum dynamics of vortices in mesoscopic magnetic disks", *Phys. Rev.* B **87,** 144420 (2013).

[209] A. A. Belavin, A. M. Polyakov, A. S. Schwartz, Y .S. Tyupkin, "Pseudoparticle solutions of the Yang-Mills equations", *Phys. Lett. B* **59**, 85-87 (1975).

[210] C. Schütte, and M. Garst, "Magnon-skyrmion scattering in chiral magnets", *Phys. Rev.* B **90,** 094423 (2014).

[211] A. D. Verga, "Skyrmion to ferromagnetic state transition: A description of the topological change as a finite-time singularity in the skyrmion dynamics", *Phys. Rev.* B **90,** 174428 (2014).

[212] G. Finocchio, M. Ricci, R. Tomasello, A. Giordano, M. Lanuzza, V. Puliafito, P. Burrascano, B. Azzerboni, and M. Carpentieri[5], "Skyrmion based microwave detectors and harvesting", arXiv:1510.03841v1.

[213] M. Belmeguenai, J.-P. Adam, Y. Roussigné, S. Eimer, T. Devolder, J.-V. Kim, S. Mourad Cherif, A. Stashkevich, and A. Thiaville, "Interfacial Dzyaloshinskii-Moriya interaction in perpendicularly magnetized Pt/Co/AlO*x* ultrathin films measured by Brillouin light spectroscopy", *Phys. Rev. B* **91**, 180405(R) (2015).

[214] J. Cho, N.-H. Kim, S. Lee, J.-S. Kim, R. Lavrijsen, A. Solignac, Y. Yin, D.-S. Han, N. J. J. van Hoof, H. J. M. Swagten, B. Koopmans, and C.-Y. You, "Thickness dependence of the interfacial Dzyaloshinskii–Moriya interaction in inversion symmetry broken systems", *Nature Comm.* **6**, 7635 (2015).

[215] S. Pizzini, J. Vogel, S. Rohart, L. D. Buda-Prejbeanu, E. Jué, O. Boulle, I. M. Miron, C. K. Safeer, S. Auffret, G. Gaudin, and A. Thiaville, "Chirality-Induced Asymmetric Magnetic Nucleation in Pt/Co/AlO_x Ultrathin Microstructures", *Phys. Rev. Lett.* **113**, 047203 (2014).

[216] H. Yang, A. Thiaville, S. Rohart, A. Fert, and M. Chshiev, "Anatomy of Dzyaloshinskii-Moriya Interaction at Co/Pt Interfaces", arXiv:1501.05511v1.

[217] S.-Z. Lin, C. D. Batista, and A. Saxena, "Internal modes of a skyrmion in the ferromagnetic state of chiral magnets", *Phys. Rev. B* **89**, 024415 (2014).

[218] H. Meng, R. Sbiaa, M. A. K. Akhtar, R. S. Liu, V. B. Naik, and C. C. Wang, "Electric field effects in low resistance CoFeB-MgO magnetic tunnel junctions with perpendicular anisotropy", *Appl. Phys. Lett.* **100**, 122405 (2012).

[219] R. Verba, V. Tiberkevich, I. Krivorotov, A. Slavin, "Parametric Excitation of Spin Waves by Voltage-Controlled Magnetic Anisotropy", *Phys. Rev. App.* **1**, 044006 (2014).